

UNIVERSITY OF OKLAHOMA
GRADUATE COLLEGE

ENHANCING MULTI-PURPOSE MMWAVE SYSTEM AND W-BAND
ANTENNA IN PACKAGE CALIBRATION AND MEASUREMENTS

A THESIS

SUBMITTED TO THE GRADUATE FACULTY

in partial fulfillment of the requirements for the

Degree of

MASTER OF SCIENCE

By

EDGAR ALEXIS OBLITAS MANTILLA
Norman, Oklahoma
2024

ENHANCING MULTI-PURPOSE MMWAVE SYSTEM AND W-BAND
ANTENNA IN PACKAGE CALIBRATION AND MEASUREMENTS

A THESIS APPROVED FOR THE
SCHOOL OF ELECTRICAL AND COMPUTER ENGINEERING

BY THE COMMITTEE CONSISTING OF

Dr. Jorge Salazar-Cerreño, Chair

Dr. Tian-You Yu

Dr. Caleb Fulton

Acknowledgments

My heartfelt gratitude extends to all those who have supported me and contributed to this thesis. I am deeply thankful to my committee members for their generous time and patience, as well as to everyone who aided me, whether through resources or wisdom, on this academic journey.

First and foremost, I wish to express my profound appreciation to Dr. Jorge Salazar for his unwavering support and guidance throughout my master's studies. I am also immensely grateful to him for granting me the extraordinary opportunity to pursue my graduate studies at the University of Oklahoma and to work at the Advanced Radar Research Center.

I extend my gratitude to the sponsor, Metawave Corporation, whose support made this project possible. Special thanks go to Andy Bonthron, Edmond Megerdichian, and Maha Achour for providing us with ample resources to develop this project, as well as to Rodrigo Lebron and Arturo Umeyama for their foundational work that greatly influenced this project's development.

I offer special thanks to the Committee members, Dr. Tian-You Yu and Dr. Caleb Fulton, for their acceptance of membership, their valuable time, and their constructive feedback in reviewing this thesis.

I am also thankful to the Advanced Radar Research Center for the facilities and resources that enabled me to develop this project, as well as for the invaluable support from the individuals associated with the center. I would like to acknowledge the contributions of Dr. Rockee Zhang, Dr. Jay McDaniels, Dr. Justin Metcalf, Felipe

Moncada, Sergio Rodriguez, Khuda Burdi, Mariel Avalos, Marcelo Moreno, Jorge Alva, Dr. Syed Jehangir, Dr. Zeeshan Qamar, Dr. Nafati Aboserwal, Dr. Cesar Salazar, Dale Sexton, Johnny Cook, and Caleb Nelson, who supported, assisted, or mentored me over the course of these two years.

To conclude, I am deeply indebted to my beloved family and friends for their unwavering support and encouragement throughout my journey in pursuing graduate studies. To my revered parents, Edgar Alberto Oblitas and Juana Mantilla, I owe everything I am today; their guidance has shaped my character and achievements. Gratitude also extends to my siblings – Johan, Fatima, Valeria, Mauricio, and Gabriel Oblitas – whose boundless support and encouragement have been my pillars of strength.

Special appreciation is reserved for my longtime friend from my undergraduate studies, Juan Carlos Loyza, with whom I continue to share camaraderie and laughter.

Table of Contents

Acknowledgments	iv
List Of Tables	viii
List Of Figures	ix
Abstract	xiii
1 Introduction	1
1.1 Motivation	1
1.2 Literature Review	2
1.3 Proposed System	6
1.4 Organization of the thesis	7
2 Original mmWave Scanner System	9
2.1 Background and Requirements of Antenna Measurements	9
2.1.1 Near-Field Scanning Measurements	9
2.1.1.1 Near-field to Far-field Transformation and Probe Cor- rection	12
2.1.2 Far-Field Scanning Measurements	13
2.2 System Description	14
2.2.1 Hardware	15
2.2.2 Software	18
2.3 Modes of Operation	20
2.3.1 Near-Field Measurements	20
2.3.2 Far-Field Measurements	22
2.3.3 Material Characterization Measurements	24
2.4 Summary	25
3 System Improvements	27
3.1 New Graphical User Interface Software	27
3.2 Software Description	28
3.3 User Interface and Scanning Improvements	31
3.3.1 New Graphic User Interface	31
3.3.2 Near-Field Scanning Improvements	34
3.3.3 Raster Scanning Algorithm Improvements	37
3.3.3.1 Continuous Raster Scanning Queue Lag Issue	41
3.3.4 Far-field AUT Holder Structure	45
3.4 Results, Comparison and Validation	48

3.4.1	Near-field Test Measurement Results	48
3.4.2	Far-field Test Measurement Results	54
3.5	Summary	54
4	W-band Antenna-in-Package Calibration	56
4.1	Antenna-in-Package	56
4.1.1	Metawave's Antenna-in-Package	56
4.2	System Description	58
4.2.1	Requirements	60
4.2.2	Near-Field Probe and Polyrod Antenna	61
4.3	Calibration Setup	63
4.3.1	Setup Components and Power Budget	66
4.4	Summary	70
5	AiP Calibration, Measurement Tests and Results	71
5.1	AiP Calibration Process	71
5.1.1	Calibration Results	72
5.2	AiP Control Software	78
5.3	Patterns Measurement Tests	79
5.3.1	Horizontal Near-Field Scanning	79
5.3.2	AUT in-situ Far-field Scanning	82
5.4	Radiation Pattern and Measurements	83
5.5	Summary	86
6	Conclusions and Future Work	88
6.1	List of Conclusions	88
6.2	Future work	91
	Bibliography	93
	Appendix A	
	Velmex Application Notes-AN10697	

List Of Tables

2.1	Specifications of Distributed Network Analyzer	17
2.2	VELMEX Motorized Positioners Specifications. Notations (B) and (R) Correspond to Bislid and Rotary Table Respectively	18
3.1	Average period of the last 10 measurements corresponding to Figure 3.11.a and b.	42
3.2	Average period of the last 10 measurements corresponding to Figure 3.11.c and d.	45
3.3	Antenna NF measurements records, showing the total number of samples and a time comparison between the continuous and park-and-probe methods.	52
4.1	Summary of the electrical characteristics of the AiP. Provided by Metawave Corporation.	59
4.2	Link budget of the TX calibration setup	68
4.3	Link budget of the RX calibration setup	69
5.1	Statistical parameters of the calibration results of the AiP chip antenna.	73
A.1	A portion of the complete table from [1] is provided below, where x represents the value in the command AmMx , which configures the acceleration, and m denotes the motor ID.	97

List Of Figures

2.1	Field regions around the antenna	10
2.2	Acquisition geometries for planar near-field range measurements. Figures adapted from [2]	11
2.3	Graphical representation of the scanning window dimension calculation represented by Equation 2.1.	12
2.4	Illustration of a far-field antenna measurement generic setup.	14
2.5	Description of the multipurpose mm-Wave scanner modes: a) All the hardware that makes up the mmWave scanner. b) Shows the setup and components used in the near-field antenna test. c) Shows the setup in the far-field antenna test. d) Shows the setup for material and radome characterization.	16
2.6	Main window of the LABVIEW software shows the operation modes, motor positions, and VNA s-parameters.	19
2.7	a) and b) Near-field results of the NF measurement test of amplitude and phase, respectively. c) E and H plane of the AUT's simulated and measured radiation patterns. Figures adapted from [3].	21
2.8	Far-field measurement setup and pattern results of a 77 GHz spherical lens antenna: (a) Picture of the antenna lens and setup in FF mode. (b) Lens antenna connected to a WR-10 waveguide used as a feed. (c) FF antenna patterns using far-field measurement data overlapped with simulated results obtained in HFSS. Source: Adapted from [3].	23
2.9	Comparison between simulated (HFSS) and measured results obtained in the mm-Wave region: a) Permittivity vs. frequency. b) Error in permittivity vs. frequency. c) Tangent-loss vs. frequency. d) Error in tangent-loss vs. frequency. Figures adapted from [3].	24
3.1	Diagram of the structure of the system in reality and its model in the software using OOP.	30
3.2	New GUI main window tab for connection and configurations to the VELMEX controllers and the Copper-mountain VNA.	32
3.3	New GUI near-field setup window, scanning range and position grid calculations are located in this window.	32
3.4	New GUI far-field setup window, configures the angle range, resolution and polarization.	33
3.5	New GUI material characterization setup window, configures the motors' position for alignment and calibration, and visualizes the s-parameters collected from the VNA.	33
3.6	Near-field measurement in progress of a horn antenna at 75 GHz in cross polarization.	35
3.7	GUI tab window in the Near-field section that shows the measured radiation pattern.	36

3.8	GUI tab window in the Near-field section that shows the hologram back projection results.	36
3.9	a) The trapezoidal speed profile of the VELMEX motor showing the sections where the speed is variable and constant. b) Raster scan sampling and motion positions	39
3.10	Timer object schedule configuration for multi-execution mode. Figure adapted from [4]	40
3.11	a) and b) present the magnitude and phase, respectively, of measurements conducted with the probe moving back and forth along the same row, demonstrating the error in timer period. Similarly, c) and d) showcase the magnitude and phase of the identical process, incorporating the application of Equation 3.3.	43
3.12	a) First prototype of the AUT holder structure, 3D printed made by a combination of PLA and ABS. b) Second prototype of the AUT holder structure made with aluminum. c) Photo of the complete far-field setup featuring both AUT and the probe antenna.	46
3.13	The AUT holder structure accommodates various antennas installed as AUTs, each centered to the rotating axis. The antennas include: a) WR10 Spot Focused Horn Lens Antenna (SAQ-903071-10-S1). b) WR10 Lens Corrected Antenna (SAL-7531142607-10-S1). c) WR12 Pyramidal Horn Antenna (SAR-2309-12-S2) [5].	47
3.14	a) NF magnitude results of the SGH in dB. b) NF phase results of the SGH in degrees at 75 GHz. c) and d) are the magnitude and phase of the cross-polarization measurement of the SGH at 75 GHz respectively. e) SGH radiation pattern comparison between simulation and measurement in both E- and H-planes.	49
3.15	a) and b) are the NF-P results in magnitude and phase respectively of the SGH antenna (SAR-2309-12-S2) which is used as reference. c) and d) are the NF results of the continuous method without any period correction. e) and f) are the results of the same method applying a period correction.	51
3.16	Radiation patterns of the NF data illustrated in Figure 3.15, it shows the park-and-probe method, the continuous method with and without period correction.	52
3.17	Radiation patterns of the pyramidal horn antenna between the simulation, near-field and far-field results.	53
4.1	Simplified functional block diagram for both TX and RX channels in MARCONI beamforming chips. LNA represents the low noise amplifier, VMPS stands for vector modulated phase shifter, VGA denotes variable gain amplifier, LA represents linear amplifier, and PA stands for power amplifier.	57

4.2	a) A photo of the AiP chip antenna size compared with a one-cent coin. b) A photo taken from an electronic microscope showing the precise dimensions of the antenna elements and the spacing between elements.	58
4.3	Image of the hybrid test system portraying the near-field calibration process and featuring the AiP antenna array and evaluation board. The system integrates both near-field and far-field scanning operation modes	60
4.4	a) and b) Measured radiation patterns of the NF OEWG probe and with the polyrod respectively.	62
4.5	Illustration of the calibration setup for TX and RX AiPs.	64
4.6	AiP variable values sweep measurement results a) with an input power of -15 dBm and b) with an input power of -25 dBm.	67
5.1	Summarized block diagram of the calibration algorithm.	71
5.2	S-parameters (amplitude) of each individual channel of the TX AiP. Panels a) and b) display the calibration results with the calibration values at 77 GHz, panels c) and d) depict the results at 78 GHz, and panels e) and f) show the results at 80 GHz. Additionally, panels b), c), and f) present the s-parameters normalized with respect to (w.r.t) channel 8.	74
5.3	S-parameters (phase) of each individual channel of the TX AiP. Panels a) and b) display the calibration results with the calibration values at 77 GHz, panels c) and d) depict the results at 78 GHz, and panels e) and f) show the results at 80 GHz. Additionally, panels b), c), and f) present the s-parameters normalized with respect to (w.r.t) channel 8.	75
5.4	S-parameters (amplitude) of each individual channel of the RX AiP. Panels a) and b) display the calibration results with the calibration values at 77 GHz, panels c) and d) depict the results at 78 GHz, and panels e) and f) show the results at 80 GHz. Additionally, panels b), c), and f) present the s-parameters normalized with respect to (w.r.t) channel 8.	76
5.5	S-parameters (phase) of each individual channel of the RX AiP. Panels a) and b) display the calibration results with the calibration values at 77 GHz, panels c) and d) depict the results at 78 GHz, and panels e) and f) show the results at 80 GHz. Additionally, panels b), c), and f) present the s-parameters normalized with respect to (w.r.t) channel 8.	77
5.6	Photo of the AiP controller software developed specifically for automatic analog beamforming process.	79

5.7	a) and b) Magnitude and phase NF measurements by increasing the attenuation of the variable attenuator on FE2 to 35 dB respectively. c) and d) Magnitude and phase NF measurements with saturation in the LNA. e) Radiation patterns comparison between the theoretical, measured with saturation in the LNA and measured normally without saturation.	81
5.8	Far-field scan process for a) an OEWG probe antenna used for near-field tests, and b) the OEWG with a polyrod structure attached. . . .	82
5.9	Near-field measurements for both TX and RX AiP chips in broadside uniform distribution.	84
5.10	AiP antenna array radiation patterns at 78 GHz a) Comparison of the radiation patterns using both park-and-probe (P&P) and continuous NF scanning modes in both H- and E-planes. b) Comparison between the calibrated and not calibrated AiP antenna array in the H-plane, c) comparison of the calculated and measured radiation pattern of the AiP antenna array in broadside both E- and H-planes, d) comparison of the radiation pattern obtained by the NF scanning after a NF to FF transformation and the pattern obtained by the FF scanning, and e) A beam-steering of the TX AiP antenna array in azimuth from -20° to 20° every 5°	85

Abstract

The millimeter-wave (mmWave) scanner is a system built a few years ago by the phased array antenna research and development group (PAARD) in the Advanced Radar Research Center (ARRC) with the purpose of measuring, characterizing, and calibrating mmWave antennas without significantly changing the setup. The most important reason for developing a multitasking system is to utilize a vector network analyzer (VNA), in many applications. This thesis proposes upgrades to this system, starting with the software, which restricts the system with poor motion flow, and addition of new features to the system that allow faster and reliable measurements.

A relevant feature that was added is the calibration and measurement of a W-band active phased array antenna in a package that was manufactured for commercial purposes. Due to the nature of the active element in a phased array antenna, calibration of the system is required for precise and correct performance, which is critical for radio frequency systems. Over-the-air (OTA) calibration is a powerful technique used in phased array antennas in real-world environments. This thesis proposes a novel measurement system to calibrate and characterize the antenna. The system is a multi-axis hybrid system with nine degrees of freedom, used to perform the calibration process and also to scan the antenna radiation pattern in both near-field (NF) and far-field (FF) regions. Experimental results of the calibration method show high precision in the element radiation values, and excellent agreement between the antenna array radiation pattern measured in the near-field and far-field is achieved.

Chapter 1

Introduction

1.1 Motivation

The Phase Array Antenna Research and Development (PAARD) group, part of the Advanced Radar Research Center (ARRC), has been developing antenna measurement systems as it is an essential field in the antenna industry. Metawave Corp. was a startup company focused on radar for the automotive industry. One area of development within the company was phased array antennas at millimeter-wave (mmWave) frequencies. Since 2017, Metawave and the University of Oklahoma (OU) have been collaborating on a project to develop a system enabling multiple measurements for active array antennas in the W-band. Originally, the system was required to perform near-field (NF) measurements, far-field (FF) measurements, and phased array antenna calibration. Later, a module for material and radome characterization was also included. Due to limited time to develop a complex measurement system, OU developed hardware to perform NF, FF, and phased array calibration. The graphical user interface (GUI) was implemented using LABVIEW. However, this interface was not optimized for user-friendliness and efficiency. Part of this work aims to improve the GUI, adding new features to make the system more efficient.

Years later, Metawave Corp. requested OU-PAARD's assistance in calibrating an active phased array antenna. This new antenna, developed by them, is a high-tech antenna in a package (AiP) operating at mmWave frequencies between 76-81 GHz and capable of analog beamforming. Metawave ask for assistance to built a new calibration setup for the AiP. However, it was decided that the versatility of the already developed mmWave scanning system would be perfect to implement the calibration setup by adding more configurations. This would also allow the system to do more than just calibration; it could include NF and FF scanning algorithms to verify the efficiency of the calibration. The purpose of this work is to describe the improvements made in the mmWave scanner system and the implementation of the AiP calibration setup.

1.2 Literature Review

Each year, driven by technological progress and the swift expansion of services reliant on the electromagnetic spectrum, both military and civilian sectors face an urgent demand to secure space in the spectrum for essential operations, where the communication sector is especially crucial [6]. Millimeter waves (mmWave) frequencies seem to be a viable solution to this necessity. mmWaves refer to the range of frequencies where the wavelength ranges between 10 to 1 millimeters (30 - 300 GHz). One of the greatest interests to the industry and communication systems in these frequencies is the wide range of bandwidth. For example, this characteristic is valuable for supporting applications such as high-speed data transmission and video

streaming. Another important characteristic of these frequencies is that relatively secure communications can be performed in the absorption resonance bands. Additionally, free space losses are much higher in these frequencies compared to radio frequencies. Typically, the range is below 20 km, which is useful for short-range communications. This allows a high degree of frequency reuse [7]. While high atmospheric attenuation might seem like a disadvantage in certain applications, it is favorable in others, especially in the automotive industry.

Typically, the size of an antenna is directly related to the wavelength (λ) of the frequency of operation. In the mmWave frequencies, which are characterized by wavelengths measured in millimeters, the antennas exhibit millimetric dimensions. Furthermore, when designing array antennas, the spacing between the elements is typically less than 1λ [8]. To address these challenges, a relatively new technology called antennas-on-chips has been widely implemented, especially in mmWave applications. Numerous studies have underscored the compelling attributes of antenna-on-chip technology, each tailored for specific applications [9–11]. Antennas-on-chips are commonly used in fully integrated systems. They reduce the complexity of the matching network and reduce the front-end losses and noise figure [12]. Another advantage of this technology is the reduction of connectors between the RF circuits and the antenna, allowing flexibility in the circuit design [13]. For radar systems, the greatest advantage is the bandwidth, which enables the radar system to achieve much better spatial resolution. A radar system operating in a range of frequencies between 57 to 66 GHz has the benefit of using a large bandwidth (9GHz). This bandwidth will allow the system to have a spatial resolution of 2 cm [14]. Naturally,

this technology and the properties of short-range mmWave frequencies are particularly significant for automotive radar applications, where frequencies ranging from 24 GHz to 77 GHz are extensively studied and utilized [15–18].

In recent years, Metawave Corporation has pioneered the development of a cutting-edge category of active phased array antennas-on-chips tailored for the automotive industry. Their groundbreaking contribution manifests in the form of the Antenna in Package (AiP). This unique in-package antenna boasts the remarkable ability to execute beamforming and beam-steering functions. Comprising 16 patch antennas, the chip operates predominantly within the frequency range of 77 to 80 GHz [19].

The advantage that phased array antennas provide is the capability to change the shape of the radiation pattern by defining the magnitude and phase of each element antenna. By using electronic devices like amplifiers and phase shifters, it is possible to electronically modify the radiation pattern. However, these devices are commonly frequency and temperature dependent, requiring calibration for the proper functioning of the system [20]. Additionally, the non-ideal conditions of the components of each antenna element on the array result in what is known as excitation errors. These errors would cause array pattern distortion, gain degradation, worse side lobe level, and null drifts [21, 22]. Over the years, many calibration algorithms were developed to compensate for these errors. Some studies use simple algorithms to calculate the amplitude and phase modulation compensation like in [20], while others use more complex algorithms [21, 23]. It is important to highlight that each calibration algorithm was designed for a unique architecture of the

phased array antenna. For example, mutual coupling calibration is a technique that relies on the neighboring antenna elements of the calibrating element [24–26]. The advantage of this mutual coupling calibration is the self-test capabilities that allow performing calibration without the use of a probe antenna outside the antenna under calibration. Aside from the calibration algorithm used, another important aspect of the calibration is the range in which the calibration is performed. The most common calibration technique in the near-field region is the park-and-probe technique [20, 22], which positions the probe antenna in front of the calibrating element. Calibration in the near-field range is more common in low frequencies (below 20 GHz) because the far-field distance of the antenna depends directly on the wavelength, making near-field measurement and calibration more feasible; otherwise, it would require a huge space to perform the tests. However, there are solutions to this problem such as utilizing a compact antenna test range, which significantly reduces the measurement distance [27], or using unmanned aerial vehicles (UAVs). The use of this technology has been widely studied and implemented in the UAV measurement sector [28]. Many studies have been conducted pointing out the advantages and challenges in frequencies below the mmWaves, showing promising results [29–31]. For mmWave frequencies, due to the short far-field distance, it is more practical to perform far-field tests on the antenna under testing. Over-the-air calibration emerges as a reliable method for achieving high precision calibration in antenna systems. Extensively documented in the literature, this technique has been

consistently employed for calibration purposes in both on-chip antennas at frequencies exceeding 220 GHz and in phased array antennas necessitating sophisticated algorithms to derive correction weights for individual elements [23, 32, 33].

Antenna test scanners have been developed since the second half of the last century, encompassing both near-field and far-field scanners. NSI-MI is one of the leading companies in near-field antenna test scanners, as well as in studying and developing near-field measurement techniques and hardware [20, 34–36]. With the advancement of technology, new systems have been developed to perform these tests with a higher degree of precision and speed at a lower cost, as professional systems are highly expensive. Furthermore, these systems are typically designed to meet research needs and may require specific modifications [37–39]. In the realm of mmWave, due to the reduced size of the wavelength, scanning systems tend to be more compact. Additionally, there is the possibility of adding more functionalities and test capabilities, as demonstrated in [3, 40, 41].

1.3 Proposed System

The focus of this thesis is to develop new software that allows users to have easier control over the system. The user interface (UI) is more organized and intuitive and can show real-time data collected by measurements, with most of the post-processing algorithms included in the software. The versatility of the software is another strong point. As long as the user has knowledge about the code, it is possible to program new operation methods as well as new specific functionalities

into the system. Conversely, on the hardware side, a structure was designed to aid in far-field scanning tests. This structure allows easy installation of the antennas under test (AUT) and also allows adjustment of the distance between the axis of rotation and the center of the antenna, achieving flexibility when measuring different types of antennas. As a consequence of the versatility of the system, three more functionalities or operation modes were implemented. With an ingenious design to achieve far-field calibration tests for mmWave antennas in package (AiP), which need to be located horizontally, it was possible to calibrate and characterize these AiPs with high precision. Although the calibration process had to be done outside of the UI, the near-field and far-field measurement test algorithms were implemented into the software. It is also important to highlight that all calibration, near-field, and far-field measurements use the same probe. Even though theoretically, near-field and far-field probes have different properties, a simple but powerful component was used to compensate for this difference.

1.4 Organization of the thesis

The content of this thesis will take a progressive approach. To begin with, Chapter 2 reviews the background of near-field and far-field tests, describes the features of the original mmWave scanner, including hardware, software, and operation modes, and presents measurement results taken at the time of its development. It also highlights the disadvantages of the original system's software. In Chapter 3, all the improvements that were implemented are discussed, starting with the change of the

software. The chapter describes the advantages that the new software will have over the previous one and provides a comparison of different scanning algorithms in all modes with measurement results shown in Chapter 2. Chapter 4 details the new situation that the company Metawave faced with their new product, the need for a calibration system, its requirements, and the system's design, components, and incorporation into the mmWave scanner system. Finally, in Chapter 5, the calibration algorithm and its results are described. Additionally, a new mode of NF and FF measurements was developed specifically for this antenna due to its special features, which will be further explained later. In the conclusions chapter, the advantages of the new software, measurement results, and the versatility to incorporate new setups and operation modes like the AiP calibration setup are discussed. The results of the latter will also be examined in this chapter.

Chapter 2

Original mmWave Scanner System

This chapter will describe the mmWave scanner system developed by Metawave Corp. and OU-ARRC, along with all the theoretical background implemented in the fabrication of this scanner system, as well as the measurement results obtained with the original software.

2.1 Background and Requirements of Antenna

Measurements

Theoretical background serves as a crucial guide in designing both the hardware and software components of the system. Its significance is essential; for instance, in software design, the background plays a pivotal role in determining the movement algorithms of the linear positioner for conducting precise measurements. Furthermore, it significantly influences the post-processing procedures.

2.1.1 Near-Field Scanning Measurements

An antenna is a device that transforms guided EM waves, from electric sources, into radiating waves that propagate in free space. The properties of these propagating waves change with the distance from the antenna. This space around the antenna is divided into three regions [8], as shown in Figure 2.1. Many authors have

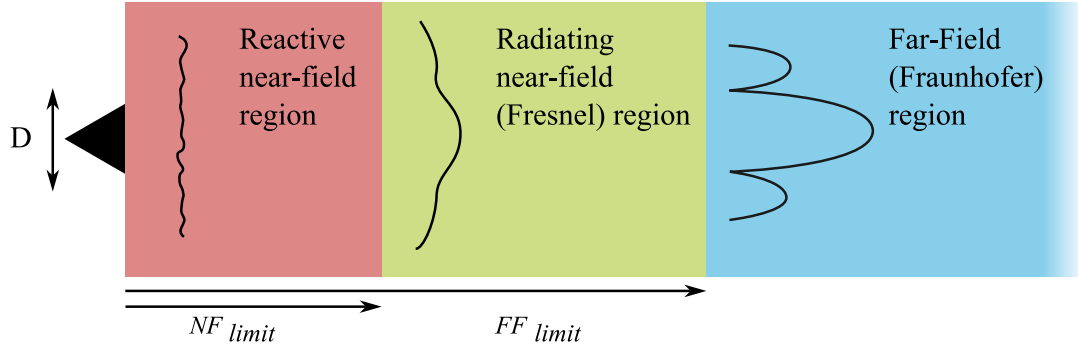


Figure 2.1: Field regions around the antenna

proposed different mathematical equations to define these regions. For example, Balanis [8] defined the limits as $NF_{limit} = 0.62\sqrt{D^3/\lambda}$ and $FF_{limit} = 2D^2/\lambda$, where λ is the wavelength. Slater [42] defined the $NF_{limit} = 3\lambda$, and the FF_{limit} is the same as Balanis.

As the name indicates, near-field scanning antenna measurements are performed in the near-field region or Fresnel region. There are mainly three types of NF scanning: planar near-field range (P-NF), cylindrical near-field range (C-NF), and spherical near-field range (S-NF) [42, 43]. The selection of the test type usually depends on the geometry of the AUT. However, for NF system designers, the decisive factor is how complex the system will be. Unlike the P-NF, where the AUT remains at rest, the C-NF and S-NF require the AUT to rotate in azimuth (C-NF, S-NF) and elevation (only S-NF) [2]. For P-NF, there are also many types of acquisition geometries, as shown in Figure 2.2. The scan patterns must meet certain requirements to acquire reliable data, such as the definitions of dimensions, probe antenna, and sampling rate, which must meet the Nyquist criterion to avoid aliasing. The most common scan pattern is the raster scan [42] due to its simplicity. The raster

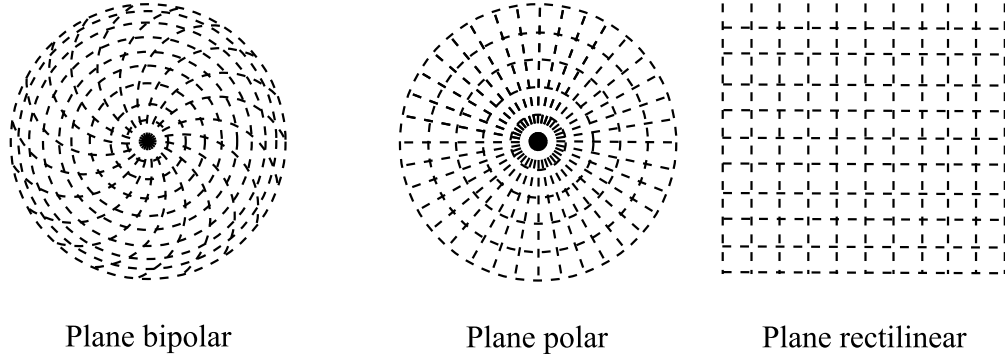


Figure 2.2: Acquisition geometries for planar near-field range measurements. Figures adapted from [2]

scan pattern is a P-NF, and it consists of moving the probe antenna linearly in one direction and in the opposite direction in the next row.

Some special characteristics are required for the probe antenna in NF measurements. According to Gregson et al. [2], the probe antennas must have the following characteristics: time-invariant gain and mechanical rigidity, absence of nulls in the pattern and low directivity, wide bandwidth, low reflection coefficient, and good polarization purity, or at least better than that of the AUT.

In the planar near-field test, it starts by calculating a scanning range, which is the distance the probe travels in the x - y plane. The formula to calculate the scanning range is shown below. Figure 2.3 shows the a graphic representation of the formula.

$$SR = D + P + 2Z \tan(\theta_{FF}) \quad (2.1)$$

D represents the diameter of the AUT, P represents the diameter of the probe, Z represents the distance between the AUT and the probe antenna, and θ_{FF} represents the maximum processing angle from the bore-sight [36].

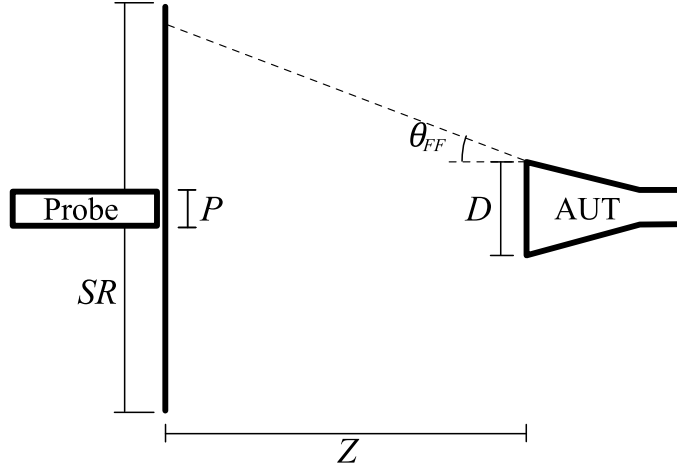


Figure 2.3: Graphical representation of the scanning window dimension calculation represented by Equation 2.1.

2.1.1.1 Near-field to Far-field Transformation and Probe Correction

The post-processing algorithm that transforms the NF phase into an angular spectrum is called near-field to far-field (NF/FF) transformation, even though the terminology is not correct since it does not transform the data from one distance to another. The transformation only changes the phase front into an angular spectrum at the same position, and the result is an equivalent of a far-field pattern [42]. There are many NF/FF transformation techniques, and these differ depending on the NF scanning type, which includes planar, cylindrical, and spherical types. However, the principal advantage of the planar NF/FF technique is its mathematical simplicity, and it is also easy to implement the Fast Fourier Transform (FFT), a highly effective tool capable of performing the high-level calculations required by the Fourier transform in a very short amount of time [8]. This transformation involves a large number of equations and calculations detailed in [8], [44], and [45].

The probe correction is a necessary process in NF measurements because it compensates the non-ideal behavior of the probe antenna. In this process the far-field patterns of the probe must be known due to the interaction of the NF phase front between the probe and the AUT antennas [45], [35]. And the equations that define the probe correction are the following.

$$E_C = E_{Cu}/E_{probe} \quad (2.2)$$

$$E_X = E_{Xu}/E_{probe(\phi+90^\circ)} \quad (2.3)$$

Where E_C and E_X are the true/compensated FF patterns of the AUT in co-polarization and cross-polarization directions respectively, E_{Cu} and E_{Xu} are the uncompensated FF patterns of the AUT. E_{probe} represents the FF pattern of the probe antenna, all in complex values. This is a simplified version of another more complete equation in [35], where the FF patterns of the cross-polarization direction of the probe antenna were ignored.

2.1.2 Far-Field Scanning Measurements

For far-field measurements, the sampling must be taken in the FF region. Figure 2.1 shows where the FF region is located; the distance of the FF limit is defined by Balanis [8] as follows:

$$FF_{limit} = \frac{2D^2}{\lambda} \quad (2.4)$$

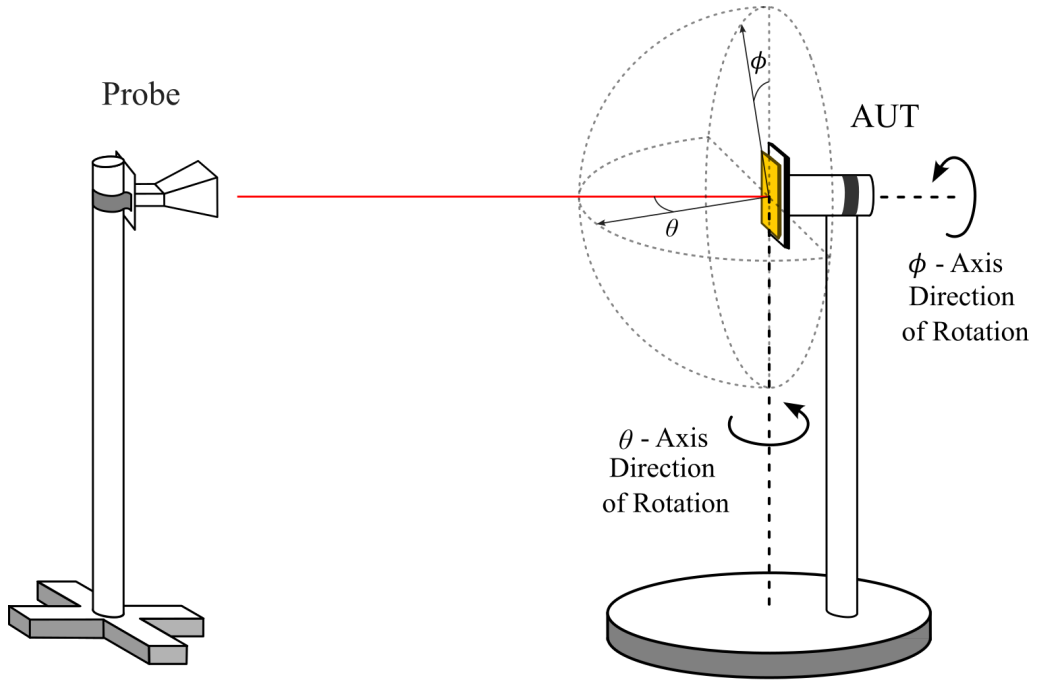


Figure 2.4: Illustration of a far-field antenna measurement generic setup.

This region is defined as the region where the angular field distribution is independent of the distance from the antenna. For this test, both antennas must have a separation of at least FF_{limit} between them, so that the AUT is illuminated by nearly planar waves generated by the probe [46]. The test consists of straightforwardly taking measurements with the instrument while rotating the AUT in both azimuth and elevation. Figure 2.4 illustrates a generic picture of a far-field antenna measurement test.

2.2 System Description

The system was originally designed for a variety of tests that allow the measurement and calibration of W-band antennas. With precise hardware design and software control, measurements can be performed with a high level of precision.

The system was originally designed to work in the frequency range of 75-110 GHz (W-band). The tests, also known as modes of operation, include near-field planar (NF), far-field (FF), active array calibration (AC), material characterization (MC), and radome characterization (RT). For all these operation modes, most of the components are shared. This means that the hardware, software, and measurement instruments are shared, though some components like the probes cannot be shared since they must have special features depending on the application. This multitasking characteristic of the system allows for a reduction in both costs and physical space requirements, especially when instrumentation like a VNA in mmWave frequencies (W-band) is very expensive in the market.

2.2.1 Hardware

The hardware of the system consists of two different and important types. The first one is the instrumentation, which is a VNA. Copper Mountain Technologies (CMT) is a renowned company that manufactures VNAs capable of operating at ultra-high frequencies due to their frequency extension system, which has the ability to make accurate measurements for various mm-Wave applications. The model chosen for the system is the C4209. It is a two-port vector analyzer with a fast sweep speed down to $10\mu\text{s}$ per point and a dynamic range of up to 110 dB. Its normal frequency range of operation is from 100 kHz to 9 GHz. However, with the CobaltFx frequency extenders (FE), the frequency range increases to 75 GHz to 110 GHz. Table 2.1 shows more specifications of the instrument. The CobaltFx system is precise equipment with repeatable measurement results, offering fast sweep

measurements down to $10\mu\text{s}$ per point and a dynamic range of up to 110 dB. It is ideal for mmWave systems.

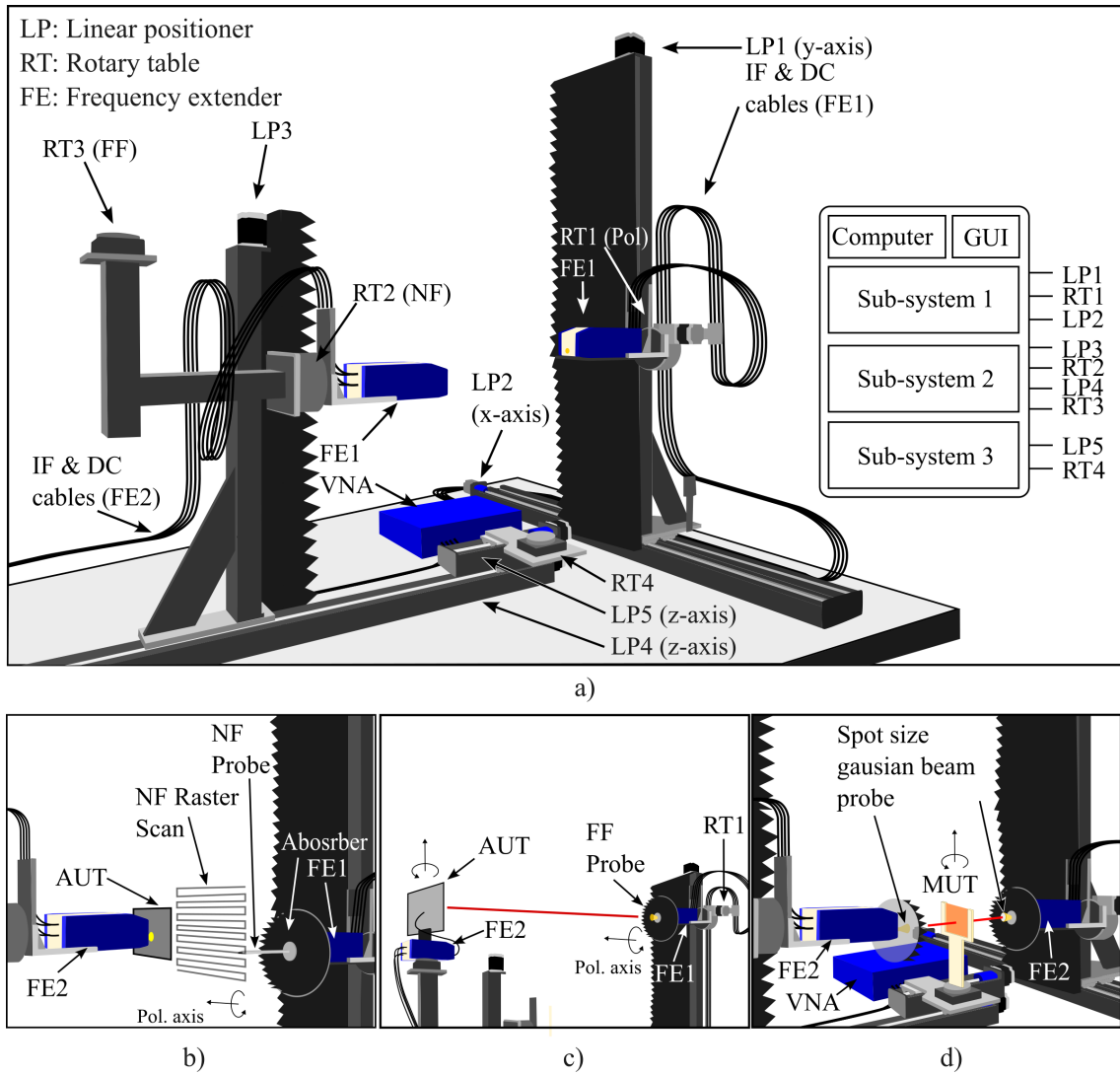


Figure 2.5: Description of the multipurpose mm-Wave scanner modes: a) All the hardware that makes up the mmWave scanner. b) Shows the setup and components used in the near-field antenna test. c) Shows the setup in the far-field antenna test. d) Shows the setup for material and radome characterization.

The second type of hardware in the system is the positioners. This hardware allows the motion of the components in space. The manufacturer of these positioners is called VELMEX. This company is well-known for manufacturing reliable motorized positioners with high resolution for positioning and easy control. There are

Table 2.1: Specifications of Distributed Network Analyzer

Parameters	VNA (CMT C4209)	FE (CobaltFx FEV-10)
Freq. Operation	100 kHz to 9 GHz	75 GHz to 110 GHz
Test Power out	-60 dBm to 60 dBm	0 dBm to 5 dBm
Dynamic Range	138 dB (142 dB typ)	100 dB (110 dB typ)
Interface	N-Female	WR-10
AC/DC Power	110-220 VAC (75W)	6V at 2.2A
Weight	7 kg	3-5 kg
Temp. Operation	0 °C to 30 °C	0 °C to 30 °C

two types of positioners used in the system. The linear positioner, known as bislide, allows linear motion along a determined axis. The rotary tables allow rotational motion with high angular resolution. The resolution of the positioners depends on the model. However, in this system, all the bislides have the same resolution; the only aspect that changes is the travel length. Table 2.2 shows more information about the motorized positioners.

The final design of the system was done by using 9 motorized positioners and the VNA with the frequency extenders, separating the system into three subsystems, as shown in Figure 2.5. This figure also shows how the operation modes are distributed and how they work.

Table 2.2: VELMEX Motorized Positioners Specifications. Notations (B) and (R) Correspond to Bislide and Rotary Table Respectively

Positioner Model	Type	Travel Resolution	Travel Length (B)/ Gear Ratio (R)	Width (B)/ Diameter (R)	Dynamic Load	Repetibility
MT10-0480-E01	Tandem Bislide	6 μ m	121.92 cm	17.27 cm	272.15 kg	5.08 μ m
MN10-0480-E01	Bislide	6 μ m	121.92 cm	8.64 cm	136.1 kg	5.08 μ m
MN10-0240-E01	Bislide	6 μ m	60.96 cm	8.64 cm	136.1 kg	5.08 μ m
MN10-0060-E01	Bislide	6 μ m	15.24 cm	8.64 cm	136.1 kg	5.08 μ m
B4872TS	Rotary Table	100 arcseg	72:1	12.7 cm	11.3 kg (Vertical)	1 arcseg
B5990TS	Rotary Table	100 arcseg	90:1	4.2 cm	22.6 kg (Horizontal)	1 arcseg

2.2.2 Software

The software installed on the computer of the system is the controller; it is in charge of communication and sending commands to the VELMEX controllers to move the positioners precisely. It is also capable of configuring and collecting information from the VNA. The software was developed in NI-LABVIEW and has support to connect and control all elements of the system. The graphical user interface developed is also capable of performing complex processes like raster scanning for the NF tests or circular scanning for the FF tests by synchronizing different positioners and the VNA precisely, allowing the system to take reliable measurements. Finally, this graphical interface is capable of data collection for all modes

of operation and saving the raw data in files correctly, to later use these files for post-processing using MATLAB scripts for data visualization.

The system was designed and built in 3 and a half months by the PAARD group. Starting from mid-December 2019, the system was delivered by the end of March 2020. During that period, only 50 hours were used to develop the software, which is approximately 5% of the time. In that brief amount of time, an expert in LABVIEW was hired to develop the software, and as a result, it was completed on time. The software demonstrated exceptional completeness, fulfilling its designed purpose by seamlessly executing all intended tests. However, there are still areas where enhancements could be made. In Figure 2.6, the primary interface of the software is depicted, featuring intuitive options for managing motor positions, configuring the VNA, and selecting operational modes like near-field test, far-field test, AUT calibration and material characterization.

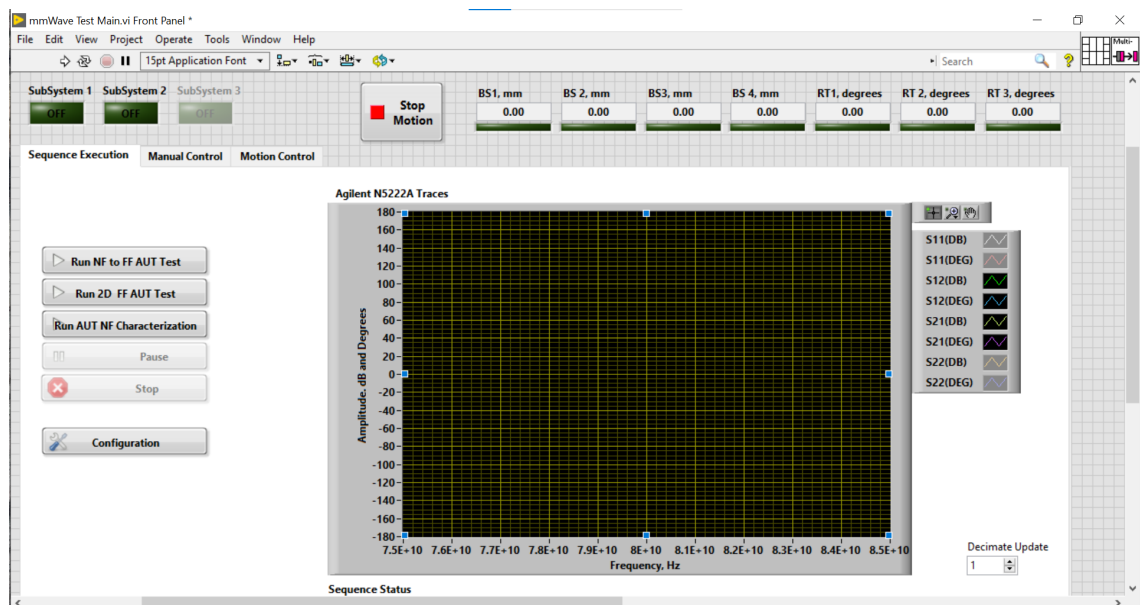


Figure 2.6: Main window of the LABVIEW software shows the operation modes, motor positions, and VNA s-parameters.

2.3 Modes of Operation

The mmWave scanner system was initially designed to perform five different tests, with each test defined as an operation mode of the system. These tests are not only focused on the measurement of antennas but also on dielectric materials and array antenna calibration. Of the five tests, three of them shall be briefly explained.

2.3.1 Near-Field Measurements

In the Near-field measurements test, the AUT is located at the end of sub-system 2, and the probe antenna is situated at the end of sub-system 1. For this process, the software controls both linear positioners LP1 and LP2 to perform sampling every half wavelength of the defined frequency in the software. The type of scanning defined for the system is the raster scan, which can be easily performed with the two linear positioners. The scanning method is called park-and-probe, which means that the probe antenna moves towards the scan position, stops and takes measurements. The probe antenna is positioned from 3λ to 5λ to perform the test, and this distance can be adjusted using linear positioner 4 (LP4). The maximum planar near-field raster scanner window of the system is $0.5\text{ m} \times 0.5\text{ m}$ in the x - y plane. A near-field open waveguide mmWave probe (WR10) with a gain of 6 dBi, operating from 75 GHz to 110 GHz, is mounted on FE1. The linear positioners provide an accuracy of 0.076 mm ($\lambda/36$ at 110 GHz) with repeatability of 0.002 mm. In both FEs (for the probe and AUT), there are rotary tables (RT1 and RT2) that enable polarization rotation

from 0° to 360° with position accuracy of 100 arc-sec and repeatability of 1 arc-sec. To minimize reflections from metallic parts in the scanner, absorbers (C-RAM SFC3) were used. C-RAM SFC3 is rated to provide -50 dB reflectivity at the normal incident angle and -35 dB reflectivity at the $\pm 45^\circ$ incident angle. Fully automated by the software, it returns the position and measurement data. Figure 2.5.b illustrates a picture of the NF scanning setup. The polarization change in the measurement is only done by the probe section (FE1), and it only rotates 90° clockwise facing

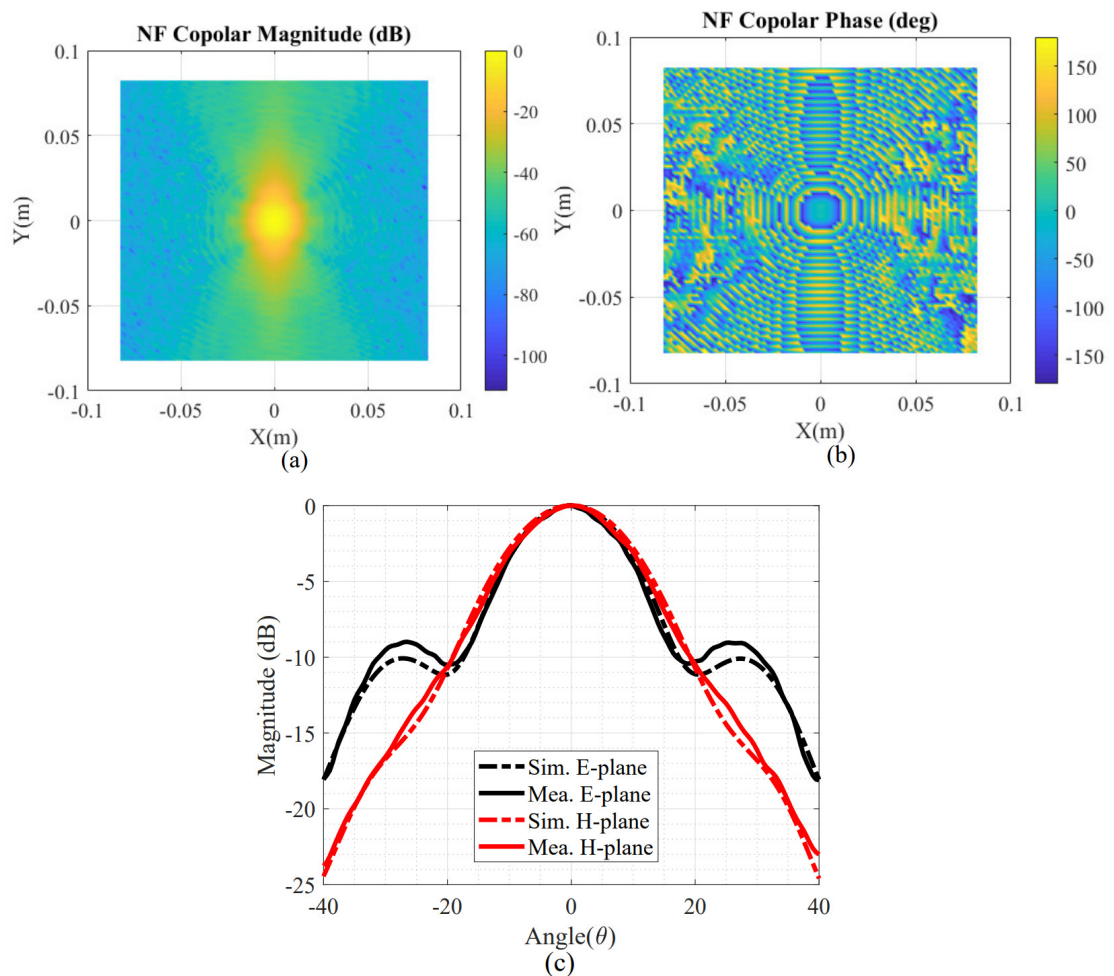


Figure 2.7: a) and b) Near-field results of the NF measurement test of amplitude and phase, respectively. c) E and H plane of the AUT's simulated and measured radiation patterns. Figures adapted from [3].

the probe antenna. Post-processing options, including fast Fourier transform (FFT) processing, phase retrieval, and probe correction, as well as holographic projections for near-field antenna, are available in separate scripts [3].

A test was conducted to validate the performance of the system's NF measurement mode. A W-band pyramidal horn antenna (SAR-2013-10-S2) was used as the AUT. It operates from 75 GHz to 110 GHz and has a typical half-power beamwidth of 16° in the E-plane and 18° in the H-plane at the center frequency. The spacing between the probe and the AUT is 3λ , enabling a $\pm 40^\circ$ far-field angle measurement and a $60 \text{ mm} \times 60 \text{ mm}$ scanning window. Figure 2.7 illustrates the NF results of the AUT collected by the NF system.

2.3.2 Far-Field Measurements

For the Far-Field Measurement, Figure 2.5.c illustrates the setup designed for this test. The AUT is positioned above RT3 so it can rotate on its own axis while the probe antenna, situated on sub-system 1, is elevated using LP1 in order to avoid interference from LP3 and any obstacle between the AUT and the probe. Additionally, both antennas must be perfectly aligned; otherwise, the measurements will represent a wrong cut of the AUT's radiation pattern. Tools like cross laser devices are very helpful for aligning the antennas accurately. For this test, a lens-corrected conical horn antenna that operates from 75 GHz to 110 GHz is used as the probe antenna. This antenna has a gain of 26 dBi with a 3 dB beamwidth of 7° and 9° in the E- and H-planes, respectively. The minimum required distance between

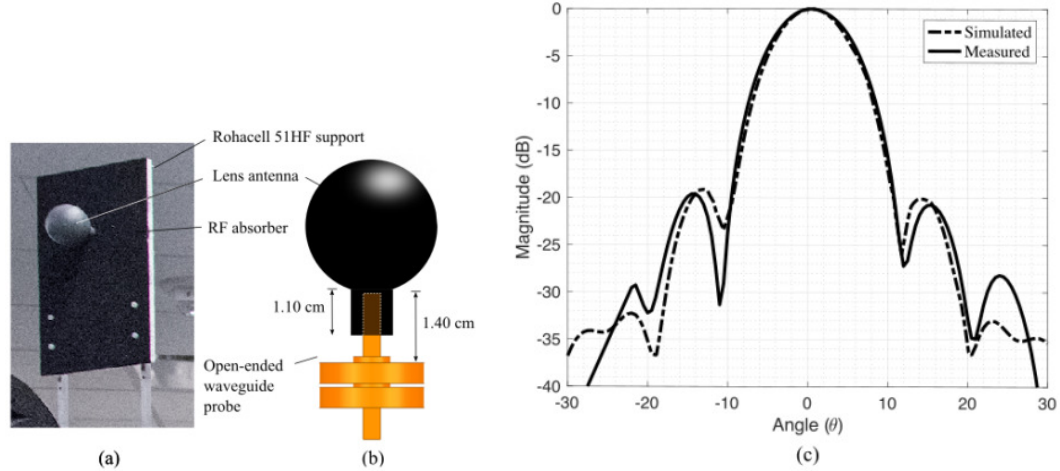


Figure 2.8: Far-field measurement setup and pattern results of a 77 GHz spherical lens antenna: (a) Picture of the antenna lens and setup in FF mode. (b) Lens antenna connected to a WR-10 waveguide used as a feed. (c) FF antenna patterns using far-field measurement data overlapped with simulated results obtained in HFSS. Source: Adapted from [3].

the probe antenna and the AUT is $FF_{limit} = 2D^2/\lambda$, where D is the AUT's maximum dimension. This distance can be adjusted using the LP4 positioner. Another consideration is that the AUT's center must be aligned to the rotary table so the distance between the AUT and the probe antenna remains constant. The validation data collected in the original system was by measuring in the FF region the radiation pattern of a spherical lens antenna attached to a WR-10 open-ended waveguide antenna, which serves as the feed. Figure 2.8 illustrates the setup for the FF measurement test, a graphic illustration of the antenna, and the comparison between the results simulated in HFSS and the measured data.

2.3.3 Material Characterization Measurements

Basically, this operation mode is used to characterize any isotropic dielectric materials. To measure the intrinsic properties of the material (permittivity, permeability, and loss tangent), techniques like TRL calibration and time-domain gating are commonly used in instruments of this nature. And, of course, this mode will also utilize them. The calibration of the VNA is extremely important in this setup because the algorithms used to calculate the intrinsic properties are highly sensitive

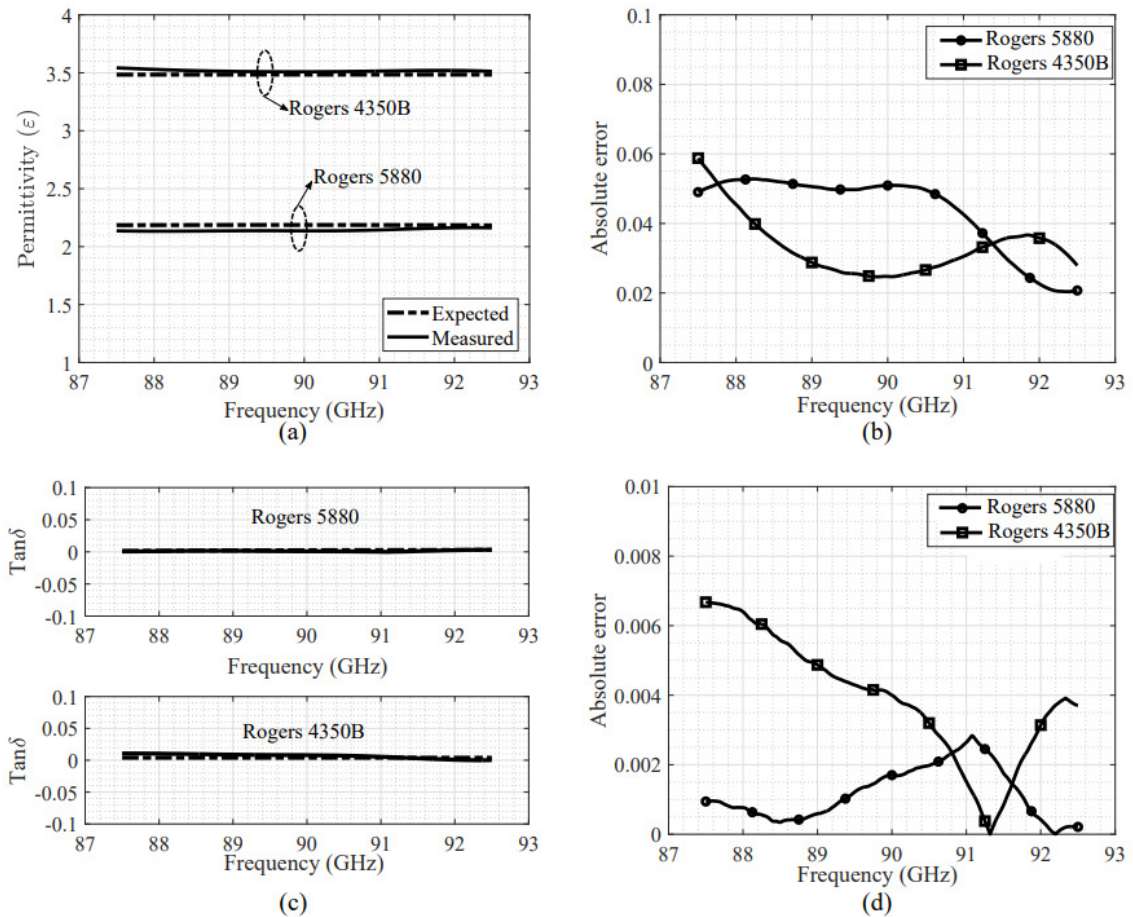


Figure 2.9: Comparison between simulated (HFSS) and measured results obtained in the mm-Wave region: a) Permittivity vs. frequency. b) Error in permittivity vs. frequency. c) Tangent-loss vs. frequency. d) Error in tangent-loss vs. frequency. Figures adapted from [3].

to errors. TRL calibration uses thru, reflect, and line standards to determine and remove the error coefficient terms.

Time gating is used to remove the EM information in the space from the sample to the port, so the data collected would be only inside the material sample. For the TRL calibration, the reflect standard is measured by placing a metal plate between the antennas, and the thru standard is measured by removing the plate (free space). A focused Gaussian beam guarantees a minimum spot size in the middle of the sample that is not affected by the diffracted fields at the edges of the material under testing (MUT). The test uses the s-parameters to evaluate the overall performance of the MUT in the frequency domain. After that, the collected data is processed by different algorithms which can extract the intrinsic properties of the material. The validation measurement for this operation mode was the characterization of two materials: Rogers 5880 and Rogers 4350B. Figure 2.9 shows a comparison of those two materials between the simulated and measured results, where the maximum error is below 1%.

2.4 Summary

A high-technology company named Metawave collaborated with the PAARD team of the ARRC to develop a system capable of multiple tasks of antenna measurements, calibration, and material characterization. This system was designed to measure the antennas they develop in NF and FF regions at mmWave frequencies (W-band). The project was completed in less than 4 months, and the system

possesses 9 motorized positioners (axes), which allows the full functionality of the system and all its operation modes. The system has 3 main operation modes: NF and FF antenna measurements, which allow the measurement of the radiation patterns of the AUT, and material characterization, which allows the measurement of important properties of the MUT like permittivity and permeability. The hardware distribution of the 9 axes is divided into three sub-systems: sub-system 1 is dedicated only to the NF test, sub-system 2 is used for the FF test, and sub-system 3 is mainly used for the MC test. The software used to control the system was developed in LABVIEW. However, due to the limited time in finishing the project, the software presented some limitations. The software worked fine when it comes to configuring the parameters of the measurement and starting the process but did not allow the user to visualize and perform some basic post-processing on the collected data; it only allowed the user to save it. Another limitation was that the GUI was not very well organized, and some configuration entries were hidden. The software also presented some elements in the GUI that had no functionality or did not function as intended. Finally, even though the NF test's results were highly reliable, the operation time of the test was very long. Finally, a validation test was done for each operation mode, which showed a comparison between simulation data and measurement data to determine the reliability of the system.

Chapter 3

System Improvements

3.1 New Graphical User Interface Software

The main objective of this chapter is to develop a new graphic user interface software. Given the widespread use of MATLAB and Python in various scientific endeavors, it was chosen to develop the software in MATLAB for better compatibility. This software allows the user to have much better control over the positioners and VNA configuration, as well as the calculation and input of test measurement parameters, built-in post-processing algorithms, and, finally, better visualization of the measurements and results.

The new software was developed in MATLAB's App Designer application. App Designer is an app-building software that allows the user to easily develop apps based on the MATLAB programming language. The user only needs to drag and drop the widgets into the app environment and define their behaviors. App Designer automatically generates the object-oriented code that specifies the app's layout and design [47].

3.2 Software Description

The designed software must be capable of communicating with four devices simultaneously. Typically, each manufacturer has a software engineering team that develops libraries in various platforms such as Python, MATLAB, or LABVIEW. As mentioned previously in Chapter 2, these libraries were utilized in the previous software. However, in the MATLAB environment, there are no available libraries. Therefore, they need to be developed from scratch to ensure successful communication with the device. Fortunately, all the devices have standard communication protocols with a computer, allowing for effective control of the equipment. In the case of the linear positioners, all nine positioners are controlled by three controller devices (VXM), which communicate with a computer using specific commands. These commands enable the control of the positioners connected to them, allowing for functions such as changing the relative position, absolute position, index position (the current position value of the positioner), speed, acceleration, etc. Utilizing these commands, it is possible to create a library that serves as an interface between MATLAB functions and line command strings.

To construct the line commands, the code must possess the versatility to receive parameters for a specific motor, dynamically assemble the command, and transmit it to the motor's controller. Achieving this simplicity required the implementation of Object-Oriented Programming (OOP). By employing OOP in MATLAB, software complexity can be effectively managed by organizing the code into cohesive components, facilitating maintenance and scalability. This methodology enables

the avoidance of redundant code by creating reusable objects with clearly defined interfaces, thereby concealing the intricacies of the underlying code [48]. Through OOP, it became feasible to virtually construct an object structure for each hardware component of the system. Each motor exhibits distinct properties and is positioned differently relative to its controller, necessitating the software's awareness of these positions. Moreover, a crucial discrepancy in the linear positioner lies in the size of the lead screw, which dictates precise positioning through rotation. However, depending on the positioner model, the spacing between the screw threads may vary, resulting in differences in speed and positional resolution. To ensure precise system control, the software must account for these disparities and store them within their respective objects.

Figure 3.1 shows a brief overview of how OOP was structured in the mmWave scanner system. As explained in the previous chapter, the scanner system comprises a VNA connected to 2 frequency extenders, which fortunately do not need to be modeled in the software as the VNA already has drivers to control them without user interference. The system also includes 3 motor controllers (VXM), each connected to various motorized devices such as linear positioners (also known as bislides in the figure) and rotary tables. Each positioner is assigned an order number in the controller, which is essential for object design in the software. In OOP, an object can contain other objects, so a controller object can have up to 4 motor objects, which may be either bislides or rotary tables. The primary objective of this structural design is to have a single function that can control the position and speed of all positioners in the system, without worrying about the different properties of the

motors and controllers. The object will retrieve the properties and parameters of the other objects inside it and use them to calculate the necessary parameters for building the command that is later sent to the controller to perform the action. The only drawback of the software is that the configuration file, which contains all necessary information about the motorized positioners, must be correct. If there are changes in the connections of the motors in the controller or changes in the models of the positioners, the software will not automatically update the configuration, and errors may occur. Manual configuration updates are required by the user in such cases.

OOP Structure for Motor Control

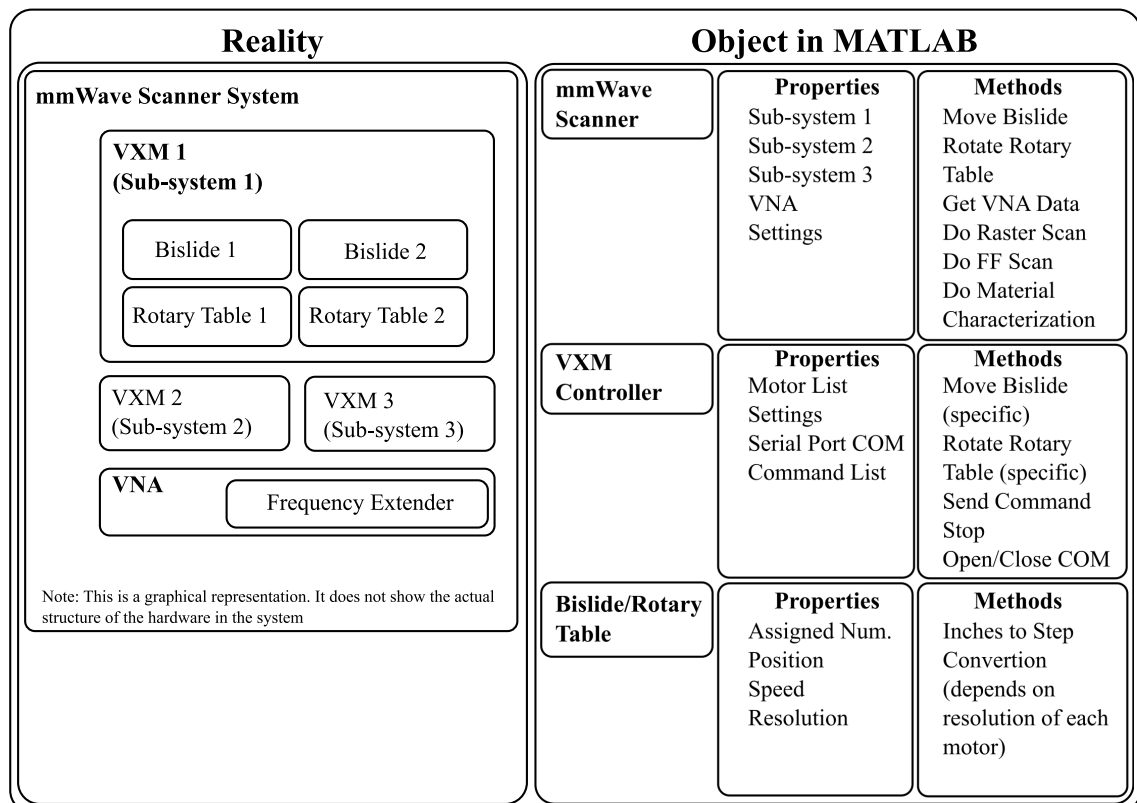


Figure 3.1: Diagram of the structure of the system in reality and its model in the software using OOP.

3.3 User Interface and Scanning Improvements

With the new software structure, developing and organizing algorithms for the testing processes became easier. Consequently, it was also possible to enhance the quality and speed of the tests.

3.3.1 New Graphic User Interface

The new GUI is divided into four main windows. In the first window, all the configurations are located. The parameters for serial communication with the VELMEX controllers can be found, and with one button, the user can connect to all of them. After a successful connection, new configuration entries are unlocked, and the user can move a specific positioner a determined distance and speed. An image shows which motor is selected and the direction of the movement. Additionally, in the same window, VNA connection and configuration options are available. Whenever the user wishes to change VNA configurations, such as the frequency range, number of frequencies, or select the desired S-parameter (S12 or S21), all those options can be found in this window. Figure 3.2 shows a picture of the main window configurations, while Figure 3.3 displays the near-field setup window, which allows the user to control the motors commonly used for the alignment of the AUT or probe antenna, as well as the distance between the two antennas. It also calculates the scanning windows and the position grid where the samples must be collected. Finally, it configures the polarization and the scanning method, which are park-and-probe or continuous scanning.

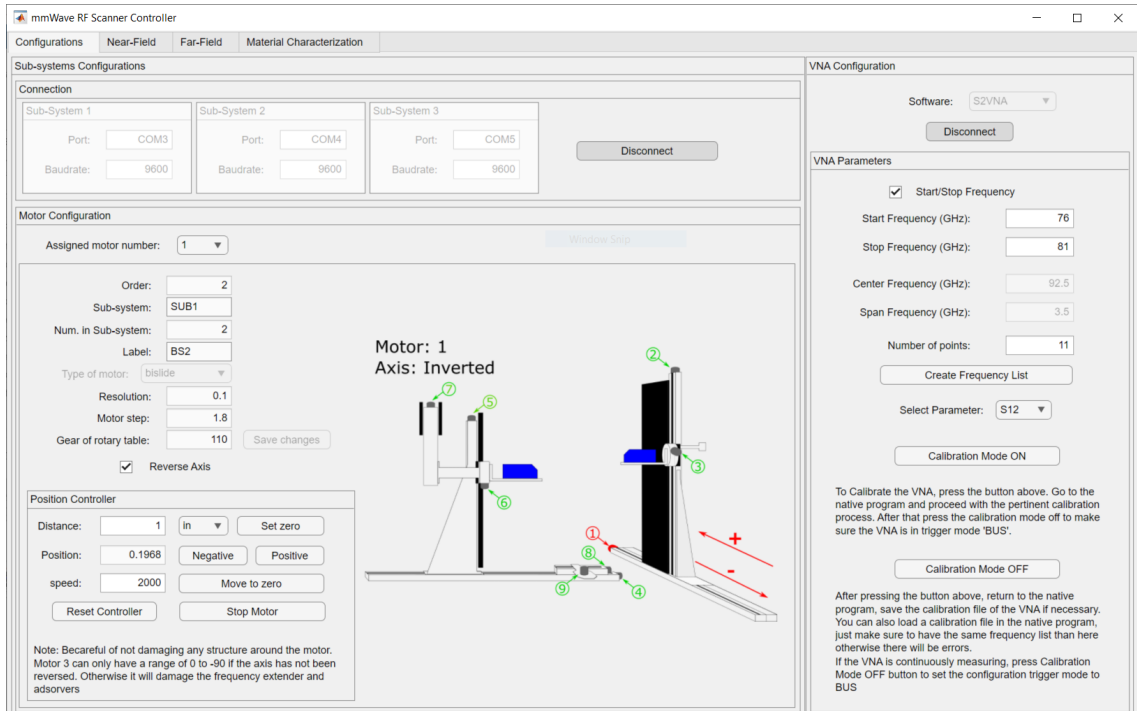


Figure 3.2: New GUI main window tab for connection and configurations to the VELMEX controllers and the Copper-mountain VNA.

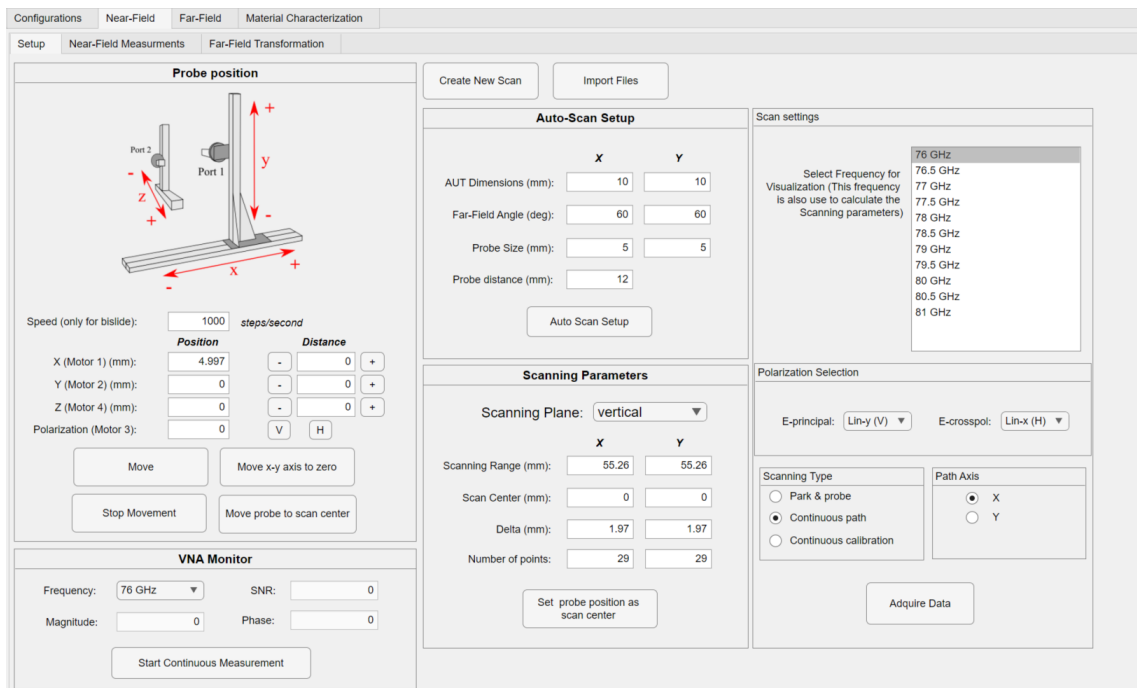


Figure 3.3: New GUI near-field setup window, scanning range and position grid calculations are located in this window.

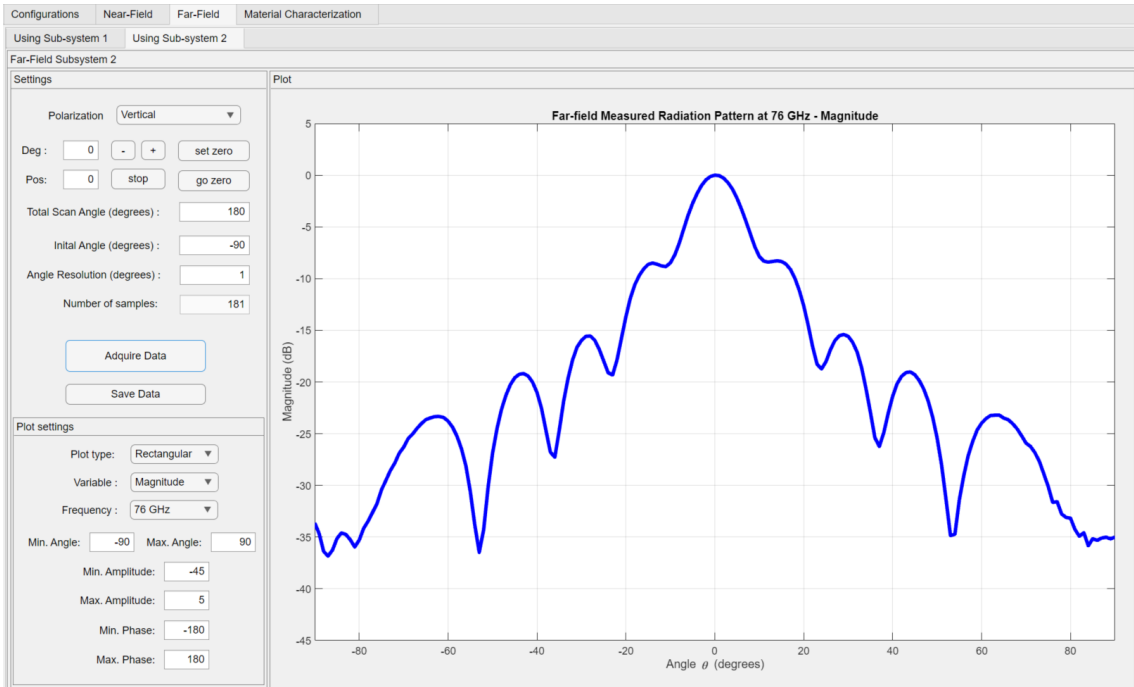


Figure 3.4: New GUI far-field setup window, configures the angle range, resolution and polarization.

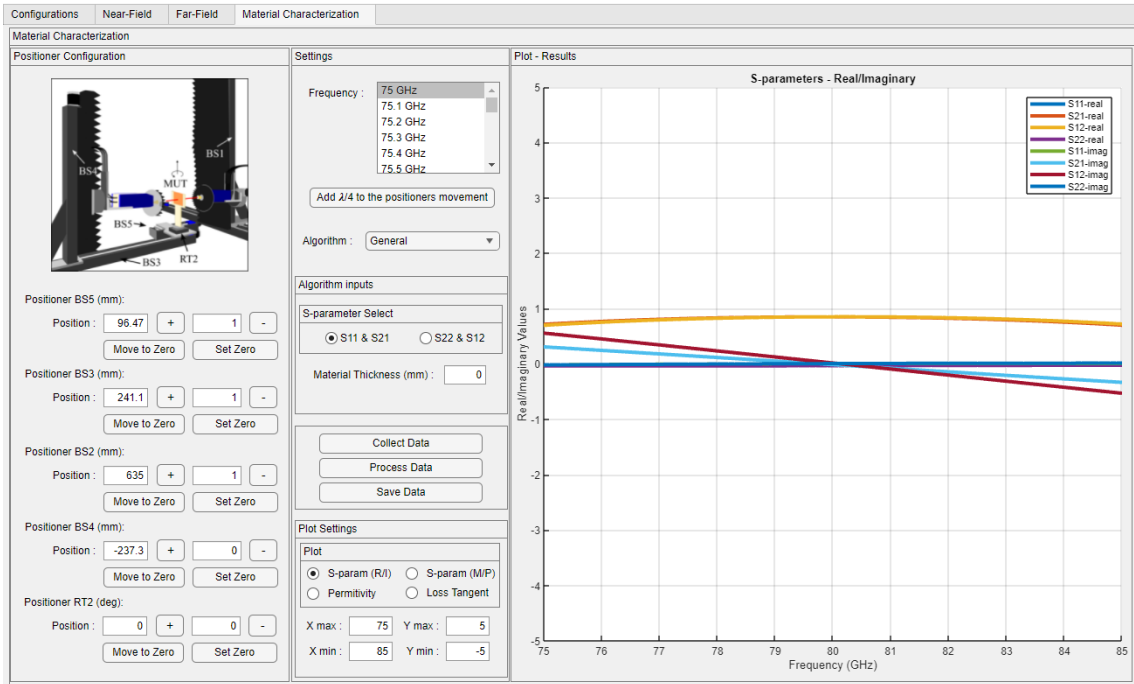


Figure 3.5: New GUI material characterization setup window, configures the motors' position for alignment and calibration, and visualizes the s-parameters collected from the VNA.

The next important window is the far-field configuration and data acquisition window, as depicted in Figure 3.4. In this window, the GUI allows the user to control the rotary table responsible for performing the FF measurement test, crucial for precise alignment. It also configures the total scanning angle and the angle resolution. The software is also capable of displaying the measurements in both magnitude and phase in real-time. Finally, there are some basic plot controls for user visualization of the results and data storage in a file.

Finally, Figure 3.5 illustrates the material characterization setup window that was designed. This window, like the others for different operation modes, allows the control of five different motors: 4 linear positioners for aligning the antennas and calibrating the VNA, and the rotary table for rotating the sample at various angles for incident angle measurements. It also calculates the $\lambda/4$ of a specific frequency, which is important for VNA calibration. This operation mode does not require real-time data collection, but it immediately displays the s-parameters that will be used to calculate the intrinsic properties of the material. Lastly, there are basic plot control settings.

3.3.2 Near-Field Scanning Improvements

In contrast to the previous software, which only permitted park-and-probe measurements, wherein the probe halts at each measurement position to enable precise measurements, the time required to complete a raster scan in one direction was considerable. If the user desired to conduct dual-polarization scanning, the time would double.

It is possible to view the collected data in real-time, displaying the magnitude and phase at a specific frequency in a spatial distribution, represented on an x - y axis plane where the samples were collected. Figure 3.6 demonstrates the software collecting near-field data of the antenna at 75 GHz, showcasing both magnitude and phase in real-time.

As previously mentioned in Section 2.2.2, the post-processing algorithms were performed outside the UI program, in separate scripts where the saved data is loaded and processed. The inconvenience with this method is that the user must have some level of understanding in order to operate the script, to find where or what parameters are going to be used and change them properly. In the newly developed GUI, the post-processing algorithms were incorporated, and all the parameters needed

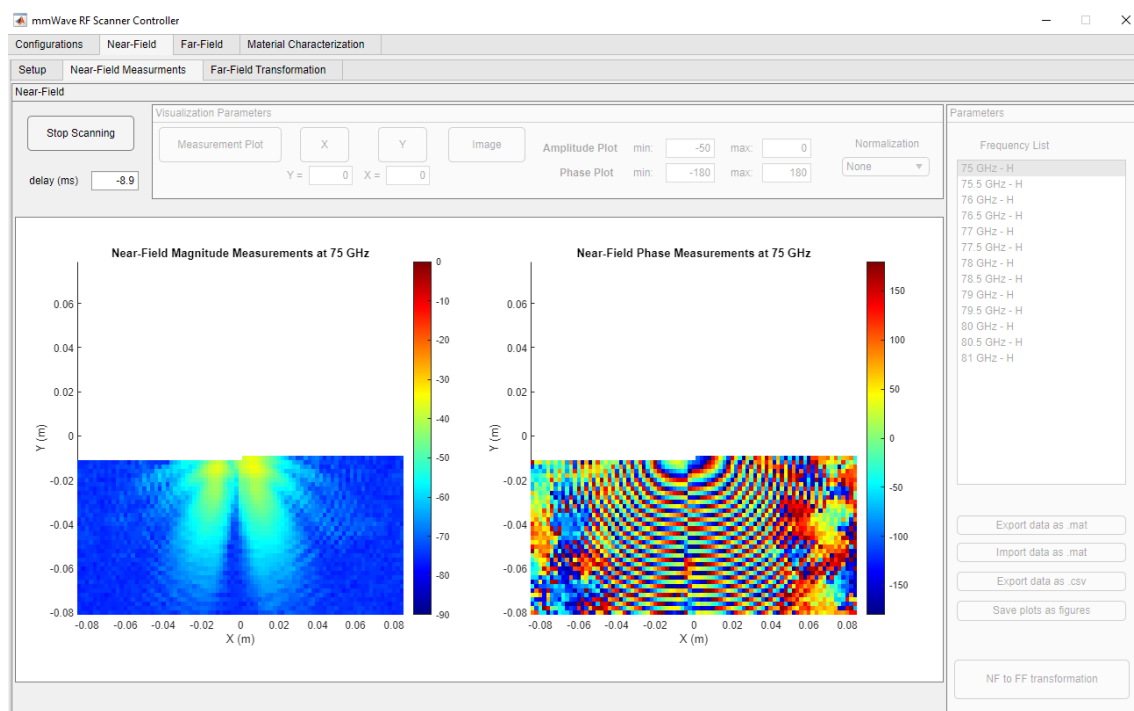


Figure 3.6: Near-field measurement in progress of a horn antenna at 75 GHz in cross polarization.

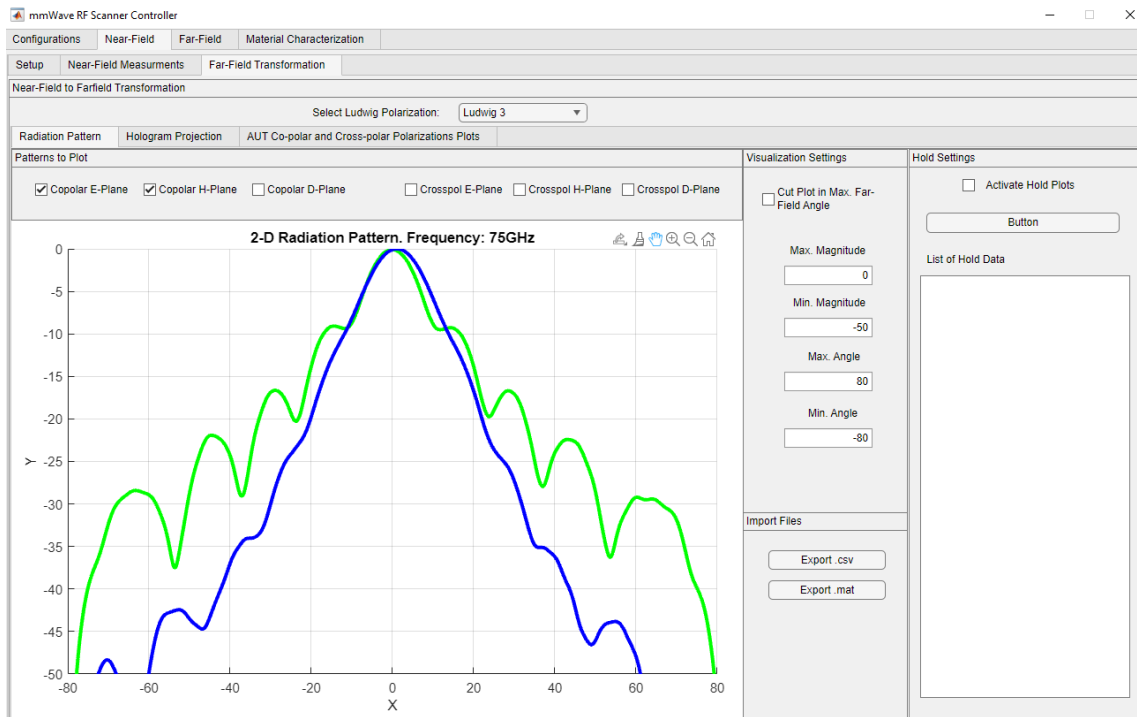


Figure 3.7: GUI tab window in the Near-field section that shows the measured radiation pattern.

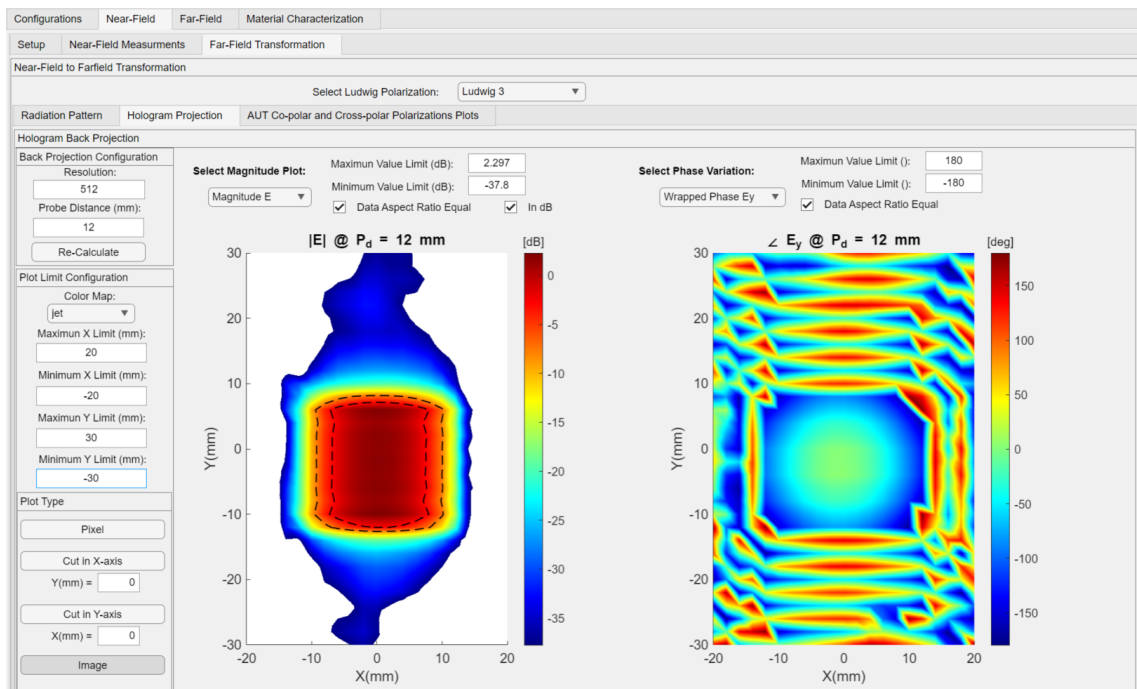


Figure 3.8: GUI tab window in the Near-field section that shows the hologram back projection results.

for the algorithms are displayed in the GUI. Figure 3.7 and Figure 3.8 show the GUI window for both the NF to FF transformation results and holographic back projection, respectively. The window allows the user to select which plane of the calculated radiation pattern is being shown. It also enables loading previously stored files to display comparisons in the graphic plot.

3.3.3 Raster Scanning Algorithm Improvements

Originally, due to software limitations in LABVIEW, the raster scan algorithm was restricted to only one method, similar to a calibration method known as park-and-probe [22], [20]. This method involves moving a linear positioner that holds the antenna probe to a specific location, stopping, and then collecting data from the VNA (s-parameters in amplitude and phase). Subsequently, it moves to the next location, typically $\lambda/2$ in either the x or y direction. Although this method has demonstrated high measurement precision, it is also extremely time-consuming. The high precision is attributed to the probe triggering and collecting VNA data numerous times at each position, followed by averaging the data. Averaging reduces errors induced by environmental noise.

There are some solutions to reduce the duration of the process. One of those methods is performing a continuous scan. In other words, instead of stopping at every position, the main software synchronizes the movement of the positioners and the VNA data collection trigger to collect the data at a specific probe position. For the mmWave scanner system, there used to be two possible solutions that allow the NF system to collect data continuously. One of them is to add special hardware

offered by VELMEX, which is the encoder. This device is installed in the positioner's hardware as an add-on, and its purpose is to accurately measure the current position of the motor with a resolution of $1\mu\text{m}$. However, the downside of this hardware is that the encoder controller is also very slow to send the position to the computer because the computer has to ask for the position from the encoder every time instead of the encoder constantly sending the information. This two-way communication requires reducing the speed of the positioner to a point where it is as slow as the park-and-probe method. Due to this drawback, the most viable option is to use MATLAB tools and create an algorithm to synchronize the timing of the positioner movement and the trigger signal sent to the VNA.

The motion of VELMEX linear positioners, like many other positioners, follows a uniformly accelerated rectilinear motion (UARM). This means that the path the positioner follows does not have a constant speed, but there are sections where there is acceleration and deceleration (see Figure 3.9.a). This is critical for synchronizing the data collection timing because if this acceleration is not taken into account, there will be a delay in the sampling in each row of the raster scan grid. In order to avoid this variable speed section, the solution is simple. The software calculates the sample positions using the AUT dimensions, probe size, desired FF angle, and probe distance from the AUT. With these parameters, the software calculates the scanning window and sample positions with a spacing of $\lambda/2$ (default). In the case of performing the scan in the x direction, the software will only use the first and last points of the row and all the points in the column. Figure 3.9.b shows, in red dots, the first and last sampling points of the raster scan grid. Then, using the basic

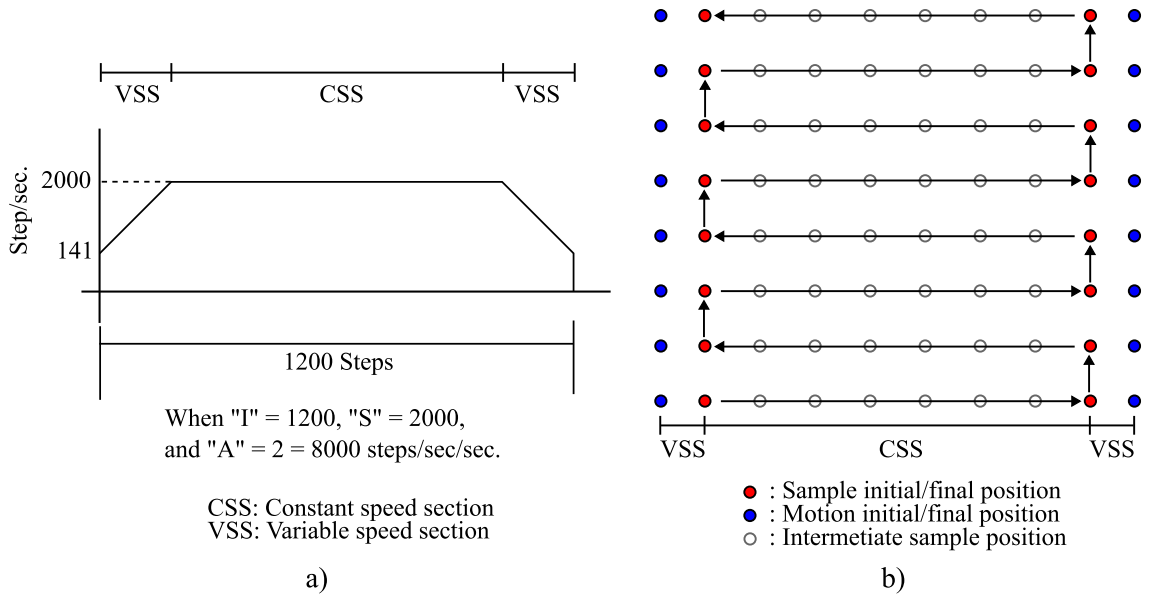


Figure 3.9: a) The trapezoidal speed profile of the VELMEX motor showing the sections where the speed is variable and constant. b) Raster scan sampling and motion positions

equation of the UARM, the distance and time where the speed is variable can be calculated.

$$\Delta x_{VSS} = \frac{v_f^2 - v_i^2}{2 \cdot a} \quad (3.1)$$

$$t_{VSS} = \frac{v_f - v_i}{a} \quad (3.2)$$

Where Δx is the distance where the speed is variable, and t is the time, with v_f and v_i representing the final velocity and initial velocity respectively, and a representing the acceleration. The acceleration of the VELMEX motors is configurable, with this configuration provided by the user in a command and the values ranging from 1 to 127, representing 7 bits. VELMEX has measured and defined accelerations and initial velocities for each value of the acceleration configuration (see Appendix A). For example, for an acceleration of 2, this means that the initial speed is 141

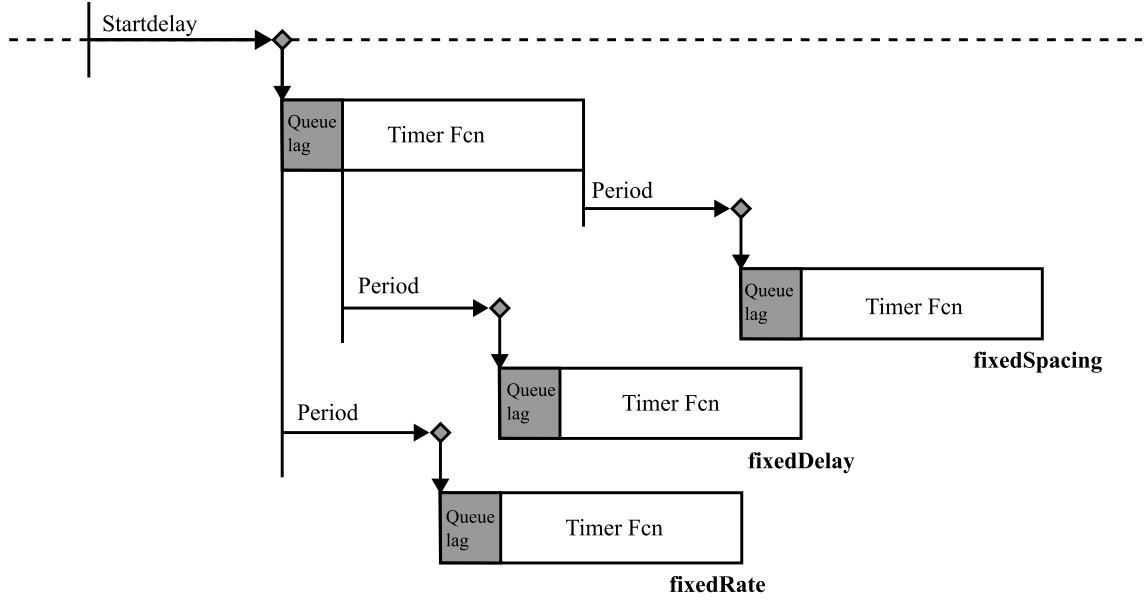


Figure 3.10: Timer object schedule configuration for multi-execution mode. Figure adapted from [4]

steps/s, where "steps" is a unit representing the rotations of the motor, and an acceleration of 8000 steps/s^2 (Figure 3.9.a). However, it is recommended to use low values for acceleration to avoid synchronization issues between the motor and the controller.

Once those values were calculated, the distance Δx_{VSS} was added to the initial and final sampling positions. In Figure 3.9.b, these positions are represented as the blue dots. To synchronize the sample trigger with the position of the probe, MATLAB has an object called a timer, where one of its configurations allows a function to be called every defined period of time [4]. This function will trigger, collect, and store the data from the VNA.

The timer object has four configurations that trigger the callback function differently. Three of them are used for multi-execution mode, which means that the timer function is called every certain period of time. Figure 3.10 shows the behavior of all

three configurations. The three configurations include `fixedSpacing`, which initiates the next cycle after a set duration following the conclusion of the preceding cycle. `FixedDelay` triggers the subsequent cycle after a specific time has elapsed since the commencement of the prior cycle, without accounting for any queue lag. Lastly, `fixedRate` commences the next cycle after a predefined interval from the start of the previous cycle, considering the queue lag. This feature of the timer is important because it greatly affects the timing of the measurement if it is configured incorrectly. To achieve a precise sampling frequency, the `fixedRate` configuration, illustrated in the figure, is used. However, due to the computer running other background processes, there is a queue lag that might disturb the period of the timer, reducing the precision of the sampling and causing some issues at the moment of sampling.

3.3.3.1 Continuous Raster Scanning Queue Lag Issue

After developing the code for the continuous raster scanning algorithm, it underwent immediate performance testing. The results are depicted in Figures 3.15.c and 3.15.d, illustrating the NF scan test results in magnitude and phase, respectively. The graphs reveal significant inconsistencies among the measurement rows. This inconsistency introduces substantial errors in the radiation pattern after the NF to FF transformation, as elaborated in Section 3.4.1. To address this issue, several approaches were pursued. Initially, it was suspected that the imprecision lay in the time required for acceleration. Consequently, a manual time delay offset was introduced, temporarily resolving the problem. However, subsequent modifications to the scan settings, such as altering the AUT and scan window dimensions, necessitated

Table 3.1: Average period of the last 10 measurements corresponding to Figure 3.11.a and b.

Calculated period (ms)	Average period (ms)	Difference (ms)
350	362.26	12.26
350	361.67	11.67
350	361.62	11.62
350	362.16	12.16
350	361.54	11.54
350	362.44	12.44
350	361.32	11.32
350	361.38	11.38
350	361.76	11.76
350	361.33	11.33

recalibrating the offset, a time-consuming process. Eventually, the park-and-probe scanning method proved more effective. Alternatively, reducing the scanning speed eliminates misalignment as a concern. However, this solution also compromises the method's ability to achieve its primary goal of reducing scanning time. Fortunately, MATLAB's timer object offers a method to measure the real average period of the timer. It revealed that the measured period slightly differed from the calculated period. To better visualize the period error, a new process was programmed to conduct a pseudo raster scan, with the only difference being that the probe doesn't move along the axis perpendicular to the continuous scanning axis; instead, it moves

only back and forth. This allows for a comparison of rows in the measurement that are expected to be highly similar. Figures 3.11.a and 3.11.b illustrate the problem, and the measured period of the timer is presented in Table 3.1. During this test, the probe moved horizontally, collecting 81 samples via the timer function. After 20 row measurements, the difference between the actual period was approximately 10 ms. This delay accumulates with each sampling, resulting in misalignment in the rows of the plot.

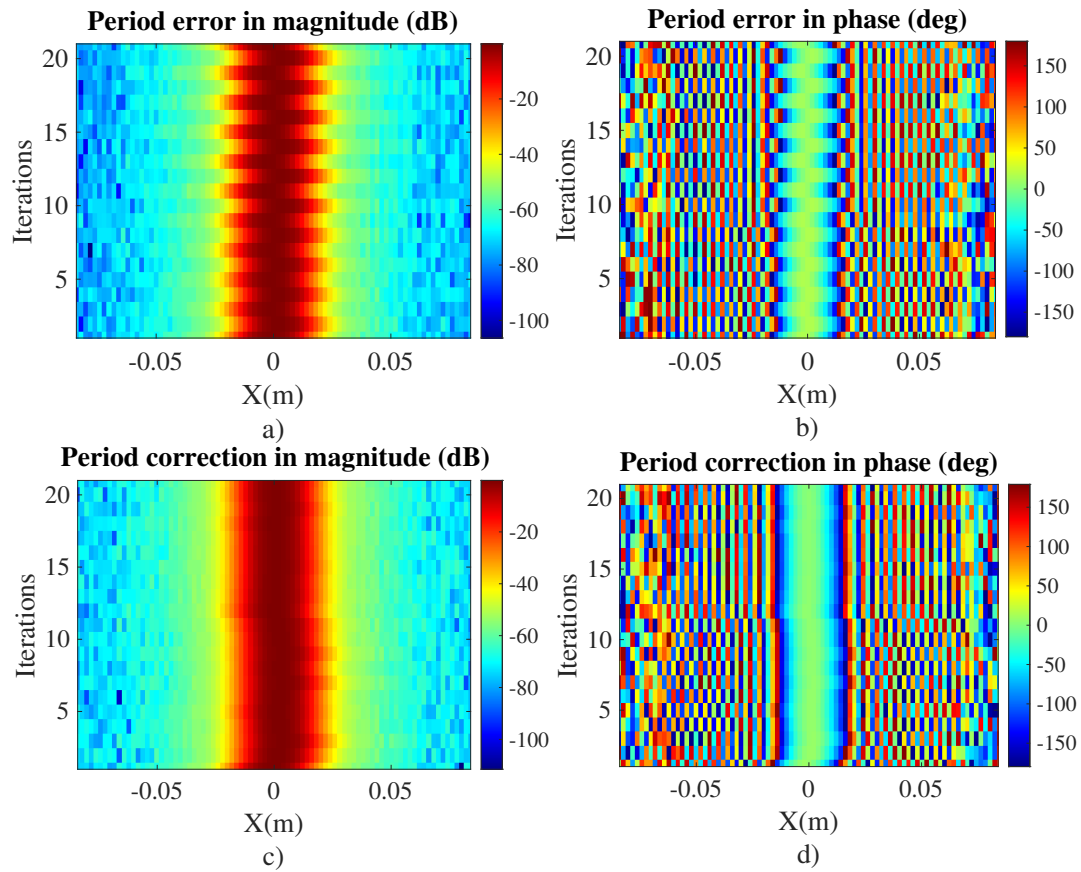


Figure 3.11: a) and b) present the magnitude and phase, respectively, of measurements conducted with the probe moving back and forth along the same row, demonstrating the error in timer period. Similarly, c) and d) showcase the magnitude and phase of the identical process, incorporating the application of Equation 3.3.

An algorithm to correct this period error became necessary. Initially, an averaging method was employed. This involved taking all the difference values in Table 3.1, averaging them, and subtracting the result from the calculated period, which was then used to configure the timer. However, this approach proved inefficient because of the irregular lag of the computer; consequently, the corrected value failed to precisely adjust the period. Subsequently, a simple iterative process was developed. In each row measurement, Equation 3.3 was applied to obtain an average period as close as possible to the calculated period, which represents the ideal value.

$$Pd = Pc + \sum_{i=1}^m (Pc - Pave_i) \quad (3.3)$$

Where m is the current iteration in the iterative process of the period calibration, Pc is the calculated period for the sampling, $Pave_i$ is the measured period of the timer after a sampling process, and Pd is the new period correction that will be configured into the timer for the next sampling process. To test this calibration algorithm, the same process was used as previously, and the results are shown in Fig 3.11.c and d, which illustrate much better alignment in the measurements of magnitude and phase. Table 3.2 shows less difference between the calculated period and the average period of the timer. This method proves to be better at finding a period correction value that is applied in the NF continuous scanning.

3.3.4 Far-field AUT Holder Structure

In the case of the Far-field operation mode, the frequency extender 2 (FE2) must be moved and attached to the rotary table at the peak of subsystem 2. For the tests in Chapter 2, a support was built to accommodate the AUT. However, only that specific AUT fits on that support. Furthermore, the aforementioned support is no longer available, so a new support structure was designed.

The only requirement for this design is that it must support the frequency extender, which weighs 2.2 kg according to its specifications, and the AUT holder must slide a certain distance across the center of the rotary table, so the AUT's

Table 3.2: Average period of the last 10 measurements corresponding to Figure 3.11.c and d.

Calculated period (ms)	Average period (ms)	Difference (ms)
350	351.53	1.53
350	347.72	-2.28
350	352.89	2.89
350	348.05	-1.95
350	354.33	4.33
350	348.18	-1.82
350	352.13	2.13
350	347.21	-2.79
350	353.12	3.12
350	346.53	-3.47

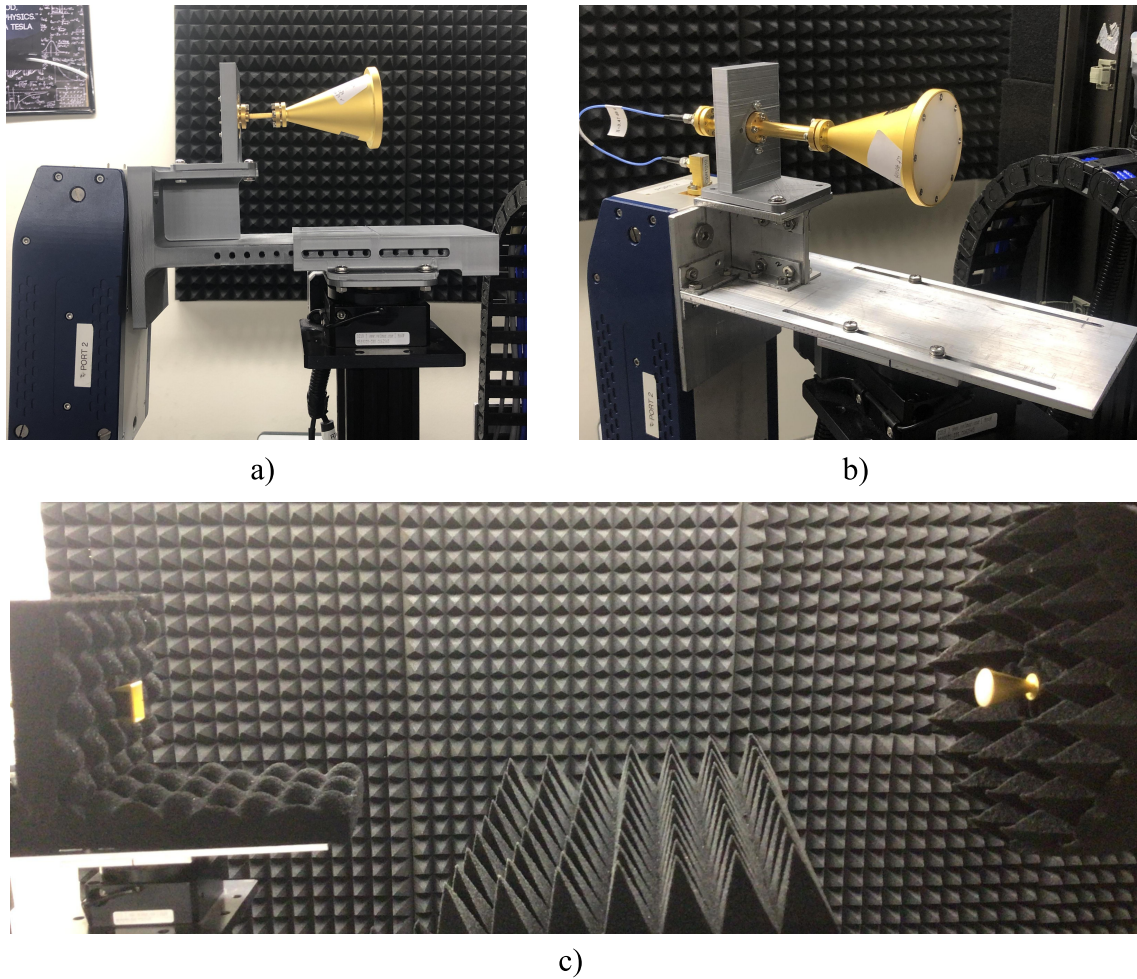


Figure 3.12: a) First prototype of the AUT holder structure, 3D printed made by a combination of PLA and ABS. b) Second prototype of the AUT holder structure made with aluminum. c) Photo of the complete far-field setup featuring both AUT and the probe antenna.

center can be positioned on the axis of rotation. The first prototype was designed using SolidWorks, a computer-assisted design software. The structure consists of 4 parts: the attachment to the rotary table, the slider holder, the FE carrier, and the AUT holder. Once the design was finished, it was 3D printed using a Bambu Labs x1 Carbon printer. Initially, it was printed using Polylactic acid (PLA) material. However, this material breaks if the piece bends past a certain point of tolerance. Therefore, acrylonitrile butadiene styrene (ABS) material was used; it is stronger

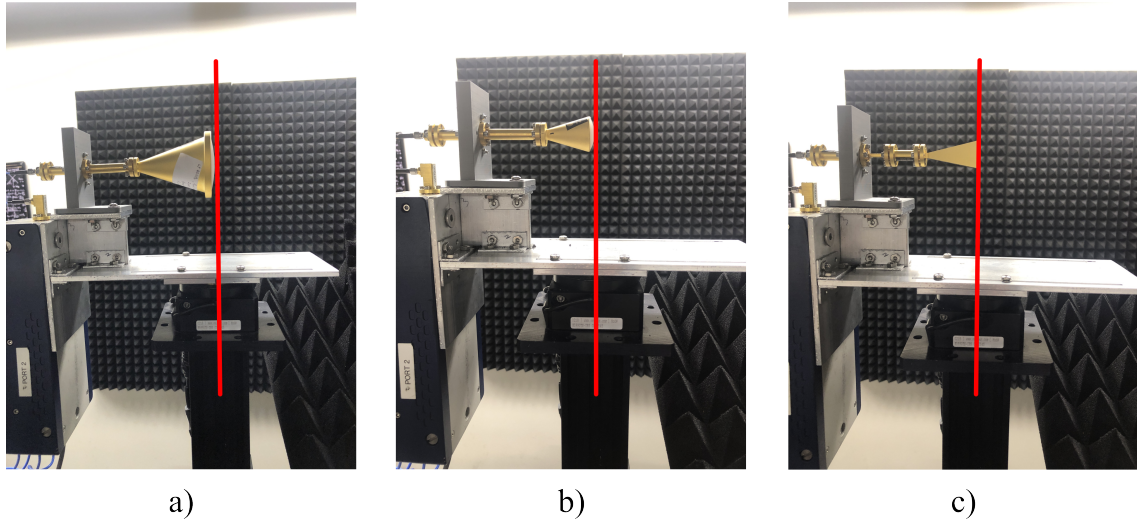


Figure 3.13: The AUT holder structure accommodates various antennas installed as AUTs, each centered to the rotating axis. The antennas include: a) WR10 Spot Focused Horn Lens Antenna (SAQ-903071-10-S1). b) WR10 Lens Corrected Antenna (SAL-7531142607-10-S1). c) WR12 Pyramidal Horn Antenna (SAR-2309-12-S2) [5].

and more durable than PLA. Figure 3.12.a shows a photo of the first prototype 3D printed with ABS material, which successfully allowed the alignment of the AUT's center to the rotation axis. However, the structure experienced bending due to the weight and torque contributed by the FE, though the material managed to withstand without breaking. Nonetheless, the possibility of breakage remained, and the bending caused an offset in the direction the AUT faced. Due to this issue and utilizing the same approach as the previous design, a second prototype was built, this time using aluminum. The sturdiness of the metal resolved the weight and bending problem, as depicted in Figure 3.12.b. The functionality of aligning the AUT's center to the rotating axes using different antennas of varying sizes is illustrated in Figure 3.12. Finally, absorbers were added to avoid electromagnetic reflectivity on the metallic structure, and the setup is now ready for data collection and antenna radiation pattern measurements, as shown in Figure 3.12.c.

3.4 Results, Comparison and Validation

In this section, the results of the antenna measurements, specifically the NF and FF tests, will be presented and analyzed.

3.4.1 Near-field Test Measurement Results

To validate the performance of the NF system, a standard gain horn (SGH) antenna (SAR-2309-12-S2) was placed under testing. The dimensions of the antenna are 27 mm x 20 mm, with a FF angle of 80° , and a distance between the AUT and the probe is 3λ . The scanning window was calculated using Equation 2.4 at a frequency of 75 GHz, where $\lambda = 2$ mm.

Figure 3.14.a and Figure 3.14.b illustrate the results in magnitude and phase, respectively, of the NF test using the park-and-probe scanning mode. Figure 3.14.c and d both show the same magnitude and phase measurement but with the difference that these results were obtained in cross-polarization, respectively. Figure 3.14.e shows a comparison between the FF pattern obtained from the NF results by using the NF to FF transformation algorithm and the simulated antenna patterns that can be found in its datasheet [5]; it also shows the cross-polarization patterns of the antenna. The traces of both simulated and measured data in the E-plane have a high similarity, while in the H-plane, there is a more noticeable difference in the patterns at angles below -20° and above 20° . These results partially support the reliability of the system in NF test measurements with the park-and-probe method.

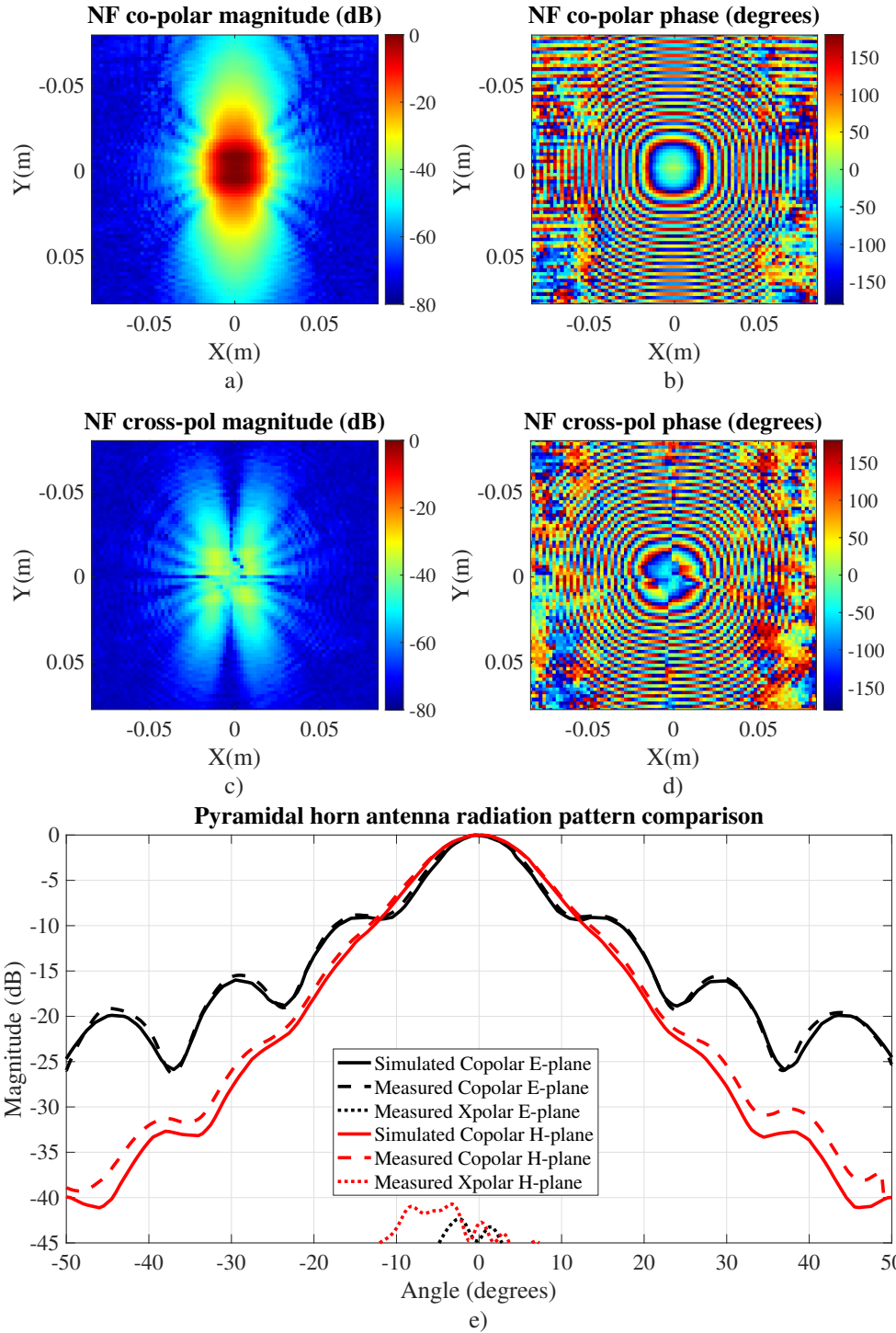


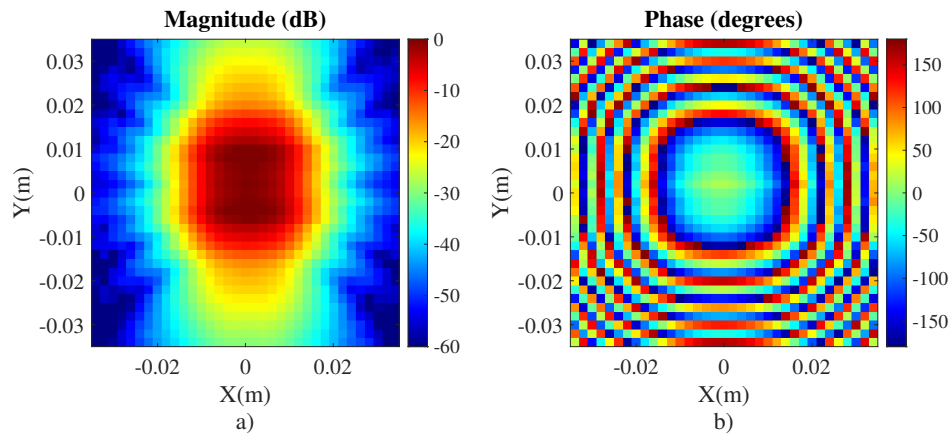
Figure 3.14: a) NF magnitude results of the SGH in dB. b) NF phase results of the SGH in degrees at 75 GHz. c) and d) are the magnitude and phase of the cross-polarization measurement of the SGH at 75 GHz respectively. e) SGH radiation pattern comparison between simulation and measurement in both E- and H-planes.

The discrepancies with the H-plane pattern are later discussed by comparing them with the FF results in Section 3.4.2.

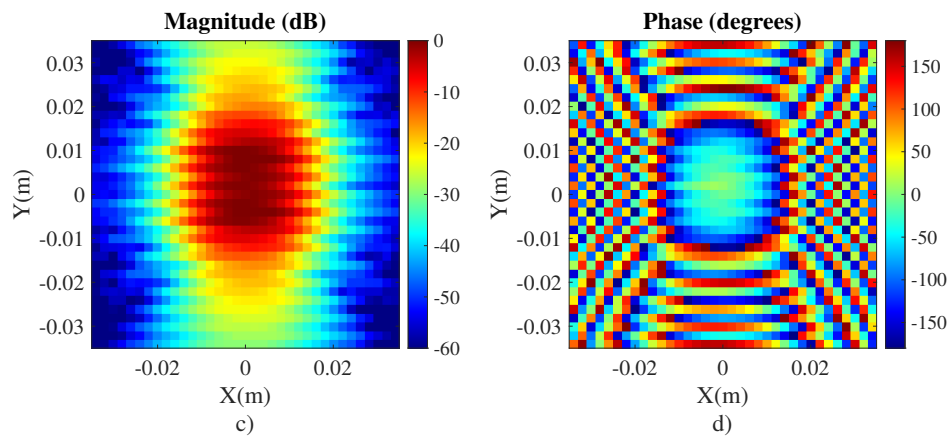
In order to measure the performance of the continuous raster scan type, other measurements were performed. The following results show the impact of the non-period corrected continuous scan method. Figure 3.15 shows a comparison of the NF measurement between the continuous scan with and without period correction, with the park-and-probe results used as reference. Figure 3.15.c and d show the NF results without period correction. In those two figures, there is a noticeable discrepancy between the rows. The graphics do not form a defined shape but appear to have an offset in the collected data of each row of the plot. This offset, caused by the real increased period of the timer object (Table 3.1), actually has a high influence on the calculated radiation pattern.

Figure 3.16 illustrates the radiation patterns of the previously mentioned NF results. In the case of the E-plane, which corresponds to the plane equivalent to the y -axis in the plots, the pattern results are highly similar. This is because the spacing in the data of the y -axis is exactly half- λ for every measurement. The difference lies in the H-plane, which is represented by the x -axis in the NF results. In the case of the non-corrected period, there is a significant difference compared to the H-plane data of the other methods. These results demonstrate two important points: the importance of period correction to the timer object, and that the corrected continuous scanning FF results are highly similar to the pattern of the park-and-probe method, raising doubts about the results of the AUT simulated radiation pattern obtained from its datasheet.

Park-and-probe mode NF copolar measurements of horn antenna at 75 GHz (Reference)



Continuous mode NF copolar measurements without period correction



Continuous mode NF copolar measurements with period correction

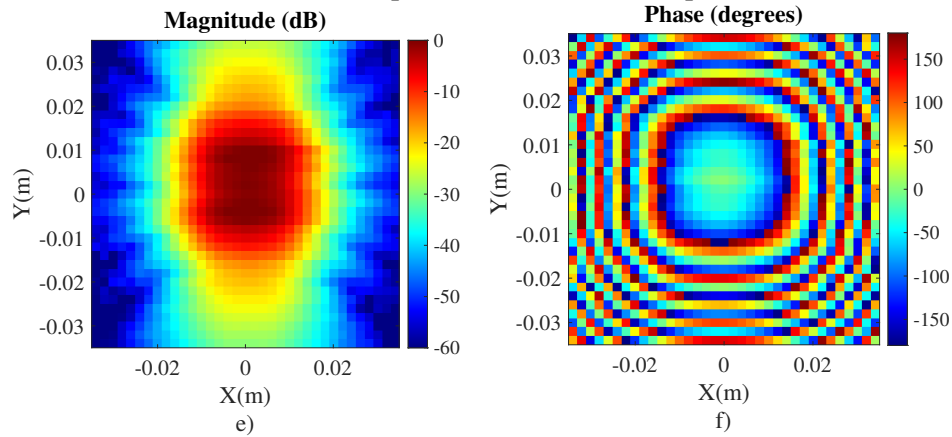


Figure 3.15: a) and b) are the NF-P results in magnitude and phase respectively of the SGH antenna (SAR-2309-12-S2) which is used as reference. c) and d) are the NF results of the continuous method without any period correction. e) and f) are the results of the same method applying a period correction.

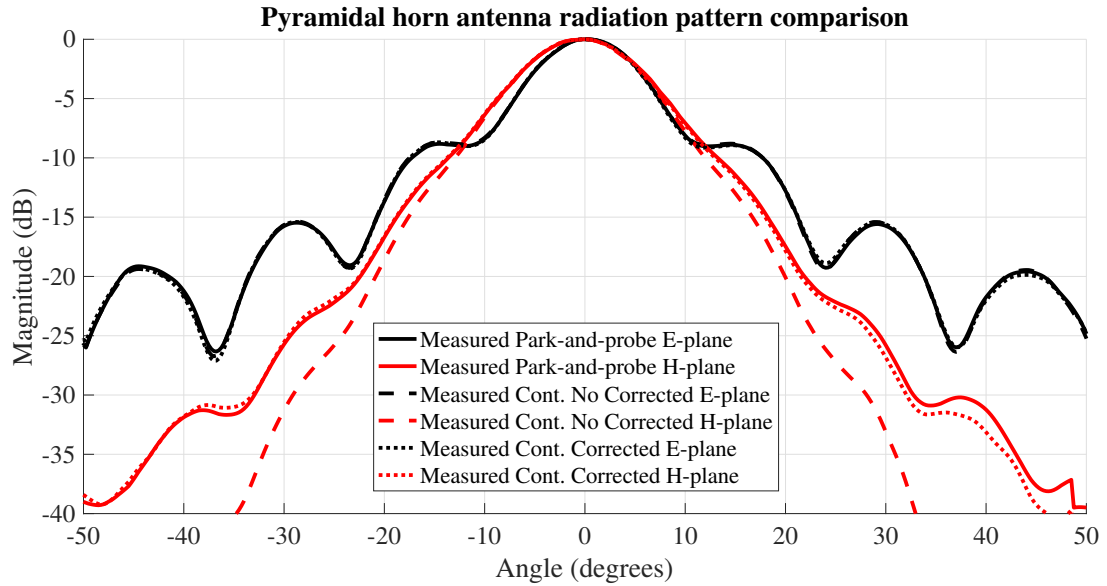


Figure 3.16: Radiation patterns of the NF data illustrated in Figure 3.15, it shows the park-and-probe method, the continuous method with and without period correction.

Table 3.3: Antenna NF measurements records, showing the total number of samples and a time comparison between the continuous and park-and-probe methods.

AUT description	Num. of samples (X x Y)	Total num. of samples	Time in continuous (mins)	Time in park-and-probe (mins)	Times faster
Horn antenna	29x27	783	5.09	13.06	2.56
AiP measurement	28x29	812	5.30	13.01	2.45
AiP measurement	33x34	1122	7.20	17.70	2.46
Horn antenna	27x82	2214	13.28	37.77	2.84
Horn antenna copol	85x80	6800	42.22	109.66	2.60
Horn antenna xpol	85x80	6800	42.81	116.73	2.73
Horn antenna	87x82	7134	42.69	110.77	2.59

Finally, the main goal of the development of the continuous scanning process is to increase the speed of the scan without compromising the reliability of the results. As previously illustrated in Figure 3.16, the reliability of the results is assured. Table 3.3 shows some records of NF measurements performed by the system. This table displays the total number of points or samples, the duration of the test with each method, and a factor that describes how much faster the continuous method is over the park-and-probe method. On average, the continuous method is 2.6 times faster than the park-and-probe method, achieving the objective of the process.

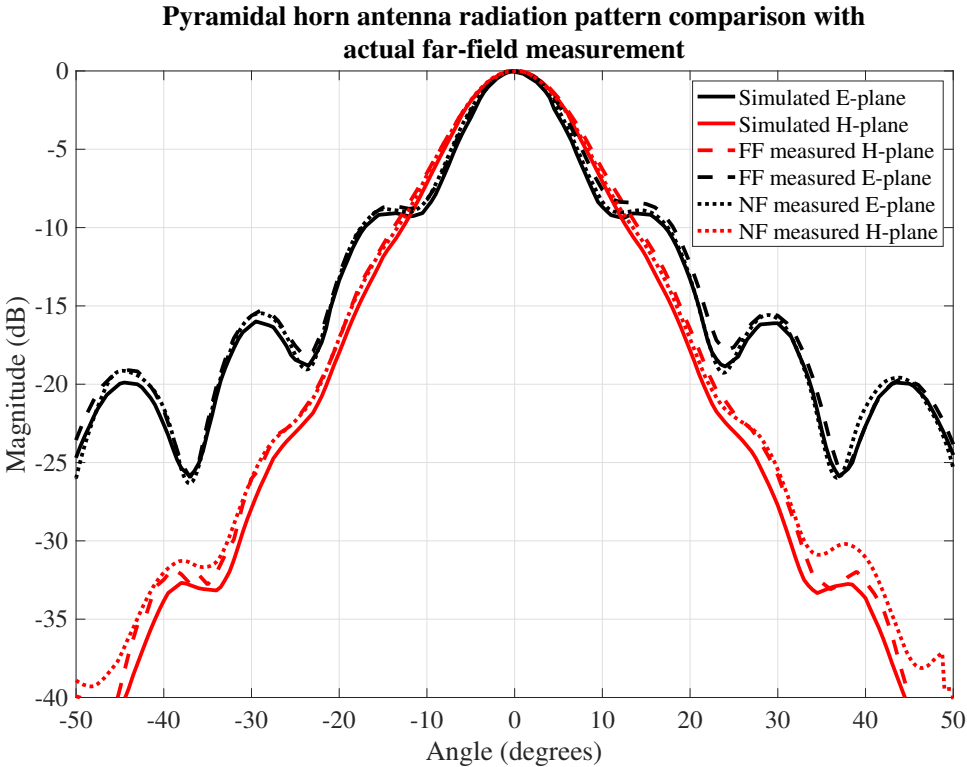


Figure 3.17: Radiation patterns of the pyramidal horn antenna between the simulation, near-field and far-field results.

3.4.2 Far-field Test Measurement Results

The results obtained with the FF setup described in Section 3.3.4 show some interesting patterns. Figure 3.17 illustrates the radiation patterns measured using the near-field and far-field measurement tests and simulation data extracted from the AUT's (SAR-2309-12-S) datasheet. The plot demonstrates high similarities in the results of the E-plane, indicating outstanding reliability of the results in this plane. However, as discussed in the previous section, discrepancies in the results of the H-plane were high, especially in angles far from the center (0°). Figure 3.17 shows that the NF and FF results overlap their traces in the H-plane from -33° to 33° in the plot. However, in outer angles, the line of the pattern obtained with the FF test starts to deviate. It is believed that this discrepancy in the results in the outer angles of the plot is due to the low values in magnitude, where floor noise interference starts to affect the measurements and disrupts the phase of the collected s-parameters. Additionally, Figure 3.14.b demonstrates, in the phase plot, that the phase data collected is well-defined in the range between -0.05 to 0.05 meters in the x -axis. Outside this range, the noise affected the measurements.

3.5 Summary

In this chapter, all the improvements made to the mmWave scanner system were reviewed. It began by explaining the advantages of designing the graphic interface in MATLAB. These include the high ease of designing the interface and the ability of object-oriented programming to reduce the complexity of the program

when controlling the hardware. In other words, it is possible to control all nine motors with a single function. This chapter also showcases the designed graphic interface and its different windows, which include instrument control, near-field, far-field, and material characterization.

In the near-field program, the improvements included the addition of a continuous raster scan algorithm that reduces the duration of the tests by 2.6 times. Additionally, post-processing algorithms such as the near-field to far-field transformation and hologram back projection were implemented. The design of a structure for the far-field setup was also detailed, which allows the carrying of the frequency extender and a sliding feature for adjusting the distance between the rotation axis of the rotary table and the center of the antenna under testing.

Finally, the results of both near-field and far-field tests are illustrated. In the near-field test, comparisons between different raster scans (continuous and park-and-probe) are shown, along with the impact of the timer's period error on the measurements. The results demonstrate that the continuous scanning method has an acceptable level of reliability while reducing the test duration to less than half compared to the park-and-probe method. However, the park-and-probe scan shows the highest level of reliability in the measurements.

Chapter 4

W-band Antenna-in-Package Calibration

4.1 Antenna-in-Package

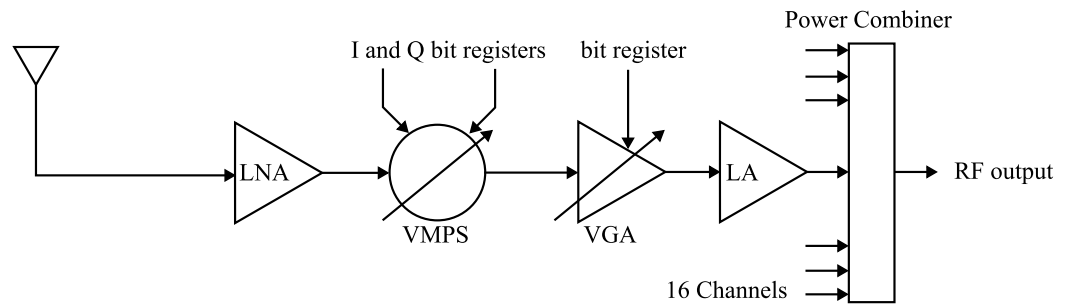
Antenna-in-Package (AiP) is a technology that has been utilized for many years to develop antennas for frequencies above 70 GHz. Recently, this technology has witnessed widespread implementation, particularly in the automotive radar applications industry, where frequencies ranging from 24 GHz to 77 GHz are extensively used.

4.1.1 Metawave's Antenna-in-Package

The Metawave Corp. developed an AiP for the automotive industry, the first 77 GHz beam-forming fully-integrated front-end AiP module, with the operating frequency range of the antennas from 76 GHz to 81 GHz. The device completely integrates a SPEKTRATM AiP module with a Metawave MARCONITM [19]. The SPEKTRA AiP, or AiP for short, is an analog beamforming antenna with 16-channels, in which each channel has a phase shifter and a variable amplifier that allows control over the output power and phase of the antenna. The 16-channels are connected to 16 phased array antennas arranged in a 4x4 element array. Due to its functional design and structure, there are two types of these AiPs, for reception

Block diagram of the SPECTRA AiP Channels

RX Channel



TX Channel

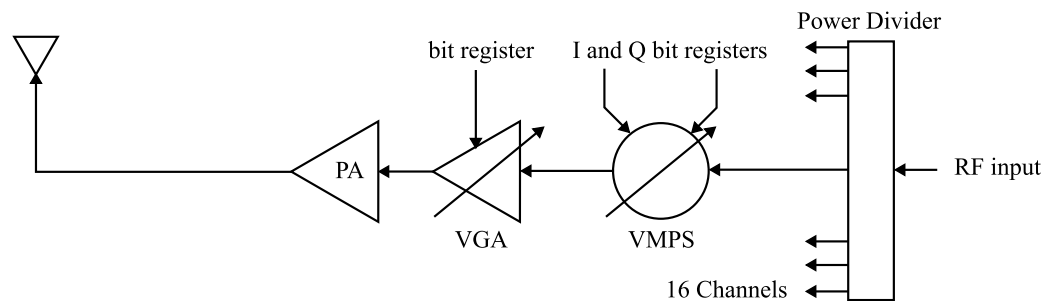


Figure 4.1: Simplified functional block diagram for both TX and RX channels in MARCONI beamforming chips. LNA represents the low noise amplifier, VMPS stands for vector modulated phase shifter, VGA denotes variable gain amplifier, LA represents linear amplifier, and PA stands for power amplifier.

(RX) and for transmission (TX). The Marconi beamforming chip is not capable of performing both TX and RX operations; because of this, there are two different models of AiPs developed by Metawave: the MWAiP03T0 for TX and MWAiP03R0 for RX. Figure 4.1 illustrates a simplified functional block diagram for both types of channels. In the case of the TX channel, the LNA and LA blocks amplify all the low-powered signals received by the antenna to increase the signal-to-noise ratio and increase the possibility of detecting a target. The TX side is simpler; it uses a power amplifier to increase the power out of the antenna. The variable gain amplifier (VGA) has a gain control range of 20 dB and a resolution of 0.5 dB. The

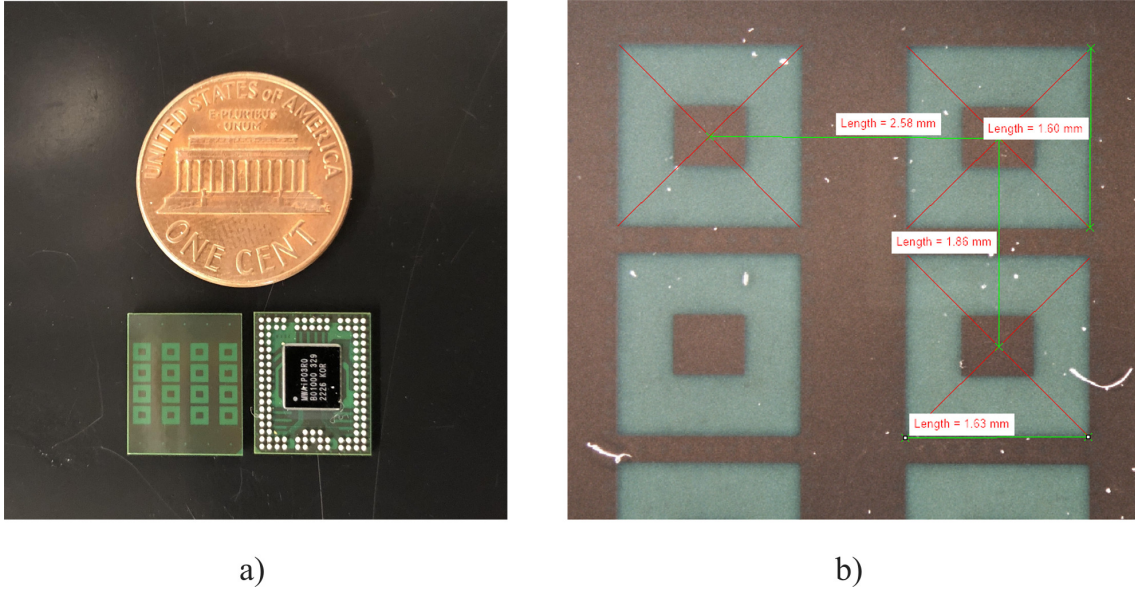


Figure 4.2: a) A photo of the AiP chip antenna size compared with a one-cent coin. b) A photo taken from an electronic microscope showing the precise dimensions of the antenna elements and the spacing between elements.

vector modulated phase shifter (VMPS) has two-bit registers which allow a phase shift range of 360° with a resolution of 2.8° . Table 4.1 shows a brief summary of the AiP electrical characteristics.

The size of the package is $10.2 \text{ mm} \times 12.4 \text{ mm}$ with 16 patch antennas distributed in 4 rows and 4 columns, as illustrated in Figure 4.2.a. Figure 4.2.b shows that the rows and columns are not evenly separated. The separation in one dimension is 2.58 mm and in the other is 1.86 mm.

4.2 System Description

The proposed system represents a hybrid configuration capable of both characterizing and calibrating antenna arrays within both the far-field and near-field regions. The far-field domain primarily serves the purpose of over-the-air (OTA)

Table 4.1: Summary of the electrical characteristics of the AiP. Provided by Metawave Corporation.

	Transmitter IC (TX)	Receiver IC (RX)
RF port return loss (dB)	12	12
Maximum single channel gain (dBi)	28	18
Gain control range (dB)	0-20	0-20
Gain control resolution (dB)	0.5	0.5
Phase control range (deg)	0-360	0-360
Phase control resolution (deg)	2.8	2.8
Noise Figure (dB)		9.5
RF port termination (Ω)	50	50

calibration and the validation of antenna patterns. Conversely, the near-field mode is capable of park-and-probe and continuous scanning measurements. This system was adapted and implemented in the 9-axis system described in Chapter 3. Building upon this foundation, this project introduces three additional operational modes integrated into the system, all while utilizing the same hardware, RF instruments, and other essential components for setup. Figure 4.3 shows an illustration of the hybrid system developed for the AiP antenna calibration, near-field measurement and an special AUT in-situ far-field measurement.

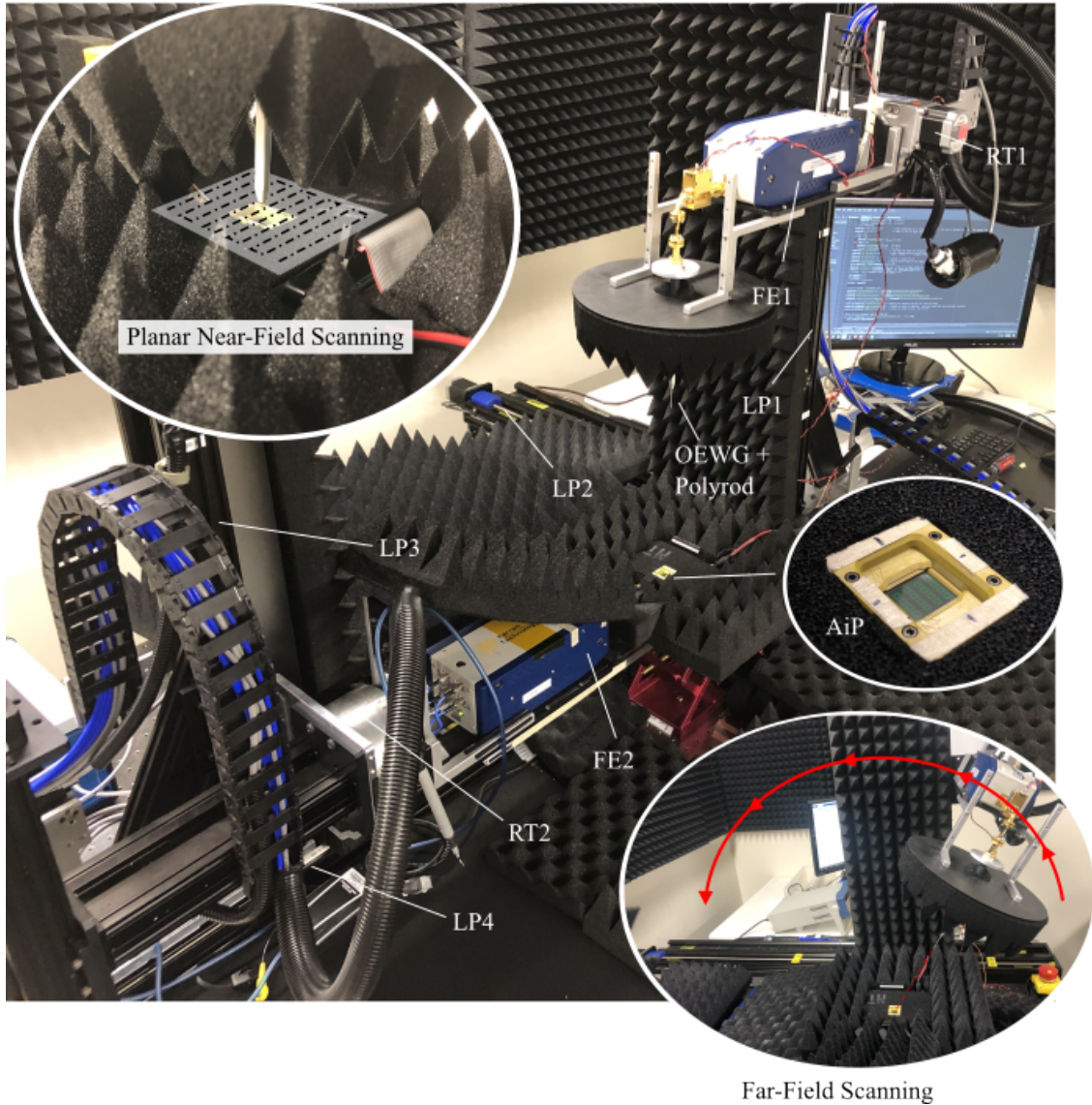


Figure 4.3: Image of the hybrid test system portraying the near-field calibration process and featuring the AiP antenna array and evaluation board. The system integrates both near-field and far-field scanning operation modes

4.2.1 Requirements

One critical requirement for this system involves the orientation of the AiP socket; it is essential to have a horizontal placement facing upward. For Metawave, this configuration is necessary due to the significant number of AiP antenna arrays subjected to the calibration and measurement processes. Such an orientation

facilitates the chip replacement process, enhancing the efficiency and speed of all AiP antennas. To ensure precise calibration and establish the desired AUT-probe distance within the far-field range, the probe antenna must possess both high gain and a narrow beam. In contrast, during near-field planar scanning measurements, the primary criterion for the probe antenna is achieving low gain and a wide beam, as highlighted in [2].

4.2.2 Near-Field Probe and Polyrod Antenna

Originally, a standard gain horn (SGH) antenna with a gain of 23 dB served as the probe for the far-field mode. The separation distance between the AUT and the probe in the far-field mode was 66 cm due to the maximum dimension of the SGH, which was 3.5 cm. Using Equation 2.4, the result was 63 cm. As previously mentioned, the FF probe must have high gain and a narrow beam. A measurement test and radiation pattern calculation were performed in Chapter 3, showing that the half-power (3dB) beamwidth is approximately 14° . However, to carry out near-field measurements, the probe antenna had to be replaced, and the distance between the antennas reduced. To enable this system to perform both far-field and near-field measurements, a probe antenna capable of easily transitioning between high gain and low gain is necessary. A polyrod, or dielectric rod, is a structure made of dielectric material without any metallic boundaries. This structure allows the radiation of the energy that travels through it. With the proper design, this radiating structure can function like an endfire antenna [49]. In this case, it can focus the radiating energy of the OEWG antenna. This requirement was addressed by implementing a solution

involving a polyrod antenna attached to an open-ended waveguide (OEWG). The polyrod functions as a component to enhance the gain and narrow the beam of the probe antenna. For this configuration, the polyrod was designed to increase the gain of a WR10 OEWG from approximately 6 dBi to 17.9 dBi. However, after fabrication, the measured gain of the polyrod antenna with the OEWG is 16 dBi. To achieve equivalent power performance as the SGH antenna, the distance was reduced from 66 cm to 26.6 cm, and this is possible due to the polyrod antenna having a short FF distance. Common OEWG antennas have a very broad beamwidth. Figure 4.4.a shows the measured radiation patterns in H- and E-planes, where the

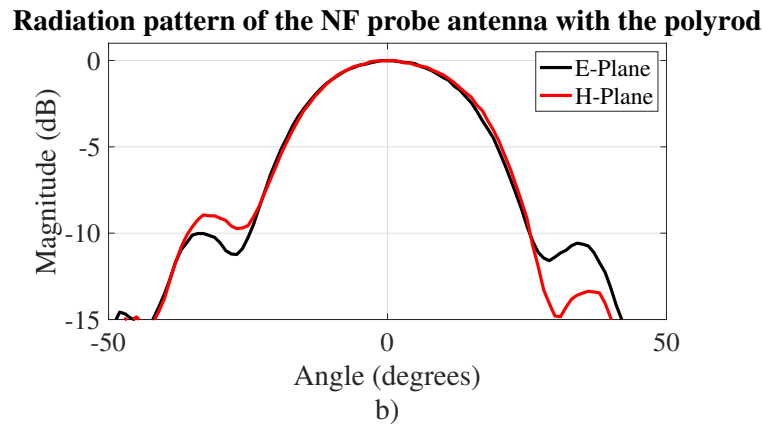
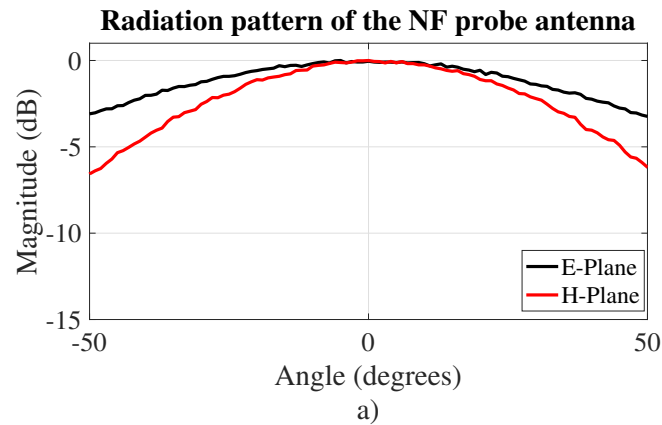


Figure 4.4: a) and b) Measured radiation patterns of the NF OEWG probe and with the polyrod respectively.

half-power beamwidth is 98° and 66° respectively, and Figure 4.4.b is the radiation pattern of the polyrod, where the half-power beamwidth for both planes is 30° . Both patterns were measured using the setup described in Section 5.3.2, and the method to calculate the gain is with the three-probe antenna method, the same method used to calculate the gain of the AiP.

4.3 Calibration Setup

The system operates in three distinct modes: a) AiP element characterization and array calibration mode, b) horizontal NF planar scanning, and c) single-plane FF scanning mode. A vector network analyzer (VNA) equipped with frequency extenders (FE) is employed, enabling measurements within a range spanning from 75 GHz to 110 GHz. Further specifications for the VNA and scanner are provided in Chapter 2. Since there are two types of AiP antennas, for transmission (TX) and reception (RX), two setups were designed in a way that they can easily transition from one setup to another. Within this project, the variable gain (VGA) was set at a 30 dB attenuation to prevent saturation during the calibration process. On the probe side, a low-noise amplifier (LNA) with a gain of 20 dB compensates for losses occurring in the free space between the probe antenna and the antenna under test (AUT). The configuration of the setup is depicted in Figure 4.5. To change between the two setups, the direction of the LNA is switched since it is an active component that only amplifies the signal in one direction. In theory, the most efficient way to design the two setups is by adding an attenuator in the transmitting FE and

the LNA in the receiving FE. This means that for the RX setup in Figure 4.5, the LNA and the attenuator should be exchanged in positions. However, such a configuration would bring some inconveniences. Firstly, the exchanges themselves entail a rearrangement of the components. Additionally, other waveguides would need to be included on the transmitting side of the setup due to the short range of the LNA and the large height of the component, which would become an obstacle

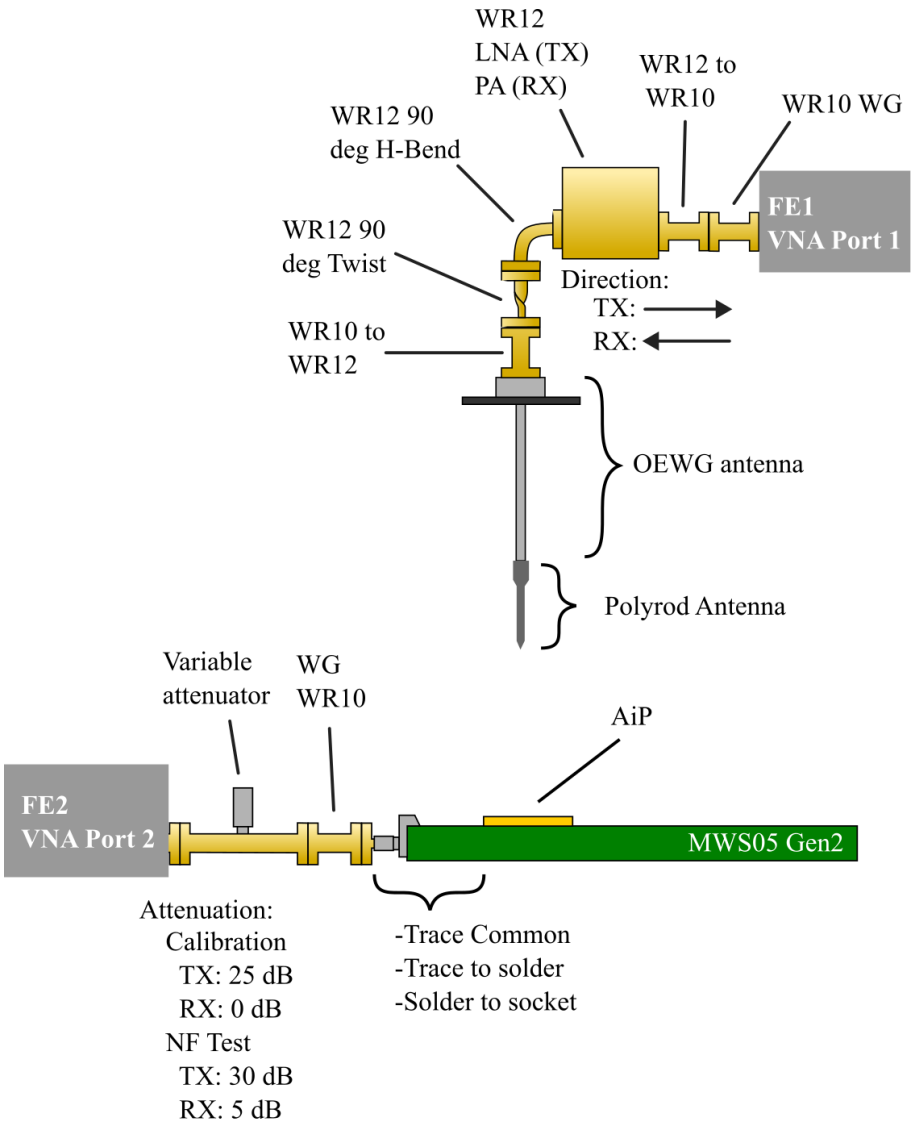


Figure 4.5: Illustration of the calibration setup for TX and RX AiPs.

to the absorbers and their support structure during the NF test. As explained in Section 2.1.1, the probe antenna would have to be at a distance of 3λ to the AUT, which is approximately 12 mm. Another minor inconvenience is the lack of and addition of other WR12 to WR10 and vice versa components to the system due to the LNA port type being WR12 and only using WR10 components at the FE2 side.

A crucial aspect of the calibration process involves the accurate measurement of the antenna's gain. To achieve this, the three-antenna absolute gain measurement method was employed. This process commences with a full two-port calibration of the VNA. Subsequently, the setup depicted in Figure 4.5 is established, with the exception being the replacement of the evaluation board and AiP array antenna with a WR12 SGH antenna. This particular antenna is characterized by its narrow beam and high gain of 23 dBi. Within this setup, the complex S-parameter data of the VNA alongside the SGH antenna is stored as a reference. This data will later undergo mathematical calculation with the VNA data of the AUT, yielding the absolute gain of the AUT. The comprehensive calculation consists of two equations, resulting in the s-parameters of a measurement. Division of Equation 4.2 by

Equation 4.1 yields Equation 4.3, and the final outcome, Equation 4.4, represents the absolute gain of the AUT.

$$P_{ref} = \frac{G_{SGH} \cdot G_{LNA} \cdot P_1}{L_{others} \cdot G_{att} \cdot L_{free}} \quad (4.1)$$

$$P_2 = \frac{G_{AUT} \cdot G_{LNA} \cdot P_1}{L_{others} \cdot G_{att} \cdot L_{free}} \quad (4.2)$$

$$\frac{P_2}{P_{ref}} = \frac{G_{AUT}}{G_{SGH}} \quad (4.3)$$

$$G_{AUT} = \frac{G_{SGH} \cdot P_2}{P_{ref}} \quad (4.4)$$

Where P_{ref} is the power measured in port 2 using the SGH as AUT, G_{SGH} is the SGH gain (this value is given in its datasheet), G_{LNA} is the gain of the LNA, P_1 is the power delivered by port 1. G_{att} is the attenuation given by the variable attenuator, L_{free} is the losses of the free-space, and L_{others} are all the losses of the other components like the waveguides, transitions, etc.

4.3.1 Setup Components and Power Budget

In the previous section, the setups designed for the two AiP antenna types were described, and one of the factors taken into consideration for the design was the power input and output in each component in order to avoid issues like saturation of power in any active device like the LNA, PA or the AUT devices. Therefore, to measure the power level (dBm) in every section of the setup, a device known as a power meter was used. The Keysight U8489A is an average power sensor designed

to measure the power level in frequencies up to 120 GHz. The power range this device is capable of measuring is between -35 to 20 dBm [50].

Table 4.2 and Table 4.3 describe the power budget for both the TX and RX calibration setups respectively. In the RX setup, the component which is more susceptible to saturation is the PA due to its direct connection to the FE. Using the power meter, it was verified that with the default RF power of the FE, the output power was 0.53 dBm and the output power of the PA was 11.2 dBm, while the actual gain of the PA is 20 dB. This indicates that the PA is saturated with power. By adjusting the output power level of the FE to -12.7 dBm, the output power of the LNA was reduced to 7.7 dBm, resulting in a 20 dB gain in the PA.

In the TX setup, the component that is susceptible to saturation due to high power is the AiP antenna itself. However, the saturation in the AiP is very special

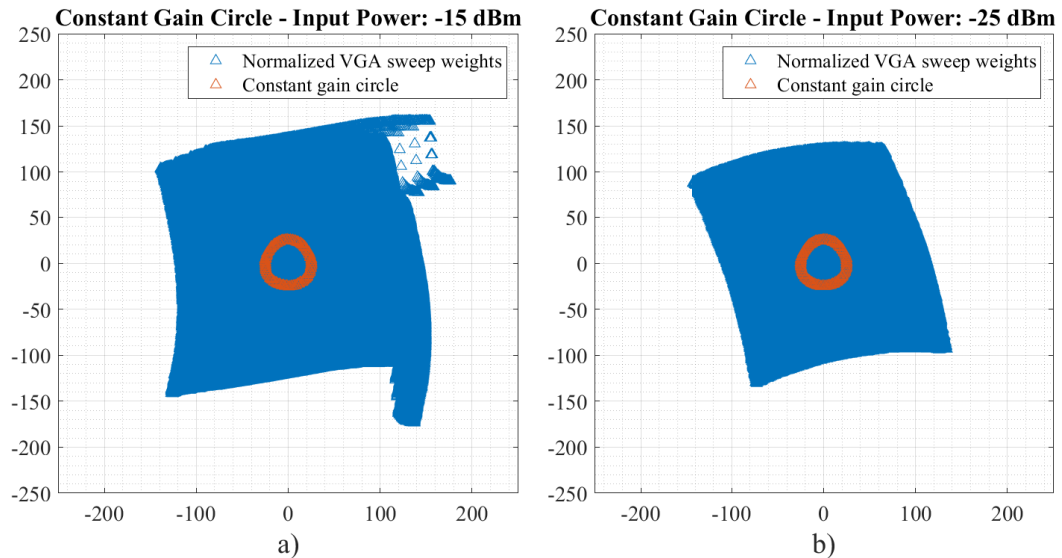


Figure 4.6: AiP variable values sweep measurement results a) with an input power of -15 dBm and b) with an input power of -25 dBm.

Table 4.2: Link budget of the TX calibration setup

RF Item	Gain (dB)	Output Power (dBm)
VNA Port 2 out WR10		-0.62
Variable Attenuator WR10	-25	-25.62
Waveguide WR10	-1.1	-26.72
Trace Common	-3	-29.72
Transition trace2solder	-0.37	-30.09
Transition solder2socket	-0.53	-30.62
MWS05 Gen2	28	-2.62
Patch Gain	4	-1.38
Free Space losses	-60	-58.62
NF Probe+Polyrod Gain	16	-42.62
Transition WR10 - WR12	-0.23	-42.85
Waveguide 90 deg Twist	-1	-43.85
Waveguide H-Bend 90 deg	-1.34	-45.19
LNA 20dB Gain WR12	20	-25.19
Transition WR12 - WR10	-0.23	-25.42

since it mostly affects non-linear states of the VMPS. Figure 4.6 shows the results of the measurement of a sweep of all the states of the VMPS and VGA. In the ideal situation of the two components, Figure 4.6.b should show a linear rhombus. However, due to the non-ideal behavior of the VMPS and VGA, the results show a non-linear behavior in certain states which are not used due to their non-linear

Table 4.3: Link budget of the RX calibration setup

RF Item	Gain (dB)	Output Power (dBm)
VNA Port 1 out WR10		-12.07
Transition WR12 - WR10	-0.23	-12.3
PA 20 dB Gain WR12	20	7.7
Waveguide H-bend 90 deg	-1.34	6.36
WG 90 deg Twist	-1	5.35
Transition WR10 - WR12	-0.23	5.13
NF Probe+Polyrod Gain	16	21.13
Free Space Losses	-60	-38.87
Patch Gain	4	-34.87
MWS05 Gen2	19	-15.87
Transition solder2socket	-0.53	-16.4
Transition trace2solder	-0.37	-16.77
Trace Common	-3	-19.77
WG WR10	-1.1	-20.87

behavior. Fortunately, these states are the ones more susceptible to saturation. The states used in the calibration are the ones inside the orange circle in Figure 4.6, where the states of both VMPS and VGA have a linear behavior. However, for this calibration process, any saturation is undesired, so the variable attenuator was set to -25 dB gain.

4.4 Summary

In this chapter, the situation of how Metawave Corp. required a calibration setup for the Antenna-in-Package, a device developed by them for the automotive industry, was discussed. Utilizing the electric properties of the AiP arrays and the two types of antennas (TX and RX), two different setups were designed and implemented into the 9-axis mmWave scanner system. The setups were designed to perform three different measurement tests: Antenna calibration, near-field scan measurement, and far-field scan measurement (for validation purposes only). It was also explained how the probe antenna's versatility allows it to change from a broad-beam, low gain antenna to a narrow-beam, high gain antenna using a dielectric structure called a polyrod, this structure is capable of increasing the gain of the OEWG from 6 dB to 16 dB, narrowing the beam from approximately 90° to 30° . To measure the gain of the AiP, a standard gain horn antenna was used with a method called three-antenna absolute gain measurement. Finally, to avoid undesired saturation in the active components like amplifiers, a power budget of both calibration setups was done, describing what would happen if the LNA or the AiP were saturated with high power.

Chapter 5

AiP Calibration, Measurement Tests and Results

5.1 AiP Calibration Process

An advanced calibration algorithm was employed to compute optimal weights and settings for the VGA and phase shifter, aligning them with the coefficients required for uniform power distribution and precise beam positioning. A general description of the calibration process is illustrated in Figure 5.1. The process starts by defining the initial parameters of the calibration process, such as the ID of the chip antenna, the number of antennas, choosing between TX and RX, the directory

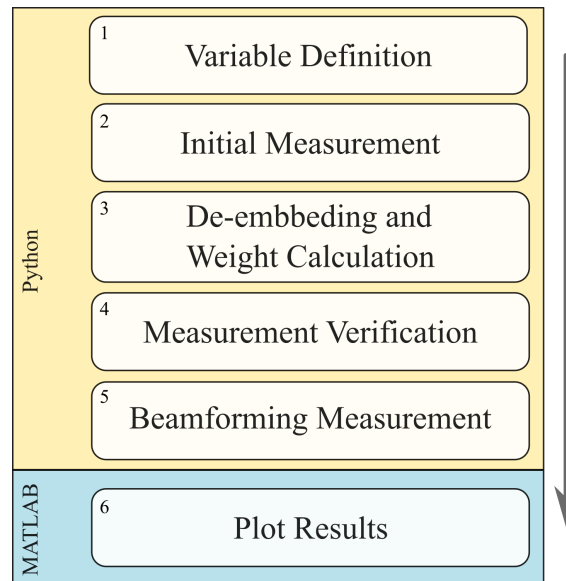


Figure 5.1: Summarized block diagram of the calibration algorithm.

where the results would be stored, defining sweep measurement values, VNA configurations, etc. In block 2, the main focus is on the measurement of the AiP in all the configured states. Block 3 performs the gain calculation with Equation 4.4, the calculation of the weights for each state of the VMPS and VGA, and the storage of the calibration table. In block 4, once these states are calculated and stored in both a table and a file, a secondary measurement is conducted to validate the calibration's efficacy. Finally, there is a measurement of the beamforming, which involves enabling each element one by one to verify the gain accumulation of the chip. Up to this point, the algorithm was developed in Python due to the driver compatibility of the AiP socket controller (MWSO5 in Figure 4.5). The final block, which involves plotting the results, was developed in MATLAB due to its better plotting resources and the capability to save the plots with ease.

5.1.1 Calibration Results

The calibration results are collected in block 4 of Figure 5.1. After the measurement, the s-parameters of all the channels are compared in amplitude and phase at three different frequencies: 77 GHz, 78 GHz, and 80 GHz. Illustrated in Figures 5.2, 5.3, 5.4, and 5.5 are the S_{12} parameters, both amplitude and phase, for each individual element or channel that was measured. In all the figures, panels a), c), and e) represent the absolute values, either amplitude or phase depending on the figure, at 77 GHz, 78 GHz, and 80 GHz, respectively. The remaining panels show the s-parameters normalized with respect to channel 8. This normalization allows us to discern the disparities between elements when all are configured for uniform

power distribution. The ideal result is that all the elements have an amplitude of 0 dB and a phase of 0° in the normalized plots. Notably, in Figure 5.2.d at 78 GHz, the amplitude discrepancies are at their lowest compared to other frequencies.

The calibration algorithm's precision is evidenced by its utilization of straightforward statistical formulas to calculate the most representative values (mean) of amplitude and phase, as well as the elements' excitation errors (standard deviation). The algorithm has been configured to successfully calibrate the AiP antenna at frequencies of 77, 78, and 80 GHz. Comprehensive results are outlined in Table

Table 5.1: Statistical parameters of the calibration results of the AiP chip antenna.

Plot	Param.	TX cal. results	RX cal. results
Freq. 77 GHz	Mean	0.0404 dB	-0.0962 dB
Amp vs Freq	STD	0.1434 dB	0.0805 dB
Freq. 77 GHz	Mean	-0.7004°	-0.4374°
Phs vs Freq	STD	1.4628°	1.3720°
Freq. 78 GHz	Mean	-0.0044 dB	-0.0208 dB
Amp vs Freq	STD	0.0815 dB	-0.0806 dB
Freq. 78 GHz	Mean	-2.1295°	-1.1554°
Phs vs Freq	STD	1.4948°	0.7375°
Freq. 80 GHz	Mean	-0.0828 dB	0.1429 dB
Amp vs Freq	STD	0.1088 dB	0.0951 dB
Freq. 80 GHz	Mean	2.4061°	-0.5243°
Phs vs Freq	STD	1.4124°	0.7312°

TX Calibration Results

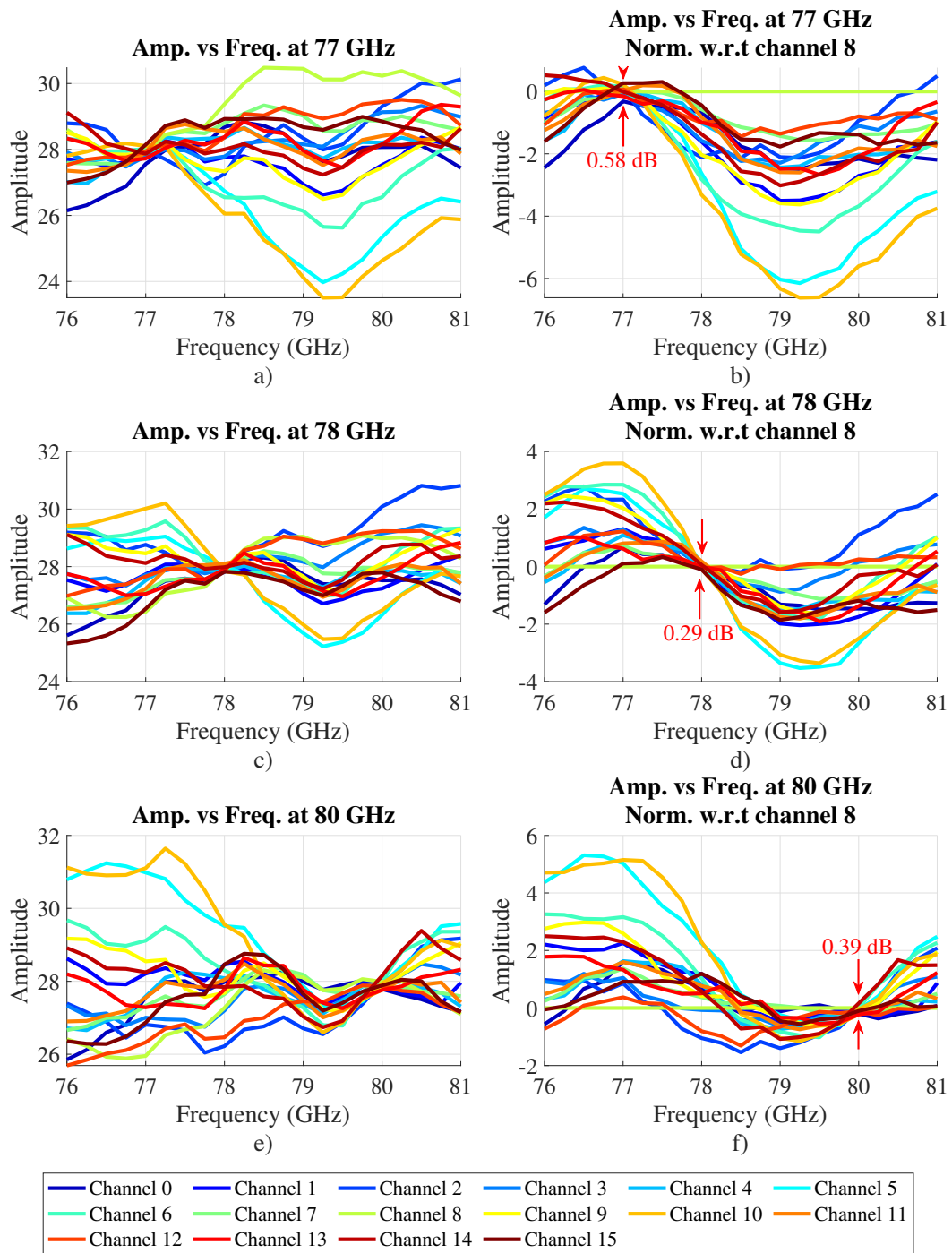


Figure 5.2: S-parameters (amplitude) of each individual channel of the TX AiP. Panels a) and b) display the calibration results with the calibration values at 77 GHz, panels c) and d) depict the results at 78 GHz, and panels e) and f) show the results at 80 GHz. Additionally, panels b), c), and f) present the s-parameters normalized with respect to (w.r.t) channel 8.

TX Calibration Results

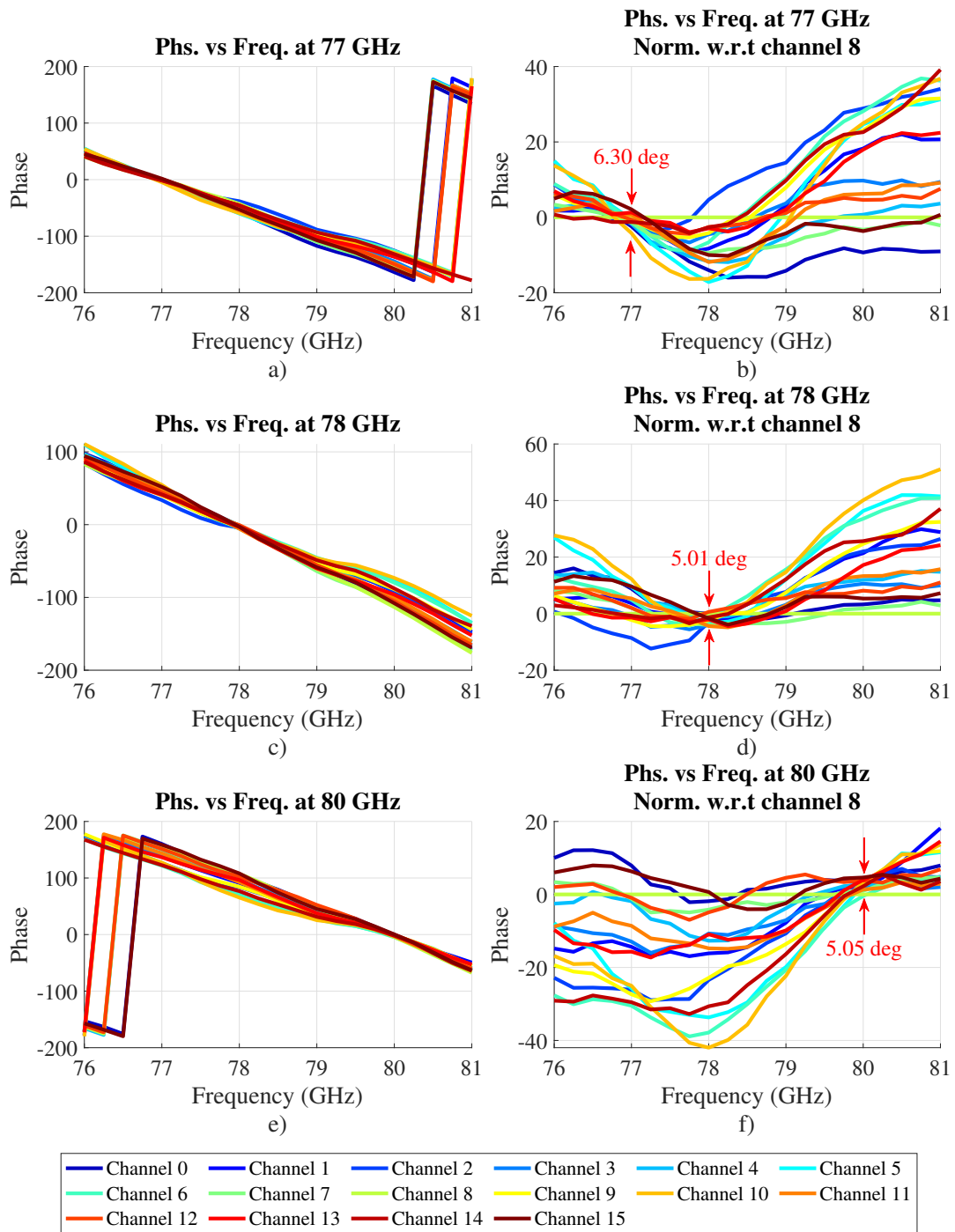


Figure 5.3: S-parameters (phase) of each individual channel of the TX AiP. Panels a) and b) display the calibration results with the calibration values at 77 GHz, panels c) and d) depict the results at 78 GHz, and panels e) and f) show the results at 80 GHz. Additionally, panels b), c), and f) present the s-parameters normalized with respect to (w.r.t) channel 8.

RX Calibration Results

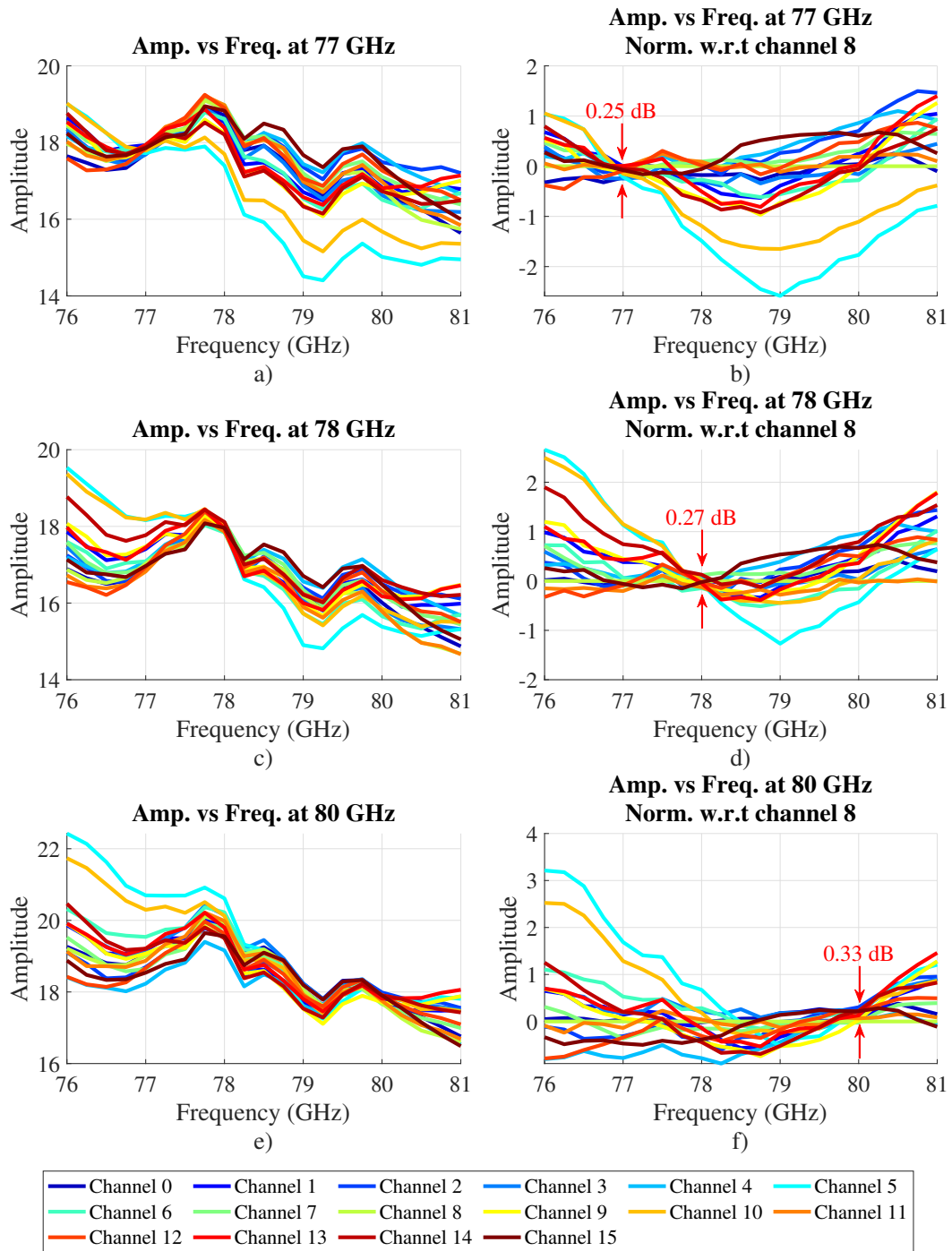


Figure 5.4: S-parameters (amplitude) of each individual channel of the RX AiP. Panels a) and b) display the calibration results with the calibration values at 77 GHz, panels c) and d) depict the results at 78 GHz, and panels e) and f) show the results at 80 GHz. Additionally, panels b), c), and f) present the s-parameters normalized with respect to (w.r.t) channel 8.

RX Calibration Results

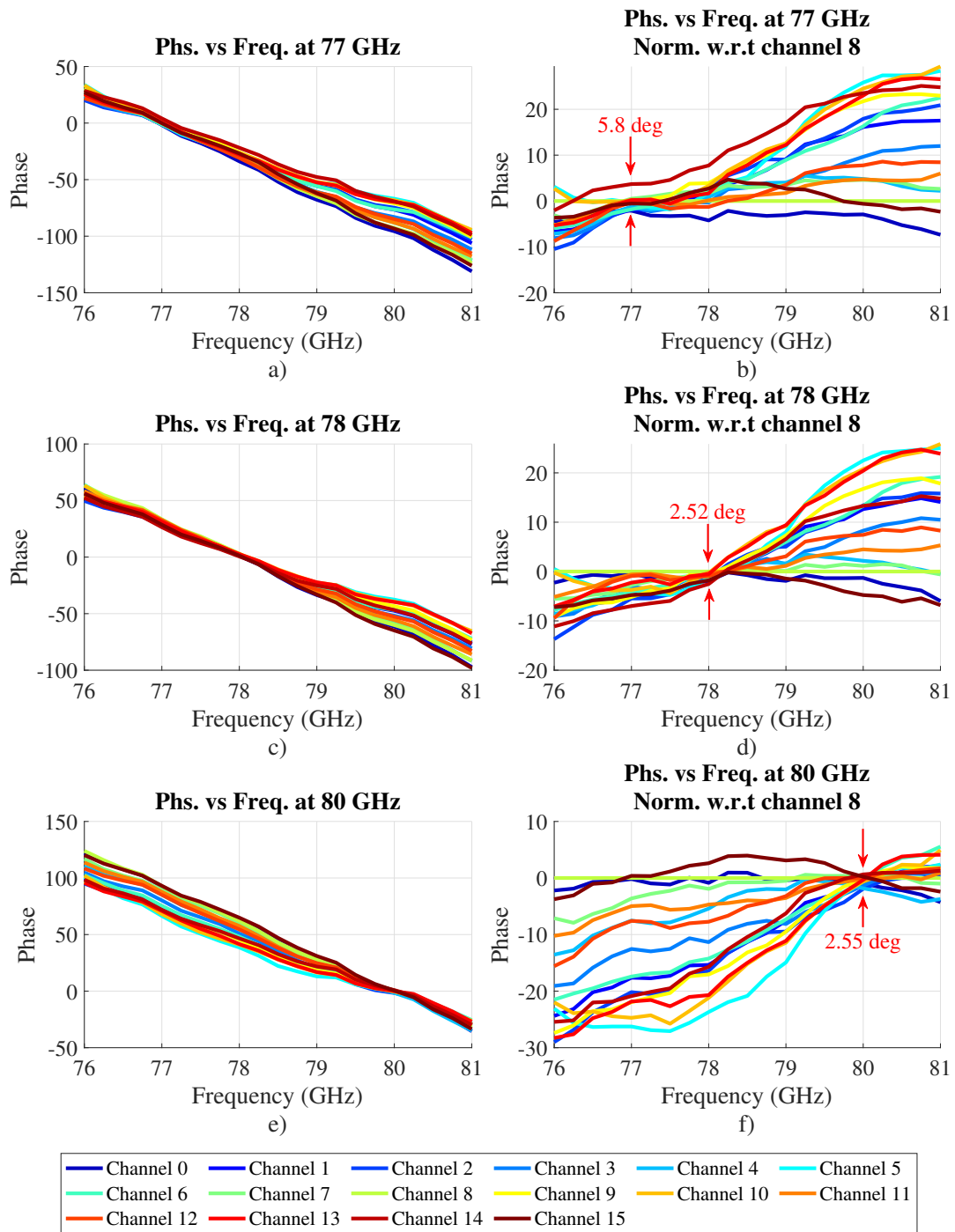


Figure 5.5: S-parameters (phase) of each individual channel of the RX AiP. Panels a) and b) display the calibration results with the calibration values at 77 GHz, panels c) and d) depict the results at 78 GHz, and panels e) and f) show the results at 80 GHz. Additionally, panels b), c), and f) present the s-parameters normalized with respect to (w.r.t) channel 8.

5.1. The standard deviation shows the dispersion of the values of the channels with respect to the mean. The lower the value, the better. As demonstrated in Table 5.1, in general, the calibration of the AiP in RX is better at every frequency than in TX. Regarding the phase measurements, Figure 5.3 shows a maximum range average of 5° , and Figure 5.5, except for the 77 GHz case, shows an average of 2.5° . In the case of Figure 5.5.b, 15 channels are noticeably close to the mean, which represents good calibration, while one of the channels is separated, indicating that recalibration is most likely needed.

5.2 AiP Control Software

In previous sections, the calibration algorithm was briefly described, and the calibration measurement plot with the results was shown. However, the principal goal of the calibration is to create a table where each single element of the AiP array antenna has assigned a specific I, Q, and V state, where I and Q represent the states of the VMPS and V represents the state of the VGA. A software capable of controlling the AiP chips was developed. This software is capable of selecting and reading the calibration table file and showing the IQV states depending on the values of the table, and the phase or gain is selected by the user. It is also capable of enabling and disabling elements of the array, showing in real time parameters of the board like the chip temperature, the current that flows through the chip, etc. Finally, the software is capable of performing beam synthesis. This function calculates the values of the phases and magnitudes of each element to obtain a

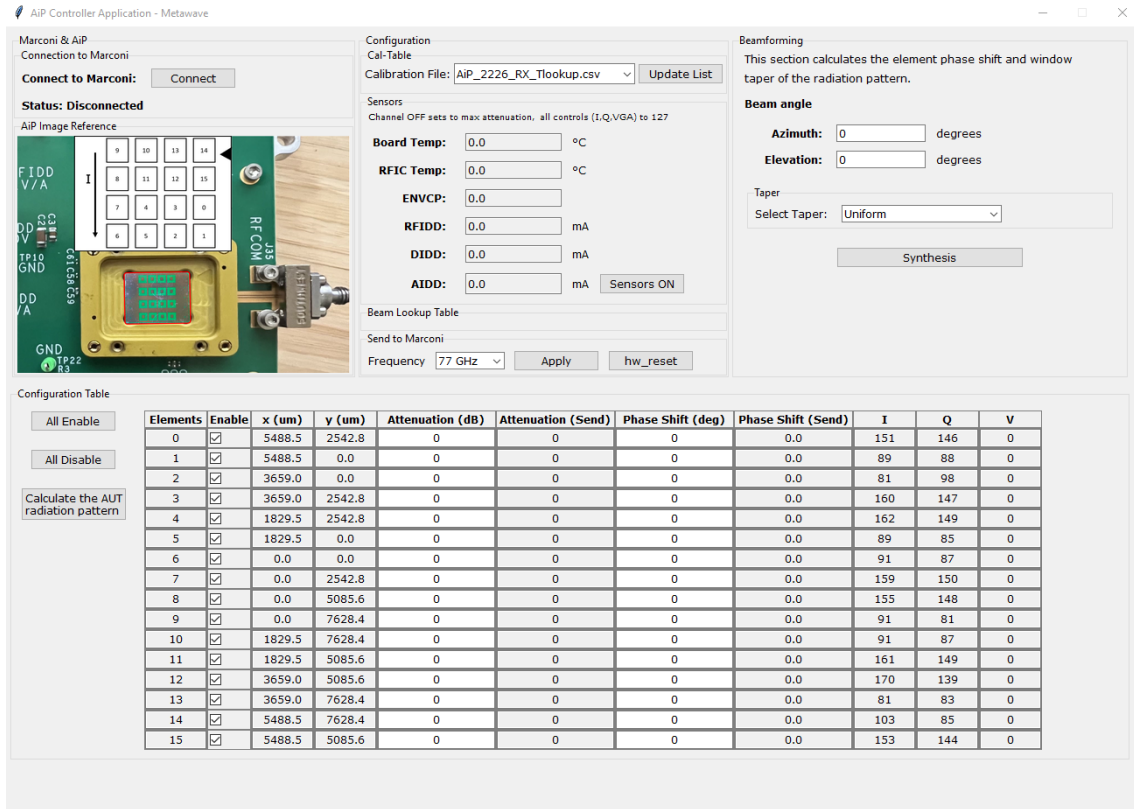


Figure 5.6: Photo of the AiP controller software developed specifically for automatic analog beamforming process.

desired radiation pattern, as well as automatically writing the results on the inputs and obtaining the IQV values. Figure 5.6 shows a picture of the main windows of the AiP controller software, which displays all the previously mentioned features.

5.3 Patterns Measurement Tests

5.3.1 Horizontal Near-Field Scanning

The mmWave scanner system offers 9 degrees of freedom. In Section 2.3.1, it is described that for the NF scanning operation, it is typically conducted in a vertical plane using linear positioners (LP1, LP2) and a rotary table (RT1). However, for the

AiP NF measurements, adjustments have been made due to the setup structure. The measurements must be performed in a horizontal plane. As depicted in Figure 4.3 (NF-P scanning), the linear positioners employed in the data collection process for the NF scan are LP2 and LP4. LP2 controls probe movement along one dimension, while motor LP4 maneuvers the AUT in a perpendicular axis. These combined movements enable the probe antenna to traverse over the AUT in a raster path in a horizontal plane. LP1 motor is used to reduce the distance from 26.6 cm to 12 mm (equivalent to 3λ at 77-78 GHz), where the polyrod antenna is detached from the OEWG antenna in order to have a broad-beam and low-gain antenna, as is explained in Section 2.1.1. Due to the proximity to the AUT, in the case of the TX setup, the variable attenuator connected to FE2 is set to 35 dB attenuation. This adjustment is necessitated by the diminished free space losses and the LNA's susceptibility to saturation. Figure 5.7 illustrates the impact of the LNA saturation effects on the NF measurement and radiation pattern calculation of the AiP chips. Figure 5.7.a and 5.7.c show the magnitude of the NF measurement, and in Figure 5.7.c, surrounding the peak point, where the transmission of the energy from the AiP to the probe is direct, there is a circular region of data where the magnitude is close to the maximum. This means that the actual maximum power level is saturated by the LNA, deforming the NF measurement and distorting the main beam in Figure 5.7.e. On the other hand, in the RX setup, there is no need for a change in the variable attenuator. Additionally, this configuration supports the continuous algorithm improvements described in Section 3.3.3 with great results.

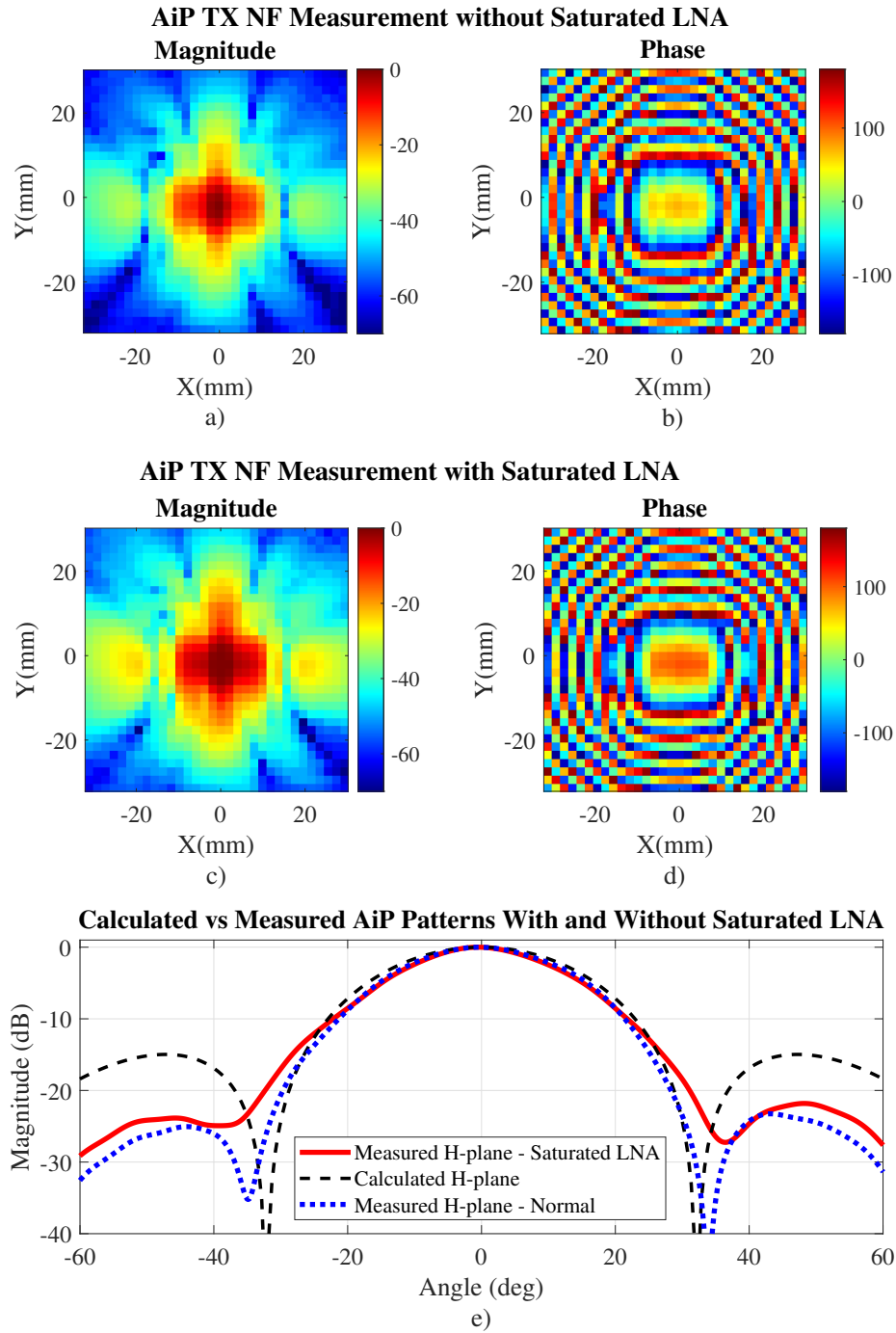


Figure 5.7: a) and b) Magnitude and phase NF measurements by increasing the attenuation of the variable attenuator on FE2 to 35 dB respectively. c) and d) Magnitude and phase NF measurements with saturation in the LNA. e) Radiation patterns comparison between the theoretical, measured with saturation in the LNA and measured normally without saturation.

5.3.2 AUT in-situ Far-field Scanning

A singular plane FF scanning technique is employed to precisely measure the antenna array pattern of the 4x4 AiP antenna array. This set of measurements plays a crucial role in validating both the OTA and NF calibration procedures. To facilitate this, linear positioners (LP1 and LP2) along with a rotary table (RT1) are utilized. They collectively execute a circular trajectory around the Antenna Under Test (AUT), maintaining a consistent radius throughout. Notably, the radius of this scan path is intentionally set to surpass the far-field (FF) distance of the AUT. In the context of the AiP antenna array, the FF range exceeds 6 cm. During this process, the polyrod and a variable attenuator set to 30 dB attenuation are incorporated. To accurately determine motor positions, the software necessitates inputs such as the distance between the AUT and the probing point, the distance

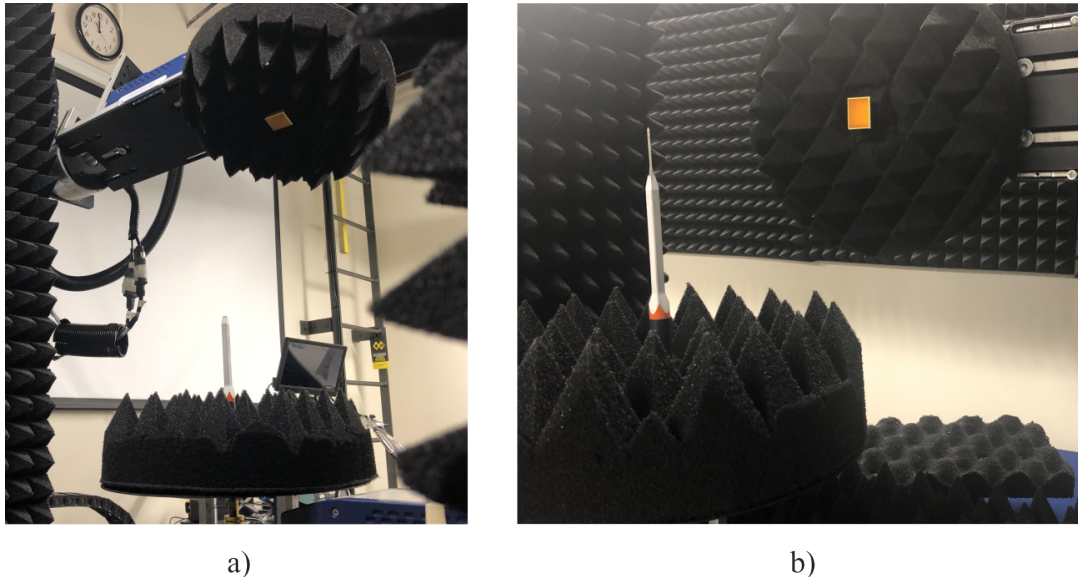


Figure 5.8: Far-field scan process for a) an OEWG probe antenna used for near-field tests, and b) the OEWG with a polyrod structure attached.

from the probing point to the center of RT1, the scanning angle, and the angle resolution. For visual reference, please consult Figure 4.3 (far-field scanning) to gain insight into the procedural execution of the scanning methodology. On another note, this FF setup was used to measure the radiation patterns of the NF OEWG with and without the polyrod structure. The results are shown in Figure 4.4, while Figure 5.8 presents photos of the OEWG and polyrod measurement process.

5.4 Radiation Pattern and Measurements

This section highlights the importance of all the previous parts of the calibration and measurement system. The goal is to measure a desired radiation pattern using the beamforming capabilities of the AiP chip. First, the NF measurement modes were tested in the new horizontal plane NF scanning, whose results are displayed in Figure 5.10. In Figure 5.9.a, the radiation patterns using both park-and-probe and continuous mode are shown, with the results indicating little discrepancy in the measured radiation pattern in both methods. Figure 5.9.b illustrates the difference and emphasizes the importance of the calibration on the AiP antenna. Each element of a non-calibrated AiP will emit an electromagnetic wave with an unknown or random phase, greatly distorting the radiation pattern of the array. The calibration process ensures that all individual elements exhibit consistent values. In Figure 5.9.b), the measured radiation pattern of the TX AiP is also overlapped against the calculated array factor. However, despite the comprehensive calibration effort, some deviations emerged in certain angles of the radiation pattern when comparing

the calculated and measured outcomes. In light of this, the reliability of the NF scanning results demanded verification. Panel d) of Figure 5.9 provides a visual comparison between the H-plane radiation patterns acquired through NF scanning and FF scanning methodologies described in Section 5.3.1 and 5.3.2, respectively. Lastly, in panel e), the beam steering capabilities of the AiP antenna are exhibited in the azimuthal direction, ranging from -20° to 20° in steps of 5° . This dynamic

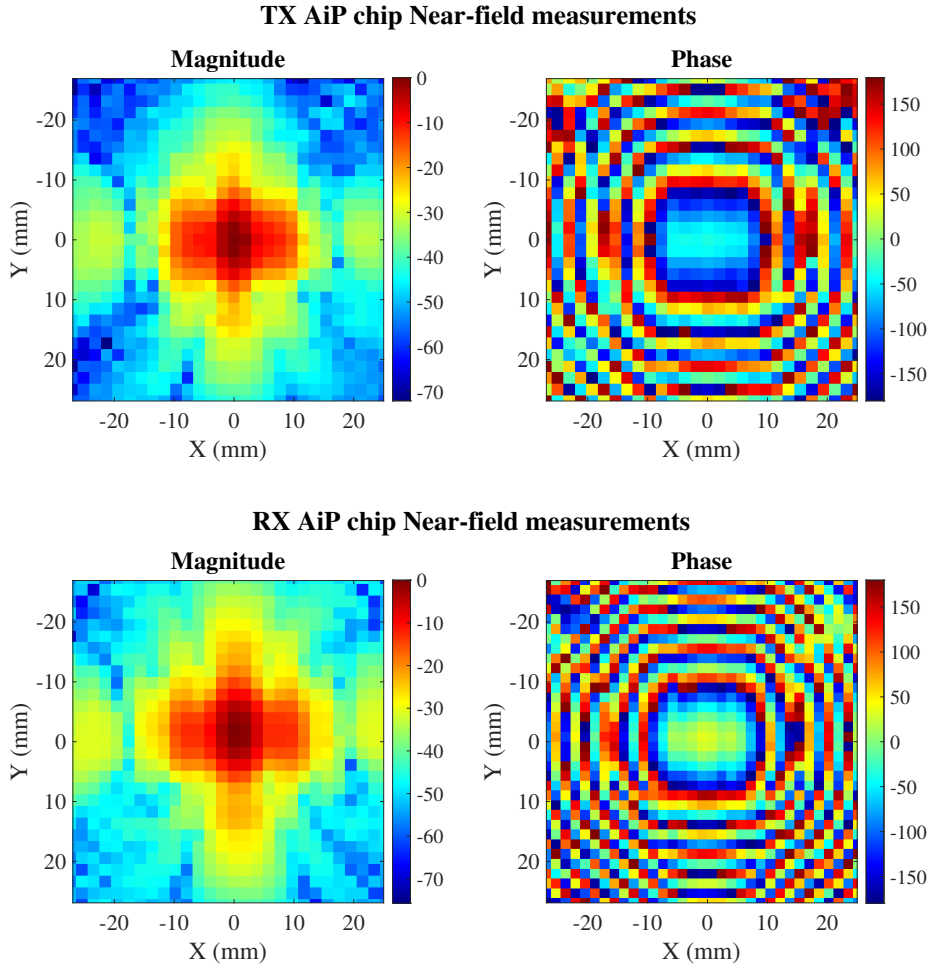


Figure 5.9: Near-field measurements for both TX and RX AiP chips in broadside uniform distribution.

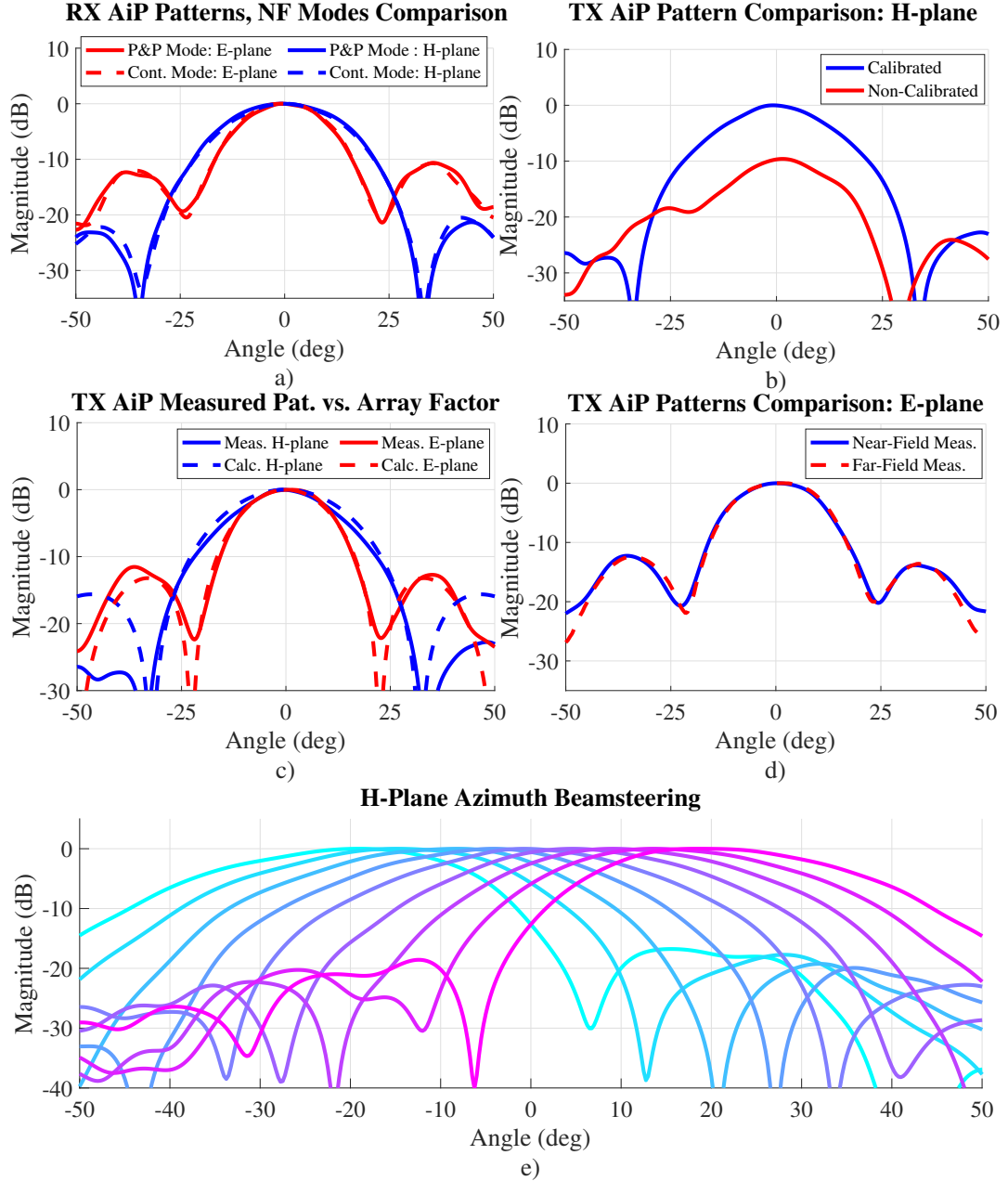


Figure 5.10: AiP antenna array radiation patterns at 78 GHz a) Comparison of the radiation patterns using both park-and-probe (P&P) and continuous NF scanning modes in both H- and E-planes. b) Comparison between the calibrated and not calibrated AiP antenna array in the H-plane, c) comparison of the calculated and measured radiation pattern of the AiP antenna array in broadside both E- and H-planes, d) comparison of the radiation pattern obtained by the NF scanning after a NF to FF transformation and the pattern obtained by the FF scanning, and e) A beam-steering of the TX AiP antenna array in azimuth from -20° to 20° every 5° .

illustration encapsulates the antenna's ability to steer its beam effectively within this range. Analyzing the results, it is concluded that the radiation pattern measured is correct, and the NF process performance is not related to the discrepancies visualized in Figure 5.9.c. It is believed that the cause of this discrepancy is the support structure that holds and presses the AiP to the socket, inducing edge effects in the measurements. Attempts were made to remove the holding structure for measurements, however, since the AiP is non-solder connected, without the structure, there was a problem of false contact and the measurement was impossible.

5.5 Summary

In this chapter, a general explanation of the calibration algorithm was provided, detailing how the calibration weights of a single AiP chip are stored in a file. The calibration results demonstrated great performance in the magnitude aspect of the measurements. In TX, the maximum difference observed was 0.58 dB, while in RX, it was 0.33 dB. Regarding the phase, it was observed that in TX, the maximum difference was 6.3° , and in RX, it was 5.8° . A software to control the AiP array antenna was developed, which initiates by calling a specific calibration file. This is crucial for determining the IQV states the software will configure in the AiP's VMPS and VGA, facilitating the beamforming configuration of the antenna.

On the other hand, in the mmWave system, two new operation modes were implemented to measure the near-field and far-field patterns of the AiP. The development of the new NF system was prompted by the requirements described in

the previous chapter, and results of two modes of raster scanning were provided, demonstrating that the continuous and park-and-probe scan have highly similar performance. However, when comparing the results to the antenna-calculated array factor, some discrepancies were observed, leading to the development of a far-field system to validate the results of the NF measurements. The validation process confirmed that the NF measurements were correct, and it was concluded that the discrepancies were caused by the structure that holds the AiP antenna to the socket.

Finally, a demonstration of the beamforming capabilities was also displayed by steering the beam in azimuth from -20° to 20° every 5° .

Chapter 6

Conclusions and Future Work

The PAARD's mmWave scanner system is a reconfigurable system capable of performing various measurement and characterization tests. This thesis focuses on making numerous improvements to the software to enhance the system's usability, particularly in antenna measurement tests. Additionally, antenna-in-package calibration and measurement operations were implemented.

6.1 List of Conclusions

- MATLAB is a user-friendly and adaptable programming language, enabling easy design of graphical interfaces and programming of system control structures. This thesis has showcased the system's remarkable versatility and reconfigurability. With a deep understanding of MATLAB programming, graphical interface design, and system control class files, users can seamlessly integrate or modify both simple and complex operation modes to suit their requirements. The evidence supporting this assertion lies in the successful addition and implementation of the calibration setup, as well as the near-field (NF) and far-field (FF) measurement modes for the AiP antenna on chip, as detailed in Chapter 5.

- Although the new graphic interface of the system was designed to be more intuitive and comprehensive than the original software developed in LABVIEW, users still require a reasonable understanding of the software to operate the system properly. Without this understanding, accidents may occur.
- The continuous NF measurement significantly reduces scanning time while maintaining an acceptable level of quality and accuracy in the results. This algorithm accelerates measurements by 2.6 times compared to the park-and-probe method. Although the algorithm initially encountered an issue with the sampling period, it was successfully resolved, ensuring reliable results.
- In the NF measurement mode, the graphic interface not only enables users to view real-time measured data but also presents it in a spatial plane. This functionality allows users to visualize the electromagnetic characteristics in the NF region of the AUT. In contrast, while the original software can display real-time data, it does so in a linear plot of magnitude over time.
- The only two operation modes necessitating post-processing operations are the NF and material characterization modes. These modes compute pertinent values from the s-parameters collected during the test, and in the new software, these algorithms are already integrated. Additionally, users can save the raw s-parameter data in a separate file and apply any post-processing algorithm as desired.
- The new support structure for the FF antenna enables precise positioning of the center of the AUT on the axis of rotation. To test this feature's functionality, three different WR10 antennas were utilized. The second prototype

successfully addressed the issues encountered in the first prototype. These issues included material bending due to the combined weight of the frequency extender and the AUT, leading to misalignment, as well as the high risk of material breakage due to excessive bending.

- After the calibration process of the AiP, the results of the two different types of AiP are displayed in Table 5.1. This table presents the mean and statistical standard deviation, where the latter describes the spread of the data from the mean. The standard deviation can approximate the calibration error. For TX measurements, the maximum phase error is 1.49° , and the minimum is 1.41° , indicating consistency in the calibration results. However, in RX measurements, the maximum and minimum phase errors are 1.37° and 0.73° respectively. This implies that the calibration was significantly better at 78 and 80 GHz compared to 77 GHz in the RX AiP.
- Table 5.1 indicates that the excitation errors for various frequencies are smaller compared to the resolution of VGA and phase shifters. This can be verified in Figure 5.9.b, where the elements, despite being excited with the same digital states for the VGA and phase shifter, exhibit significantly different phases. Consequently, the radiation pattern deviates substantially from the ideal pattern.
- The discrepancy observed in Figure 5.9.c, particularly the disparity between the measured radiation patterns and the calculated array factor, is likely attributable to edge effects induced by the surrounding structure of the AiP, as

depicted in Figure 4.3 (the sole image of the AiP antenna array). Another contributing factor could be the limited number of elements in the AiP antenna array, leading to instability in the radiation pattern.

6.2 Future work

The mmWave scanner system is a complete instrument capable of antenna measurement and calibration. The hardware and software works harmoniously in order to collect the most truthful results in the least possible time. However, despite its capabilities, there remains an opportunity for further enhancement within this system.

- This work, in Chapter 3, has described one solution of implement continuous motion raster scanning for the NF measurements, which utilize the same control computer to perform the sampling with a periodic timer. Nevertheless, this solution requires a period correction process due to the queue lag or background processes of the computer. Another approach is to have a dedicated system that is capable of sending the controlling commands to the VELMEX controllers and send a trigger signal to the VNA to perform a sweep measurements. This system would synchronize both the motion and sampling to perform a continuous raster scan more accurately. High level machines like computers, that can be affected by the background operations in their systems, cannot be used, it would also be a waste of computational resources. Embedded systems or microcontrollers might be right for this task.

- The AiP array antennas can be implemented in a larger array system for radar measurements. It is possible design of an AiP antenna socket that can hold many chip for a larger array. Furthermore, the same calibration setup can be used to calibrate the entire array antenna. To finally achieve the design of a virtual array system.
- Other instruments aside of mmWave instruments can be implemented to the system. For example, laser type devices that allows the measurement of profiles of different AUTs. With this instruments, it is possible to achieve measurement of flatness or planary of a planar phase array antenna. This is important because, in the mmWave realm, an imperfection in the antenna will cause a huge phase error.

Bibliography

- [1] Velmex, “Velmex application notes an106.” https://www.velmex.com/Downloads/Software/App_Notes/an106.pdf.
- [2] S. Gregson, J. McCormick, and C. Parini, *Principles of planar near-field antenna measurements*, vol. 53. IET, 2007.
- [3] J. L. Salazar-Cerreno, Z. Qamar, and N. Aboserwal, “A multipurpose and reconfigurable mm-wave scanner system for accurate measurements of passive/active antenna array, array calibration, radome and material characterization,” in *2021 IEEE Conference on Antenna Measurements and Applications (CAMA)*, pp. 555–559, 2021.
- [4] MathWorks, “Schedule execution of matlab.” <https://www.mathworks.com/help/matlab/ref/timer.html>.
- [5] Eravant, “Wr-12 waveguide rectangular horn antenna.” <https://www.eravant.com/23-dbi-gain-wr-12-e-band-rectangular-horn-antenna>.
- [6] R. G. Fellers, “Millimeter waves and their applications,” *Electrical Engineering*, vol. 75, no. 10, pp. 914–917, 1956.
- [7] M. Marcus and B. Pattan, “Millimeter wave propagation: spectrum management implications,” *IEEE Microwave Magazine*, vol. 6, no. 2, pp. 54–62, 2005.
- [8] C. A. Balanis, *Antenna Theory: Analysis and Design, 3rd Edition*. Wiley, 2005.
- [9] S. Li, H. T. Nguyen, T. Chi, C. Li, N. Cahoon, A. Kumar, G. Freeman, D. Harame, and H. Wang, “Performance of v-band on-chip antennas in globalfoundries 45nm cmos soi process for mm-wave 5g applications,” in *2018 IEEE/MTT-S International Microwave Symposium - IMS*, pp. 1593–1596, 2018.
- [10] H. Singh, S. Mandai, and S. Mandai, “Silicon-based ferrite loaded miniaturized on-chip antenna for biomedical applications with improved gain and efficiency,” in *2019 European Microwave Conference in Central Europe (EuMCE)*, pp. 179–182, 2019.
- [11] A. Babakhani, X. Guan, A. Komijani, A. Natarajan, and A. Hajimiri, “A 77-ghz phased-array transceiver with on-chip antennas in silicon: Receiver and antennas,” *IEEE Journal of Solid-State Circuits*, vol. 41, no. 12, pp. 2795–2806, 2006.
- [12] M.-R. Nezhad-Ahmadi, M. Fakharzadeh, B. Biglarbegian, and S. Safavi-Naeini, “High-efficiency on-chip dielectric resonator antenna for mm-wave transceivers,” *IEEE Transactions on Antennas and Propagation*, vol. 58, no. 10, pp. 3388–3392, 2010.

- [13] X.-Y. Bao, Y.-X. Guo, and Y.-Z. Xiong, “60-ghz amc-based circularly polarized on-chip antenna using standard 0.18- μ m cmos technology,” *IEEE Transactions on Antennas and Propagation*, vol. 60, no. 5, pp. 2234–2241, 2012.
- [14] B. B. Adela, P. T. M. van Zeijl, U. Johannsen, and A. B. Smolders, “On-chip antenna integration for millimeter-wave single-chip fmcw radar, providing high efficiency and isolation,” *IEEE Transactions on Antennas and Propagation*, vol. 64, no. 8, pp. 3281–3291, 2016.
- [15] I. Gresham, A. Jenkins, R. Egri, C. Eswarappa, N. Kinayman, N. Jain, R. Anderson, F. Kolak, R. Wohlert, S. Bawell, J. Bennett, and J.-P. Lanteri, “Ultra-wideband radar sensors for short-range vehicular applications,” *IEEE Transactions on Microwave Theory and Techniques*, vol. 52, no. 9, pp. 2105–2122, 2004.
- [16] E. Channabasappa, “Balanced antenna arrays for 24 ghz automotive uwb radar sensors,” in *2007 IEEE Antennas and Propagation Society International Symposium*, pp. 785–788, 2007.
- [17] C. Zhu, Z. Duan, and Y. Dai, “A flip-chip packaged design of planar antenna array based on dual-feed network for 77-ghz automotive radar,” in *2020 IEEE Asia-Pacific Microwave Conference (APMC)*, pp. 779–781, 2020.
- [18] N. Pazare and V. Kamble, “A 77 ghz microstrip comb-line antenna array for automotive radar application,” in *2022 Antenna Measurement Techniques Association Symposium (AMTA)*, pp. 1–5, 2022.
- [19] Metawave, “First 77ghz beamforming chip in aip module for defense and commercial high-resolution 4d imaging radar.” <https://www.metawave.com/post/first-77ghz-beamforming-chip-in-aip-module-for-defense-commercial-high-resolution-4d-imaging-radar>.
- [20] K. Hassett, “Phased array antenna calibration measurement techniques and methods,” *IEEE*, 2016.
- [21] G. He, X. Gao, and R. Zhang, “Impact analysis and calibration methods of excitation errors for phased array antennas,” *IEEE Access*, vol. 9, pp. 59010–59026, 2021.
- [22] J. Mulcahey and M. Sarcione, “Calibration and diagnostics of the thaad solid state phased array in a planar nearfield facility,” in *Proceedings of International Symposium on Phased Array Systems and Technology*, pp. 322–326, 1996.
- [23] T. Xiang, J. Gu, B. Yu, and X. Zhang, “A sensing-based over-the-air phased array antennas phase calibration method with greedy algorithm,” *IEEE Antennas and Wireless Propagation Letters*, vol. 20, no. 12, pp. 2240–2244, 2021.
- [24] C. Shipley and D. Woods, “Mutual coupling-based calibration of phased array antennas,” in *Proceedings 2000 IEEE International Conference on Phased Array Systems and Technology (Cat. No.00TH8510)*, pp. 529–532, 2000.

- [25] A. Nafe, K. Kibaroglu, M. Sayginer, and G. M. Rebeiz, “An in-situ self-test and self-calibration technique utilizing antenna mutual coupling for 5g multi-beam trx phased arrays,” in *2019 IEEE MTT-S International Microwave Symposium (IMS)*, pp. 1229–1232, 2019.
- [26] R. M. Lebrón, P.-S. Tsai, J. M. Emmett, C. Fulton, and J. L. Salazar-Cerreno, “Validation and testing of initial and in-situ mutual coupling-based calibration of a dual-polarized active phased array antenna,” *IEEE Access*, vol. 8, pp. 78315–78329, 2020.
- [27] H.-T. Chou, J. W. Liu, and W.-J. Liao, “Fast phased array antenna calibration incorporating with a far-field radiation measurement system,” in *2019 13th European Conference on Antennas and Propagation (EuCAP)*, pp. 1–4, 2019.
- [28] Quadsat, “Drone-based antenna measurements and calibration.” <https://www.quadsat.com>.
- [29] A. Y. Umeyama, J. L. Salazar-Cerreno, and C. J. Fulton, “Uav-based far-field antenna pattern measurement method for polarimetric weather radars: Simulation and error analysis,” *IEEE Access*, vol. 8, pp. 191124–191137, 2020.
- [30] J. L. Salazar-Cerreno, S. S. Jehangir, N. Aboserwal, A. Segales, and Z. Qamar, “An uav-based polarimetric antenna measurements for radar and communication systems from 3 ghz to 32 ghz,” in *2021 IEEE Conference on Antenna Measurements and Applications (CAMA)*, pp. 55–60, 2021.
- [31] J. L. Salazar-Cerreno, C. Fulton, K. Burdi, A. Segales, D. Schwartzman, and R. Palmer, “Accuracy assessment of antenna patterns using unmanned aerial vehicle (uav) platforms,” in *2023 IEEE Conference on Antenna Measurements and Applications (CAMA)*, pp. 175–178, 2023.
- [32] C. De Martino, A. Visweswaran, and M. Spirito, “Over-the-air characterization of mm-wave on-chip antennas and tx modules, concept and calibration,” in *2020 95th ARFTG Microwave Measurement Conference (ARFTG)*, pp. 1–4, 2020.
- [33] F. Zhang, W. Fan, Z. Wang, Y. Zhang, and G. F. Pedersen, “Improved over-the-air phased array calibration based on measured complex array signals,” *IEEE Antennas and Wireless Propagation Letters*, vol. 18, no. 6, pp. 1174–1178, 2019.
- [34] B. T. Walkenhorst and A. C. Newell, “Measuring g/t of active antennas using planar near-field scanners,” in *2019 International Conference on Electromagnetics in Advanced Applications (ICEAA)*, pp. 0903–0908, 2019.
- [35] G. F. Masters, “Probe-correction coefficients derived from near-field measurement,” in *Antenna Measurement Techniques Association Symposium*, vol. 1, AMTA, 1991.
- [36] G. Hindman and D. S. Fooshe, “Probe correction effects on planar, cylindrical and spherical near-field measurements,” in *Antenna Measurement Techniques Association, 20th annual Meeting and Symposium*, vol. 1, AMTA, 1998.

- [37] K. Sukpreecha, S. Kittiwittayapong, T. Lertwiriya-prapa, D. Torrungrueng, and K. Phaebua, “Compact spherical near-field scanning system for antenna radiation pattern measurement,” in *2023 20th International Conference on Electrical Engineering/Electronics, Computer, Telecommunications and Information Technology (ECTI-CON)*, pp. 1–4, 2023.
- [38] A. Tankielun, A. Belkacem, M. Akinci, M. Celik, H. Bartko, and B. Derat, “Quiet zone verification of plane wave synthesizer using polar near-field scanner,” in *2020 14th European Conference on Antennas and Propagation (EuCAP)*, pp. 1–5, 2020.
- [39] R. M. Lebrón, J. L. Salazar, C. Fulton, S. Duthoit, D. Schmidt, and R. Palmer, “A novel near-field robotic scanner for surface, rf and thermal characterization of millimeter-wave active phased array antenna,” in *2016 IEEE International Symposium on Phased Array Systems and Technology (PAST)*, pp. 1–6, 2016.
- [40] V. Avetissian, “Scanner with transmission line for conventional planar antenna near-field measurement in the short millimeter waveband,” *IEEE Transactions on Antennas and Propagation*, vol. 52, no. 9, pp. 2500–2503, 2004.
- [41] D. J. v. Rensburg and J. Wynne, “Near-field / far-field application for a spherical scanner at mm-wave frequencies,” in *2018 International Symposium on Antennas and Propagation (ISAP)*, pp. 1–2, 2018.
- [42] D. Slater, *Near-field Antenna Measurements*. Antenna Library, Artech House, 1991.
- [43] A. Yaghjian, “An overview of near-field antenna measurements,” *IEEE Transactions on Antennas and Propagation*, vol. 34, no. 1, pp. 30–45, 1986.
- [44] D. M. Kerns, “Plane-wave scattering-matrix theory of antennas and antenna-antenna interactions - Formulation and applications,” *Journal of Research Section B Mathematical Sciences B*, vol. 80B, pp. 5–51, Mar. 1976.
- [45] “Ieee recommended practice for near-field antenna measurements,” *IEEE Std 1720-2012*, pp. 1–102, 2012.
- [46] C. M. Technologies, “Near and far field measurement.” <https://coppermountaintech.com/near-and-far-field-measurement/>, 2022.
- [47] MathWorks, “App designer of matlab.” <https://www.mathworks.com/products/matlab/app-designer.html>.
- [48] MathWorks, “Object-oriented programming - matlab.” <https://www.mathworks.com/products/matlab/object-oriented-programming.html>.
- [49] G. E. Mueller and W. A. Tyrrell, “Polyrod antennas,” *The Bell System Technical Journal*, vol. 26, no. 4, pp. 837–851, 1947.
- [50] Keysight, “U8480 series - data sheet.” <https://www.keysight.com/us/en/assets/7018-03734/data-sheets/5991-1410.pdf>.

Appendix A

Velmex Application Notes-AN106

Table A.1: A portion of the complete table from [1] is provided below, where x represents the value in the command **AmMx**, which configures the acceleration, and m denotes the motor ID.

Calculated period (ms)	Average period (ms)	Difference (ms)
x	Step/sec ²	Start/Stop Speed
1	4000	45
2	8000	141
3	12000	190
4	16000	228
5	20000	261
6	24000	290
7	28000	316
8	32000	341
9	36000	363
10	40000	385
11	44000	405
12	48000	424
13	52000	443
14	56000	461
15	60000	478